

STRUCTURES OF CROSSLINKED NETWORKS

A Thesis  
Submitted to the Graduate Faculty  
of the  
North Dakota State University  
of Agriculture and Applied Science

By

Malia Zee

In Partial Fulfillment of the Requirements  
for the Degree of  
MASTER OF SCIENCE

Major Department:  
Coatings and Polymeric Materials

April 2015

Fargo, North Dakota

North Dakota State University  
Graduate School

---

**Title**

Structures of Crosslinked Networks

---

**By**

Malia Zee

---

The Supervisory Committee certifies that this disquisition complies with North Dakota State University's regulations and meets the accepted standards for the degree of

Master of Science

---

Supervisory Committee:

Stuart G Croll  
Chair

---

Daniel M Kroll

---

Andriy Voronov

---

Approved:

April 17, 2015  
Date

---

Dean C Webster  
Department Chair

---

## ABSTRACT

Two independent sets of studies are conducted on two collections of thermoset coatings, each exploring the molecular-level structures of its subject materials. The first work searches for the sources of durability in a library of paint film samples, prepared using linseed oil and inorganic pigments 1-2 decades before analysis. The second inquiry examines a series of end-linked polymer networks, created using different monomer architectures through molecular dynamics. Investigations proceed by drawing connections between the materials' local structures and their large-scale properties: for oil paint, guided by questions of whether metal carboxylates are responsible for the films' cohesion, and if so, then through what means; for simulations, by viewing all data through the lens of the theory of rubber elasticity, as well as outside of it. In the end, a new working model for the structure of mature oil paint is proposed; extensive connections between model and real-world polymers are made.

## ACKNOWLEDGEMENTS

My deepest gratitude is to chance for having paired me with my committee chair, Stuart Croll. While I can imagine a match that would be more concordant, I can imagine many things that do not exist.

I thank Dawn Rogala for introducing Stuart (and, through him, me) to the art conservation problem that is the subject of my first chapter. That work would not have been possible without aged oil paint specimens provided to Stuart by Marion Mecklenburg and the Smithsonian Institution, nor without the Lowell-Woods Scholarship which enabled me to select a research project in accord with my interests, independent of funding. I also thank Scott Payne for electron microscopy and Heidi Docktor for training me on infrared and thermal instrumentation.

I am grateful to chance a second time for the improbable phonetic likeness of the last names of Stuart and Dan Kroll, which triggered in me the idea to join their molecular dynamics project, the subject of my second chapter and the springboard to my professional work. I thank Dan immensely for writing all the network analysis programs that I had in mind – which seemed endlessly many, whenever I asked; working together has been a pleasure. I thank Mark Stevens of Sandia National Labs for helping Dan (and, through him, me) to orient in the *LAMMPS* environment. I am thoroughly grateful to Sandia National Labs and the Blender Foundation for developing and distributing free and open-source software which were used materially in this work. I thank the Army Research Laboratory for funding, and the NDSU Center for Computationally Assisted Science and Technology (CCAST) for providing distributed computing resources. It has been fun.

## PREFACE

The studies in this manuscript are united by theme: they explore structures that arise spontaneously in thermoset networks. However, they have two separable subjects: randomly crosslinked linseed oil paint films that exist in the real world, and end-linked chemistry-agnostic networks that exist digitally as output of computer simulations. The conceptual form of this work is in two independent parts. Yet, on paper, formatting requirements eclipse the content. The top-level organization of this dissertation is clumsy: form does not follow function.

The material, then, is organized into just two large chapters, each resting on a multitude of appendices. Some of these appendices are closer in scope to a traditional chapter than an austere listing of supporting datasets. Nonetheless, they do retain some appendix character since they were written with focus resting on their parent chapter to preserve cohesion. The arrangement of the components, however, is mangled: appendices for chapter 1 appear no earlier than chapter 2, and appendices for chapter 2 follow appendices for chapter 1. A consultation with the table of contents is in order.

# TABLE OF CONTENTS

ABSTRACT .....	iii
ACKNOWLEDGEMENTS .....	iv
PREFACE .....	v
LIST OF TABLES .....	x
LIST OF FIGURES .....	xi
LIST OF APPENDIX TABLES .....	xiii
LIST OF APPENDIX FIGURES .....	xiv
CHAPTER 1. LONG-TERM EFFECTS OF PIGMENTS ON STRUCTURES IN OIL PAINT FILMS .....	1
1.1. Introduction .....	1
1.2. Background Chemistry .....	2
1.3. Experimental Procedures .....	3
1.3.1. Manufacture of Paint Films .....	3
1.3.2. Synthesis of Metal Soaps .....	4
1.3.3. Characterization .....	6
1.4. Results .....	8
1.4.1. Macroscopic Properties .....	8
1.4.2. Scanning Electron Microscopy .....	9
1.4.3. Infrared Spectroscopy .....	10
1.4.4. Dynamic Mechanical Thermal Analysis .....	14
1.4.5. Differential Scanning Calorimetry .....	17
1.5. Discussion .....	21
1.5.1. Introduction .....	21
1.5.2. Current Working Model of Mature Oil Paint .....	22
1.5.3. Revised Working Model of Mature Oil Paint .....	24
1.5.4. Azelate Phases in Oil Paint .....	26
1.6. Conclusion .....	28
1.7. References .....	30

CHAPTER 2. IMPACT OF CROSSLINK DENSITY ON TOPOLOGY AND THERMO-MECHANICAL RESPONSES IN CHEMISTRY-AGNOSTIC THERMOSETS .....	34
2.1. Introduction .....	34
2.2. Model Description .....	37
2.2.1. Monomers .....	37
2.2.2. Particle Interactions .....	38
2.2.3. Simulation Procedure .....	40
2.3. Macroscopic Characteristics .....	45
2.3.1. Volumetric Properties .....	45
2.3.2. Elastic Properties .....	47
2.3.3. Section Conclusion .....	59
2.4. Local Network Topologies .....	60
2.4.1. Definitions of Terms .....	60
2.4.2. Analytical Procedure .....	62
2.4.3. Results and Discussion .....	63
2.5. Conclusion .....	67
2.6. References .....	67
APPENDIX A. INFRARED ANALYSIS OF OIL PAINT AND FILMS .....	71
A.1. Introduction .....	71
A.2. Results .....	71
A.2.1. Unpigmented Oil .....	71
A.2.2. Films Containing Inert Pigments .....	73
A.2.3. Films Pigmented with Lead .....	76
A.2.4. Films Pigmented with Zinc .....	77
A.2.5. Films Pigmented with Copper .....	79
A.2.6. Films Pigmented with Iron .....	80
A.3. Discussion .....	86
A.4. Conclusion .....	90
A.5. References .....	90

APPENDIX B. THERMAL ANALYSIS OF METAL SOAPS .....	93
B.1. Synthesis of Metal Soaps .....	93
B.2. Identification of Degradation Temperatures .....	96
B.3. Identification of Phase Transitions .....	100
B.3.1. Lead Soaps .....	100
B.3.2. Zinc Soaps .....	101
B.3.3. Copper Soaps .....	101
B.3.4. Iron Soaps .....	102
B.3.5. Summary .....	103
B.4. Correspondence Between Metal Soaps and Paint Films .....	103
B.5. References .....	104
APPENDIX C. THERMAL ANALYSIS OF PAINT FILMS .....	106
C.1. Introduction .....	106
C.2. Differential Scanning Calorimetry .....	106
C.3. Dynamic Mechanical Thermal Analysis .....	106
C.4. References .....	110
APPENDIX D. MASS SPECTRA OF LEAD OIL PAINT FILMS .....	111
D.1. Background .....	111
D.2. Results and Discussion .....	111
D.3. Conclusion .....	115
D.4. References .....	115
APPENDIX E. INTRODUCTION TO MOLECULAR DYNAMICS .....	116
E.1. Introduction .....	116
E.2. Time Evolution .....	116
E.3. Control of Temperature and Pressure .....	118
E.3.1. Introduction .....	118
E.3.2. Canonical Ensemble (NVT) .....	119
E.3.3. Isobaric-Isothermal Ensemble (NPT) .....	121
E.4. Conclusion .....	123



E.5. References .....	124
APPENDIX F. MAPPING OF PHYSICAL UNITS TO COARSE-GRAINED UNITS .....	125
F.1. Introduction .....	125
F.2. Mapping Calculations .....	125
F.3. Mapped Simulation Parameters .....	128
F.4. Mapped Simulation Results .....	130
F.5. References .....	131
APPENDIX G. NETWORK EVOLUTION DURING CROSSLINKING .....	132
G.1. Introduction .....	132
G.2. Simulation Procedure .....	132
G.3. Results and Discussion .....	133
G.4. Conclusion .....	137
G.5. References .....	138

## LIST OF TABLES

<u>Table</u>	<u>Page</u>
1.1. Compositions of oil paint films characterized in this work .....	4
1.2. Simplest method able to produce the desired metal soap .....	5
1.3. Starting chemicals that were used in syntheses of metal soaps .....	5
1.4. Locations of features observed by thermal analyses of the oil paint films and the corresponding metal soaps .....	18
2.1. Monomer amounts used to simulate each network model .....	40
2.2. Extents of the crosslinking reactions .....	43
2.3. Glass transition temperatures, specific volumes at $T_g$ , and coefficients of volumetric thermal expansion .....	46
2.4. Elastically active network fractions and elastic moduli at $T=1.0 \text{ } \varepsilon/k_B$ .....	53
2.5. Elastic moduli and Poisson's ratios determined at $T=1.0$ and $T=0.3 \text{ } \varepsilon/k_B$ .....	56

## LIST OF FIGURES

<u>Figure</u>	<u>Page</u>
1.1. Chemical structures of some unbound fatty acids as well as the most common fatty acids in linseed oil – oleic, linoleic, and linolenic – that are bound into a triglyceride .....	2
1.2. Scanning electron microscope backscatter images of oil paint films .....	10
1.3. Details of infrared spectra of selected oil paint films .....	12
1.4. $\tan \delta$ and storage modulus plots of aged oil paint films .....	15
1.5. DSC thermograms of selected oil paint films and the corresponding metal azelates .....	20
1.6. Schematic of the existing working model for metal-coordinated oil paint .....	23
2.1. Monomers used to create the crosslinked networks that were investigated in this study, shown flattened to two dimensions for readability .....	37
2.2. Schematic diagram of a two-dimensional equivalent of a defect-free network segment of model 4-5 .....	37
2.3. Potentials used to model interactions between particles and separated components of the bonded potential .....	38
2.4. Soft nonbonded potential used during the push-off run at the start of the simulation procedure, as compared to the WCA potential .....	40
2.5. Snapshot of one of the samples of model 4-5 at $T=1.0 \text{ } \epsilon/k_B$ following crosslinking and equilibration .....	44
2.6. System densities at hot and cold temperatures used throughout the study and the the extent of shrinkage upon cooling .....	44
2.7. Calculation of the glass transition temperature for one of the samples of model 6-3 .....	45
2.8. Determination of the elastic modulus above $T_g$ for one of the samples of model 6-3 .....	47
2.9. Determination of the elastic modulus above $T_g$ for one of the samples of model 3-5 .....	48
2.10. Determination of the Poisson's ratio above $T_g$ .....	50
2.11. Influence of the duration of the pre-equilibration period on the results of tensile testing conducted below $T_g$ for one of the samples of model 3-5 .....	51
2.12. Determination of the elastic modulus below $T_g$ for one of the samples of model 3-5 .....	51
2.13. Determination of the Poisson's ratio below $T_g$ .....	53
2.14. Schematic diagram of a portion of a network of model 4-5 .....	61

2.15. Snapshots of a one of the samples of each model 3-5 and model 6-3 at $T=1.0 \varepsilon/k_B$ following crosslinking and equilibration .....	63
2.16. Comparison of the present data for models 4-3 and 4-5 with data reported by Duering, Kremer, and Grest for analogous systems and with the theoretical prediction of Jacobson and Stockmayer .....	64
2.17. Prevalence of network defects in the series of thermosets under study .....	65

## LIST OF APPENDIX TABLES

<u>Table</u>	<u>Page</u>
A.1. Organic and organometallic IR band assignments for fresh oil paint and aged oil paint films .....	87
B.1. Temperatures at which metal soaps and starting acids exhibit endotherms or exotherms in their DSC thermograms .....	96
B.2. Temperatures at which metal soaps exhibit peaks in their DTG plots .....	97
B.3. Temperatures at which metal soaps and starting acids exhibit endotherms or exotherms in their DSC thermograms .....	97
C.1. Results of the calculation used to estimate crosslink densities of the films .....	110
F.1. Glass transition temperatures of some common thermosets, each prepared from a stoichiometric mixture of a DGEBA epoxy and the diamine listed .....	127
F.2. Simulation time scales mapped from Lennard-Jones units to real-world units .....	129
F.3. Characterization results mapped from Lennard-Jones units to real-world units .....	130
G.1. Extents of the crosslinking reactions described in the primary study in Chapter 2 compared to the extents of reactions of the supplementary study which is the subject of this appendix .....	132
G.2. Extents of reaction at gelation, $p_{gel}$ , predicted for the present models using the Flory-Stockmayer theory and the Carothers theory, as well as the value obtained by averaging the two predictions .....	136

## LIST OF APPENDIX FIGURES

<u>Figure</u>	<u>Page</u>
A.1. Infrared spectrum of fresh cold-pressed linseed oil and its second derivative, inverted .....	72
A.2. Infrared spectrum of fresh refined linseed oil and its second derivative, inverted .....	72
A.3. Infrared spectrum of a 12.3-year-old unpigmented cold-pressed linseed oil film and its second derivative, inverted .....	73
A.4. Infrared spectrum of an 18.8-year-old oil paint pigmented with Silica and its second derivative, inverted .....	74
A.5. Infrared spectrum of an 18.8-year-old oil paint pigmented with Barium Sulfate and its second derivative, inverted .....	75
A.6. Infrared spectrum of an 18.8-year-old oil paint pigmented with Calcium Carbonate and its second derivative, inverted .....	75
A.7. Infrared spectrum of a 21.0-year-old oil paint pigmented with White Lead and its second derivative, inverted .....	76
A.8. Infrared spectrum of an 11.3-year-old oil paint pigmented with White Lead and its second derivative, inverted .....	76
A.9. Infrared spectrum of an 18.8-year-old oil paint pigmented with Naples Yellow and its second derivative, inverted .....	77
A.10. Infrared spectrum of a 20.8-year-old oil paint pigmented with Zinc White and its second derivative, inverted .....	78
A.11. Infrared spectrum of a 12.2-year-old oil paint pigmented with Zinc White and its second derivative, inverted .....	78
A.12. Infrared spectrum of an 18.7-year-old oil paint pigmented with Malachite and its second derivative, inverted .....	80
A.13. Infrared spectrum of an 18.7-year-old oil paint pigmented with Red Iron Oxide and its second derivative, inverted .....	81
A.14. Infrared spectrum of a 20.8-year-old oil paint pigmented with Raw Sienna and its second derivative, inverted .....	82
A.15. Infrared spectrum of an 18.7-year-old oil paint pigmented with Yellow Ochre and its second derivative, inverted .....	84
A.16. Infrared spectrum of an 18.7-year-old oil paint pigmented with Raw Umber and its second derivative, inverted .....	85
B.1. DSC thermograms of metal salts that were used as precursors in the synthesis of metal soaps ..	95

B.2.	DSC thermograms of azelate soaps and their precursors .....	95
B.3.	DSC thermograms of palmitate soaps and their precursors .....	95
B.4.	DSC thermograms of stearate soaps and their precursors .....	95
B.5.	TG plots of synthesized metal soaps. Dashed lines denote derivative (DTG) plots .....	98
B.6.	DSC thermograms of lead soaps and the corresponding oil paint film .....	100
B.7.	DSC thermograms of zinc soaps and the corresponding oil paint film .....	100
B.8.	DSC thermograms of lead soaps and the corresponding oil paint film .....	102
B.9.	DSC thermograms of iron soaps and one of the corresponding oil paint film .....	102
B.10.	DSC thermograms of soft oil paint films .....	104
C.1.	Detail of DSC thermograms of aged oil paint films .....	106
C.2.	Tan $\delta$ plots of aged oil paint films pigmented with White Lead, Zinc White, and Malachite .....	107
C.3.	Storage modulus plots of aged oil paint films pigmented with White Lead, Zinc White, and Malachite .....	108
C.4.	Loss modulus plots of aged oil paint films pigmented with White Lead, Zinc White, and Malachite .....	109
C.5.	Detail of the storage modulus plots of aged oil paint films pigmented with White Lead, Zinc White, and Malachite .....	110
D.1.	Mass spectra of selected oil paint films showing $m/z$ ranges that contain peaks assigned to free fatty acids .....	112
D.2.	Mass spectra of selected oil paint films showing $m/z$ ranges that contain peaks assigned to free lead and lead-bound soaps .....	113
D.3.	Mass spectra of a 21-year-old oil paint pigmented with Naples Yellow, showing $m/z$ ranges that contain peaks assigned to free lead .....	114
F.1.	A schematic that shows coarse-grained model 4-3 mapped to a $n=0$ DGEBA chain extender and a DETDA crosslinker .....	126
G.1.	Network properties for each model throughout the course of crosslinking reactions shown as a function of time .....	134
G.2.	Network properties for each model throughout the course of crosslinking reactions shown as a function of conversion .....	135
G.3.	Prevalence of network defects in the series of thermosets in the primary study in Chapter 2 compared to the same in the supplementary study which is the subject of this appendix .....	137

# CHAPTER 1. LONG-TERM EFFECTS OF PIGMENTS ON STRUCTURES IN OIL PAINT FILMS

## 1.1. Introduction

The rising environmental and financial costs of the world's continued consumption of petrochemicals have become widely known in recent years, and there now exists a market demand for sustainable alternatives. While the energy industry is developing several technologies in parallel to one another, the chemical industry has only alternative: to displace fossil feedstocks for polymers and other organic chemicals with renewable vegetable and animal counterparts. However, the performance of bio-based polymers must be raised before they can fully compete with petrochemicals. For the coatings industry, this translates to an improved understanding of how polymer networks that are based on vegetable oils may be made durable over extended periods of time.

The present work advances that goal through the study of pigmented oil paint films. Similar film models are studied extensively in the fields of art history and conservation, but for a different purpose, primarily to identify the compositions of paintings and to evaluate the safety of potential restoration treatments. Many of the factors that are critical in art conservation, such as possible interactions with solvents used for cleaning and with varnishes used for protection, are considerably less salient outside the field. Similarly, factors that are important to the development of bio-based coatings, such as mechanisms that give rise to dramatic variation in mechanical properties among comparable films, are less pertinent to art conservation (since restorers are severely limited in their abilities to alter compositions of existing paintings), – so these questions are typically investigated in less thorough detail. This study, then, builds on the large body of work in art conservation and considers traditional oil paint from the perspective of coatings.

The dependence of mechanical properties of oil paint on its constituent pigments has long been known by artists and conservators in general terms. These properties depend on the age of the paint film and continue to evolve for periods that span decades or even centuries, although the rate of change decreases with time [1-2]. Unpigmented oil paint cures hardly at all. Paints containing *earth color* (iron



and clay-based) pigments cure initially but years later soften and become susceptible to moisture damage. White pigments based on lead and zinc both render their enveloping paints stiff. However, while lead paint remains durable as it ages, zinc paint becomes brittle within only years.

Mixtures of pigments produce properties that are qualitatively intermediate between those of individual pigments. Further, the properties of a given paint layer may depend on the pigment content of the adjacent layers. Due to the diffusion of metal ions, when a white ground layer (primer) contains lead, durability of the layers above the ground is increased, whereas zinc-based grounds render upper layers susceptible to cracking and delamination [2-4]. These well-known characteristics of the lead and the zinc-based paints have been long linked to the formation of metal soaps within the films. One of the present questions was whether soaps are present in the much younger films under study. Another, more important question was the manner in which they affect the mechanical properties of their containing films.

## 1.2. Background Chemistry

Oil paint chemistry is complex and has been discussed more thoroughly elsewhere [5-8]. In brief, drying oils consist primarily of triglycerides (esters of glycerol with three fatty acids) and contain unbound fatty acids in much smaller proportions (Figure 1.1). When the oil is exposed to air, unsaturated fatty acids that are bound into triglycerides at one end form additional bonds to each other through free

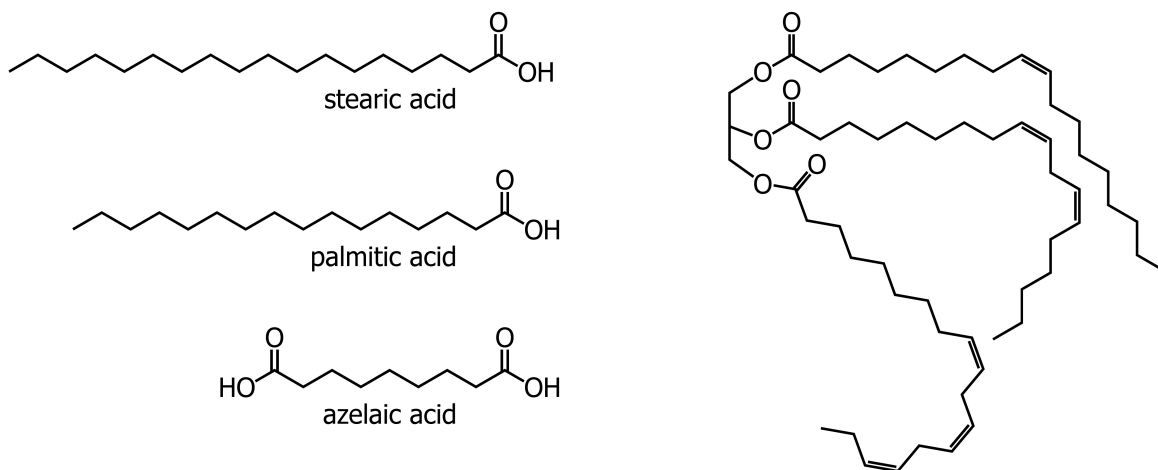


**Figure 1.1.** Chemical structures of some unbound fatty acids (left) as well as the most common fatty acids in linseed oil – oleic, linoleic, and linolenic – that are bound into a triglyceride (right).

radical chain reactions, eventually yielding a cohesive film. Saturated fatty acids do not appreciably participate in such crosslinking. However, because they generally comprise less than 10% of the total fatty acid content, few triglycerides contain more than one saturated fatty acid moiety; therefore, saturated acids are incorporated into the network as dangling ends.

Although some oxidative reactions lead to crosslinking, others result in bond-breaking. The major degradation pathway releases a small aldehyde and an alkyl radical from the polymeric network, and the aldehyde oxidizes further to a carboxylic acid. Since saturated fatty acids are incorporated into the network only as dangling ends, they are easily cleaved, so common degradation products include the two saturated fatty acids that are present initially in the oil, palmitic acid (C<sub>16</sub>) and stearic (C<sub>18</sub>). Unsaturated fatty acids may also be released from the network, but with more difficulty because for that, two bonds must be broken: that connecting the acid to the glycerol moiety, and the bond at the crosslink site. This difficulty is offset somewhat by the much greater prevalence of unsaturated acids in the original oil. This mechanism most commonly produces azelaic acid (C<sub>9</sub>) as a degradation product, because most original fatty acids are C<sub>18</sub> and because the crosslink site tends to be located approximately in the middle. Reflecting the difference in their degradation pathways, palmitic and stearic acids are monocarboxylic (one COOH group) while azelaic acid is dicarboxylic.

Fatty acids may react with metals that are present in the paint to form metal salts, which are also termed soaps when the longer-chain fatty acids are involved. Lead soaps are notorious for their prevalence in Old Masters' oil paintings [4, 9-19]. Zinc soaps in paintings are also known [18, 20-21]. Copper soaps within traditional oil paintings are more rare [18, 22], but they have been documented in protective coatings of other copper-containing cultural artifacts [23]. No evidence of iron soaps has been located in the conservation literature, which given the widespread use of iron-based pigments indicates that iron soaps do not easily form in oil paint, or (less likely) that they form but later degrade.

### **1.3. Experimental Procedures**

#### **1.3.1. Manufacture of Paint Films**

Paint samples were prepared for the Smithsonian Center for Materials Research and Education using only cold-pressed linseed oil and pigments, without other additives. The term *cold-pressed*

**Table 1.1.** Compositions of oil paint films characterized in this work.

Category	Pigment Name	Nominal Composition	PVC (%)	Mfr Date
Special	Zinc White	ZnO	35	Dec 1998
Special	Zinc White	ZnO	35	Apr 1990
Special	White Lead	2(PbCO <sub>3</sub> )·Pb(OH) <sub>2</sub>	44	Nov 1999
Special	White Lead	2(PbCO <sub>3</sub> )·Pb(OH) <sub>2</sub>	44	Feb 1990
Special	Malachite	CuCO <sub>3</sub> ·Cu(OH) <sub>2</sub>	48	May 1992
Special	Naples Yellow	Pb <sub>3</sub> (SbO <sub>4</sub> ) <sub>2</sub>	unknown	May 1992
Earth Color	Raw Sienna	Fe <sub>2</sub> O <sub>3</sub> ·nH <sub>2</sub> O + Clay	31	Apr 1990
Earth Color	Yellow Ochre	Fe <sub>2</sub> O <sub>3</sub> ·nH <sub>2</sub> O + Clay	28	Jun 1992
Earth Color	Raw Umber	Fe <sub>2</sub> O <sub>3</sub> ·nH <sub>2</sub> O + MnO <sub>2</sub> + Clay	20	Jun 1992
Earth Color	Red Iron Oxide	Fe <sub>2</sub> O <sub>3</sub>	12	Jun 1992
Inert	Barium Sulfate	BaSO <sub>4</sub>	unknown	May 1992
Inert	Calcium Carbonate	CaCO <sub>3</sub>	unknown	May 1992
Inert	Silica	SiO <sub>2</sub>	22	May 1992
Control	Unpigmented	-	0	Nov 1998

describes the method of manufacture wherein oil is extracted from flaxseed mechanically, without the use of heat, and it is significant because heat treatments alter the starting triglyceride composition of oil [7]. Prior to the 20<sup>th</sup> century, cold-pressing had been the standard manufacturing method for artist-grade paint. For the present samples, pigment volume concentration (PVC) was varied among the paints according to the typical artists' usage (Table 1.1).

Paint films were cast on polyester sheets at a thickness of approximately 0.25 mm and were stored at the commonly accepted museum environment of 23°C and 40-50% RH, under ambient museum lighting. Polyester sheets were removed prior to characterization so all analysis was on free, unsupported paint films.

### 1.3.2. Synthesis of Metal Soaps

#### 1.3.2.1. Overview

An array of metal soaps was synthesized for use as standards in interpreting the DSC thermograms of the oil paint films. Many methods have been developed over the last century for the synthesis of metal soaps from fatty acids and metal salts [24]. In the present study, the simplest techniques were attempted first, moving on to the more involved and more efficient ones only as necessary.

**Table 1.2.** Simplest method able to produce the desired metal soap. **1:** ambient temperature, no intermediate; **2:** ambient temperature, sodium soap intermediate; **3:** high temperature, sodium soap intermediate.

	Azelate	Palmitate	Stearate
Pb	1	1	1
Zn	2	1	3
Cu	2	3	3
Fe	2	3	3

Syntheses were first attempted at ambient conditions in a one-step reaction [15]. In all but two cases (iron and zinc azelates), this procedure yielded a precipitate. Since soaps may be fingerprinted by their sharp melting peaks, the DSC trace of this precipitate was compared to the DSC trace of the starting acid to determine whether a reaction had taken place. In some cases, ambient synthesis was thus found sufficient.

When it was not, synthesis was attempted again in two steps, mediated by a sodium soap. This was done at ambient conditions when possible [25-26] and at elevated temperature otherwise [24]. Ambient conditions were feasible only in the syntheses of metal azelates because DSC showed that the sodium soap intermediate was produced at laboratory temperature only from azelaic acid. DSC analyses of the final products confirmed that a reaction had taken place. These synthetic procedures are summarized in Table 1.2. Supplemental details are provided in Appendix B.

#### 1.3.2.2. Method 1: Ambient Temperature, No Intermediate

Two solutions were prepared. One contained the appropriate metal salt (Table 1.3) in a mixture of ethanol, methanol, and deionized water; the other contained the appropriate fatty acid in ethanol,

**Table 1.3.** Starting chemicals that were used in syntheses of metal soaps.

Reagent	Formula	Supplier	Purity
Copper(II) Sulfate, Anhydrous	CuSO <sub>4</sub>	Sigma Aldrich	n/a
Zinc(II) Nitrate Hexahydrate	Zn(NO <sub>3</sub> ) <sub>2</sub> ·6H <sub>2</sub> O	Sigma Aldrich	98%
Lead(II) Acetate Trihydrate	Pb(C <sub>2</sub> H <sub>3</sub> O <sub>2</sub> ) <sub>2</sub> ·3H <sub>2</sub> O	Fisher Scientific	>97%
Iron(III) Chloride Hexahydrate	FeCl <sub>3</sub> ·6H <sub>2</sub> O	Sigma Aldrich	n/a
Azelaic Acid	HOOC(CH <sub>2</sub> ) <sub>7</sub> COOH	Sigma Aldrich	98%
Palmitic Acid	CH <sub>3</sub> (CH <sub>2</sub> ) <sub>14</sub> COOH	Sigma Aldrich	99%
Stearic Acid	CH <sub>3</sub> (CH <sub>2</sub> ) <sub>16</sub> COOH	Sigma Aldrich	95%

brought into solution by sonication. The metal and the acid were either used in stoichiometric amounts, or the metal was in excess. The solutions were combined, which produced a precipitate. This precipitate was separated by filtration, washed with water and ethanol, and was oven dried at  $\sim 105^{\circ}\text{C}$ .

#### 1.3.2.3. Method 2: Ambient Temperature, Sodium Soap Intermediate

A slurry of azelaic acid in water was titrated with an aqueous solution of sodium hydroxide until all acid dissolved and pH was close to neutral. This solution was combined with an aqueous metallic cation solution, as before, to produce a precipitate. This precipitate was separated by filtration, washed with water and ethanol, and was oven dried at  $\sim 105^{\circ}\text{C}$ .

#### 1.3.2.3. Method 3: High Temperature, Sodium Soap Intermediate

First, stoichiometric amounts of palmitic or stearic acid and sodium hydroxide were heated in water to  $70\text{-}80^{\circ}\text{C}$ , until the acid crystals had melted and the sodium soap began to form. Water was used instead of ethanol despite its lower efficiency for simplicity, in order to avoid reflux conditions. The reaction was maintained at  $70\text{-}80^{\circ}\text{C}$  for 20 minutes, after which an aqueous solution of the metal salt was added, metal being in excess of the acid. Shortly after the addition, the foam that was due to the sodium soap had disappeared, and once temperature returned to  $70^{\circ}\text{C}$ , it was maintained for another 20 minutes to drive the reaction toward completion. The precipitate was separated by filtration, washed with water and ethanol, and was oven dried at  $\sim 110^{\circ}\text{C}$ .

### **1.3.3. Characterization**

#### 1.3.3.1. Solvent Swelling

Several solvent swelling experiments were attempted in order to estimate crosslink densities of the paint films. Swelling was attempted in cyclohexanone due to its known high swelling power of oil paints and its high swelling speed [27]. More limited tests were performed in toluene and dichloromethane.

#### 1.3.3.2. Microscopy

Morphologies and elemental distributions of some of the films were investigated using electron microscopy. Each sample was coated with a thin layer of carbon prior to examination in order to reduce

charging in the electron beam. Imaging and energy dispersive X-ray spectroscopy (EDS) were performed on a JEOL JSM-7600F field emission scanning electron microscope operating at 5 kV.

#### 1.3.3.3. Infrared Spectroscopy

Functional groups present in the aged oil paint films as well as in two samples of fresh linseed oil were identified from their infrared spectra. Aged pigmented oil paint samples were ground with anhydrous potassium bromide and pressed into pellets. The aged unpigmented sample had lost all cohesion and was sufficiently translucent, so it was applied in a thin layer on a KBr disk instead. Application was analogous for samples of fresh, uncrosslinked linseed oil. Fourier transform infrared (FTIR) spectra were collected by transmission using a Nicolet 8700 spectrometer (Thermo Scientific) at a resolution of  $4\text{ cm}^{-1}$  using 32 scans per spectrum.

Straight-line baseline correction was applied to all spectra except for that of the film containing Naples Yellow pigment (in which case the scattering had been too severe for a meaningful baseline determination). In order to increase the apparent spectral resolution [28], second derivative spectra were calculated, inverted to make absorption peaks positive, and smoothed using a third-order 30-point Savitsky-Golay filter, except for the second derivative spectra of fresh linseed oils, which were used unsmoothed.

#### 1.3.3.4. Dynamic Mechanical Thermal Analysis

Thermo-mechanical properties of the films were measured with a TA Instruments Q800 dynamic mechanical analyzer using a rectangular tension geometry. This geometry was chosen because some of the films were too brittle and others, too flexible to investigate in bending, and none of the films were smooth enough to test between compression platens. Average thicknesses of the test samples were measured by a micrometer to be between 0.14 and 0.30 mm, depending on the sample, with a typical variation of 0.03 mm within each sample. Strips 5 mm wide were cut from the films and were loaded into the instrument clamps using a gage length between 20 and 25 mm.

Data were acquired at a frequency of 1 Hz using a preload force of 5 mN and an oscillation strain of .005% to .01%. After equilibration to  $-50^{\circ}\text{C}$ , samples were heated to  $400\text{-}500^{\circ}\text{C}$  at a rate of  $3^{\circ}\text{C}$  per minute under a flowing air atmosphere (as no nitrogen purge was available). In some cases, the film

fractured before reaching the upper temperature limit. In others, drastic decomposition occurred without fracture. As a result, the highest-temperature results that are sufficiently reliable for discussion were recorded well below the upper temperature limit that had been set.

#### 1.3.3.5. Thermogravimetric Analysis

Locations of decomposition events within metal soaps were approximated using a TA Instruments Q500 thermogravimetric analyzer. Samples were heated from the ambient temperature to 500°C at a rate of 20°C per minute. A nitrogen purge stream was used at a flow rate of 60 mL/min. Derivative (DTG) curves were smoothed using a second-order Savitzky-Golay filter. Decomposition temperatures were identified as minima on the DTG plots.

#### 1.3.3.6. Differential Scanning Calorimetry

Thermal transitions of films, metal soaps, and pigments were recorded using a TA Instruments Q1000 differential scanning calorimeter. Samples were heated at a rate of 3°C per minute from a lower limit of either -50°C or -100°C to an upper limit between 150° and 500°C. The maximum temperature was restricted in order to minimize sample decomposition. For the same reason, samples were a few milligrams in size and were contained in aluminum hermetic pans. Straight-line baseline correction was used for most traces, necessitated in part by the small sample size.

## 1.4. Results

### 1.4.1. Macroscopic Properties

Few of the films examined were cohesive 12-22 years after manufacture. The unpigmented film was extremely sticky; the films that contained the inert pigments were mildly tacky and very soft. From the literature it is inferred that these films had not completely cured, and that it is possible they never would [2]. Similarly, the film pigmented with Naples Yellow was soft and easily dented, possibly because it was still in the early stages of oxidative crosslinking. Iron-based films were also soft and easily dented, but unlike with Naples Yellow, these properties were attributed to degradation that had followed complete crosslinking [2].

Only films made with White Lead (basic lead carbonate), Zinc White (zinc oxide), and Malachite (basic copper carbonate) were sufficiently cohesive for handling at ambient conditions. Both White Lead and Malachite films could be handled easily due to their moderate and high flexibilities. Zinc White films could be handled only with difficulty, with additional caution demanded by the older film, because they were extremely brittle. When attempting to measure crosslink densities via solvent swelling, it was found that none of these intact films swelled perceptibly in either dichloromethane, toluene, or cyclohexanone. On the other hand, most of the other films had readily washed away, indicating the absence of a percolating crosslinked structure.

Two borderline cases were presented by films containing Naples Yellow (lead antimonate) and Raw Sienna (iron oxide and clay). Both these films appeared initially to be only partially soluble in that some pigment was released into the solvent but the film fragments remained intact; however, after some mechanical agitation, both these films had dissolved completely. Unfortunately, both films were too fragile at ambient temperature to effect sample preparation and loading for thermo-mechanical analysis. As a result, that aspect of this investigation focused on those pigments that caused their paints to remain intact.

#### **1.4.2. Scanning Electron Microscopy**

The microscopic structures of the films were explored by SEM (Figure 1.2). No clear image of the Malachite film was obtainable due to its fragility, as significant fractions of the material were destroyed while focusing the electron beam. Films pigmented with iron were more fragile yet. Nonetheless, all three intact films had morphologies that were distinct from the pigment particles and from one another. The film pigmented with Malachite had a uniform corrugated surface likely owing to a fine pigment particle size. In the film containing Zinc White, nearly all the regions between the pigments were spanned by a foamy, web-like structure. The film containing the White Lead pigment was marked by a multitude of small clusters that were on the order of 200 nm in diameter. Most such clusters were located on the surface of the pigment particles, but there appeared a minority that was separate from the pigments. It is possible that at these sites, lead ions that leach from the White Lead particles nucleate the formation of soaps which at later stages break down the pigment [4, 10-11, 16, 18, 29].



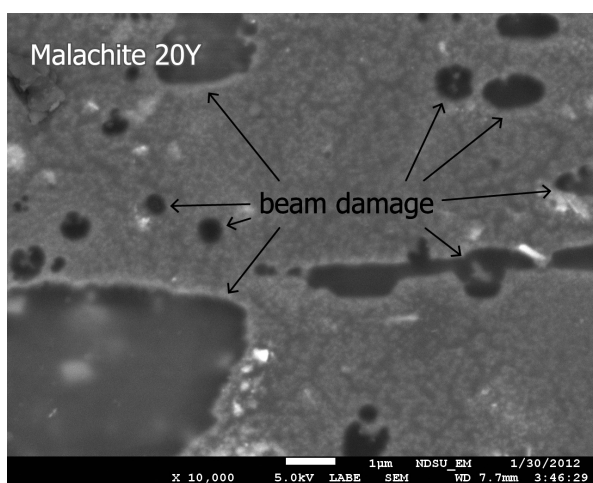
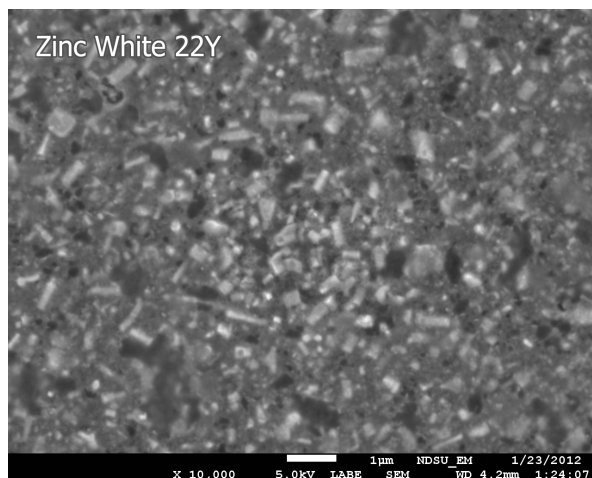
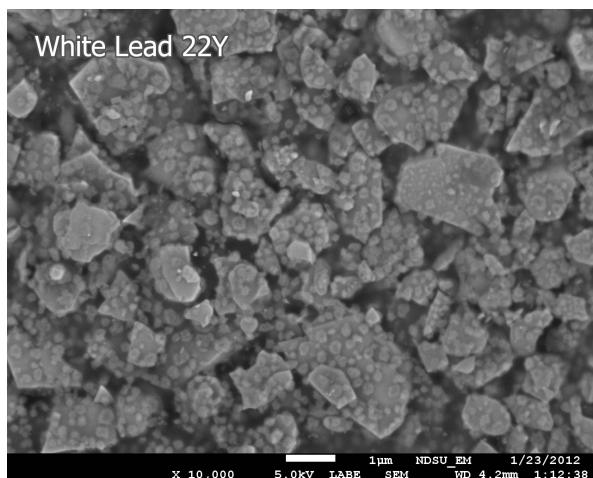


**Figure 1.2.** Scanning electron microscope backscatter images of oil paint films. Each film's age at the time of testing and its constituent pigment are labeled. Magnification is specified by the 1 μm marker below each image.

The pigment particles were many times larger for White Lead than for Zinc White, and they could not be unambiguously discerned for Malachite. In each case, energy dispersive X-ray analysis was consistent with metal atoms being distributed throughout the film rather than confined to the pigment particles. However, because EDS is not surface-specific, the possibility remained that the signal that was collected over the outer organic regions included contributions from pigment particles that were located in the interior of the film.

### 1.4.3. Infrared Spectroscopy

FTIR is used extensively in art conservation due to its ability to extract large volumes of information from extremely small sample sizes, a consideration that goes beyond convenience due to the field's need to minimize damage to the paintings being conserved. Since the validity of this technique is well-established, the present paint library was studied by FTIR before proceeding on to more novel

techniques. Infrared spectra were collected and all absorption bands were assigned to their originating sources in order to separate organic and organometallic features from features that are due to pigments and pigment impurities. This is important because locations of some characteristic organic bands coincide with locations of bands that are exhibited by some common pigment impurities, so without a complete assignment, these impurity bands are easy to misinterpret as organic in origin. Band attributions are detailed in Appendix A. Fortunately, consideration of only three markers is sufficient in order to understand the key features of these IR spectra: one for intact triglyceride esters, one for carboxylic acids, and one for metal carboxylates.

Carboxylic acids and triglyceride esters are best identified by their C=O bands which are located at  $\sim 1710$  and  $\sim 1740$   $\text{cm}^{-1}$ , respectively. (Hereinafter, these bands will be referred to as acid and ester bands, since other IR-active bands that are exhibited by acids and by triglyceride esters are not discussed in this chapter.) The relative intensities of these bands may be used to estimate the relative prevalences of each functional group within the film. However, it should be cautioned that, given the absence of an inert internal standard, quantitative determinations are unlikely to be reliable due to the apparently nonlinear relationship between peak intensity and the amount of material in the sample [28]. Fortunately, qualitative estimates are sufficient for meeting the present goals.

The acid band at  $\sim 1710$   $\text{cm}^{-1}$  was essentially absent from the spectra of the fresh linseed oils because cold-pressed linseed oil contains few fatty acids that are not bound in triglycerides. However, for the aged films, the acid band was clearly distinct from the ester band in the spectra of the unpigmented film, of the films containing inert pigments, and of the films containing iron-based pigments. (Detail of the film pigmented with Raw Sienna, an iron-based pigment, is included in Figure 1.3. Complete spectra are provided in Appendix A.) Since carboxylic acids are produced by oxidative degradation of the film, the distinct acid band indicates that considerable degradation had taken place. This is consistent with the macroscopic observation that these films had but minimal cohesion.

Further, for the unpigmented film and for the films containing inert pigments, the ester bands were more intense than the acid bands. However, the situation was reversed for the films containing iron-based pigments, whose acid bands were stronger than their ester bands, which suggests that the

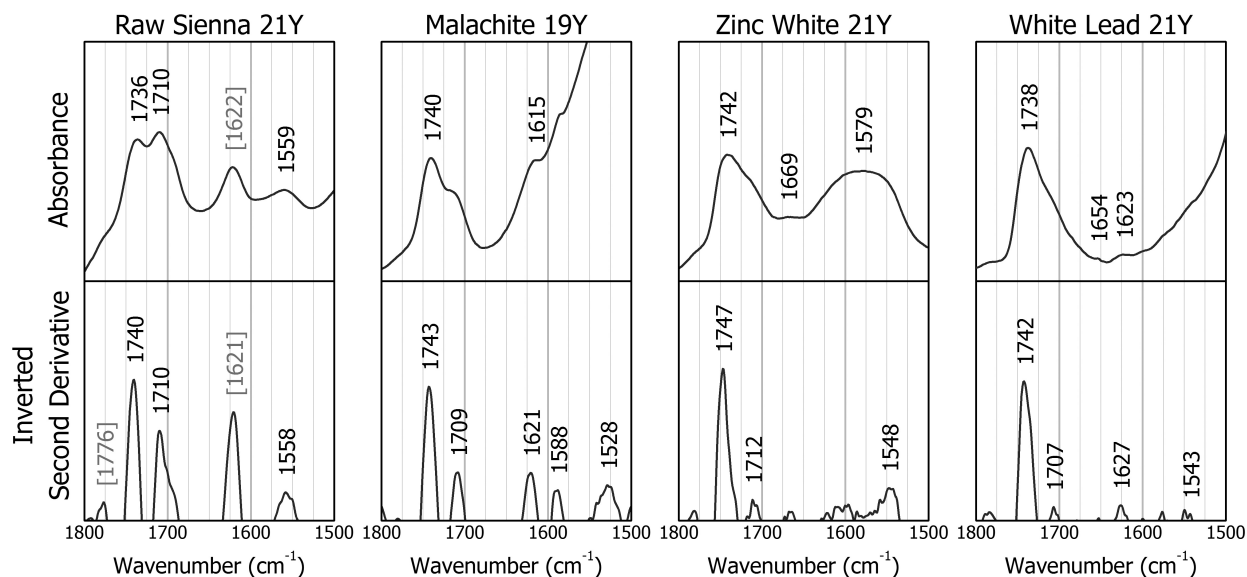


**Figure 1.3.** Details of infrared spectra of selected oil paint films. Each film's age at the time of testing and its constituent pigment are labeled. Maxima on the inverted second derivative spectrum are used to resolve shoulder peaks on the normal spectrum. [Square brackets] indicate pigment bands.

iron-based pigments accelerated degradation processes. This is not surprising because transition metals including iron are well-established in their use as pro-degradants, i.e., as compounds that are added to plastics in order to accelerate their degradation after the end of their intended service life [30].

(Premature breakdown of products that contain pro-degradants is typically countered by the simultaneous addition of antioxidants.) In particular, iron, which is commonly added to plastics in the form of iron stearate, acts as a photoinitiator for the decomposition of hydroperoxides into free radicals. In linseed oil, such alkoxy ( $RO\bullet$ ) and peroxy ( $ROO\bullet$ ) radicals react further through processes that may be categorized as either polymerization or degradation. In older films that had initially cured, such as the iron-based films in this study, few double bonds would remain, so their further polymerization would become unlikely and degradation would be expected to predominate. This explains the higher extent of degradation, signified by a higher acid content, in the present iron-containing films relative to the controls.

The carbonyl bands of the films that retained their cohesion – those pigmented with Malachite, Zinc White, or White Lead – were categorically different from the respective bands of the degraded films (Figure 1.3). The intact films exhibited acid bands that were considerably weaker than the acid bands of

the incoherent films. They were not distinct on the normal absorbance spectra where they appeared as shoulders off the more intense ester bands, but they were resolvable as peaks on the inverted second derivative spectra. The intensity of the acid band was by far the highest for the film pigmented with Malachite, followed by Zinc White, and then by White Lead. The lowering of intensities of the acid bands compared to the control may have been caused by pigments inhibiting network degradation. Alternately, this may have occurred if acids that were initially formed by degradation were later consumed by a reaction with free metal ions to form metal carboxylates. If this last scenario were dominant, then the abundances of metal carboxylates would be ordered oppositely of the intensities of the acid bands. Indeed, in the field of art conservation, lead carboxylates are encountered with the highest frequency within paintings, followed by zinc carboxylates, followed by copper, - which suggests their likely abundances within the present set of films.

Unfortunately, although all three spectra show evidence of metal carboxylates, the carboxylate features are partially masked by the adjacent pigment absorptions, so reliable estimates of their concentrations cannot be made based on the present spectra. Metal carboxylates are usually identified by their asymmetric  $\text{COO}^-$  stretch both because it is the strongest carboxylate band and because it occurs between  $\sim 1590\text{-}1540\text{ cm}^{-1}$ , a spectral region which in oil paint is often free from coinciding absorptions. The exact location of this band depends on factors that affect the strength of the bond between the metal and the  $\text{COO}^-$  moiety, which include the electronegativity of the metal, its the coordination state, and the identity of the fatty acid ligand [28, 31-33].

For the film pigmented with Zinc White, the asymmetric  $\text{COO}^-$  band appeared as a broad absorption with a maximum at  $1579\text{ cm}^{-1}$ . This wide band corresponded to a complicated set of peaks on the second derivative spectrum which suggests a diverse coordination structure [28]. For the film pigmented with Malachite, the presence of carboxylates was similarly unambiguous: the asymmetric  $\text{COO}^-$  band was a shoulder off a strong pigment absorption at  $1506\text{ cm}^{-1}$  on the normal spectrum and a single peak on the second derivative spectrum (which was located at  $1588\text{ cm}^{-1}$ ). For the film pigmented with White Lead, however, the presence of carboxylates was less distinct, as the asymmetric  $\text{COO}^-$  band was nearly negligible even on the second derivative spectrum (at  $1543\text{ cm}^{-1}$ ). The reason for this lack of

clarity is the strong and broad pigment absorption that is adjacent ( $1405\text{ cm}^{-1}$ ) to the  $\text{COO}^-$  band. For example, in a literature study of similar films (i.e., linseed oil pigmented with White Lead and naturally aged for several decades), the asymmetric  $\text{COO}^-$  bands were similarly subtle on the normal and the second-derivative spectra, but they became distinct after subtracting the pigment's spectrum [28]. Unfortunately for the present study, the pigment that had been used to manufacture the original film was no longer available. Since artists' pigments are not chemically pure, a different sample of White Lead would likely have had a different IR spectrum, so spectral subtraction was not performed here. However, the assignment of metal carboxylates to the film pigmented with White Lead was supported by a weak absorption at  $1623\text{ cm}^{-1}$  on the normal spectrum [28, 34].

Overall, IR analysis showed that all the intact films contained metal carboxylates, even though their concentrations in the films could not have been gauged due to interference from pigment absorptions. In contrast, no evidence of metal carboxylates could be similarly located in the spectra of any of the films that had lost their cohesion – with one exception, that of Raw Sienna. That film's asymmetric  $\text{COO}^-$  band is clearly visible on its IR spectrum at  $1559\text{ cm}^{-1}$ . In contrast, the film pigmented with Yellow Ochre, whose composition is nominally the same as Raw Sienna ( $\text{Fe}_2\text{O}_3$  and clay), did not exhibit evidence of metal carboxylates and did not retain cohesion. Further, iron carboxylates have their asymmetric  $\text{COO}^-$  band at higher wavenumbers,  $1573\text{ cm}^{-1}$  or above [32]. Therefore, the metal involved in this carboxylate complex was not iron but, rather, one of the metals present in the clay. Clay compositions vary widely by origin [35-37], and at present, the identity of this metal is unknown. More interesting, however, is that Raw Sienna was one of the two pigments whose films exhibited borderline cohesion. (The spectrum of the other borderline film was very poor so the presence of carboxylates in that film was indeterminate.) This all suggests that metal carboxylates do, indeed, act to cohere the films.

#### **1.4.4. Dynamic Mechanical Thermal Analysis**

DMA is a standard characterization technique in coatings, but not in the study of cultural heritage materials. Its large sample requirements render it unsuitable to the analysis of intact paintings, and the data it provides are not immediately relevant to the questions of conservation. Consequently, oil paint

models have been studied by DMA only once before [38]. However, that study considered only the near-ambient temperature range in which some compelling features of these traces are not yet explicit (Figure 1.4).

The  $\tan \delta$  plots of the present films are much more complex than those usually seen in coatings, and they extend to far higher temperature ranges before sample decomposition and rupture terminate the test. These plots concur with the macroscopic observations. The film pigmented with Zinc White has a far larger fraction of its peaks at high temperatures than the other films do. The consequently small fraction of its relaxations that occurs near ambient conditions is consistent with its observed hard and brittle behavior. The film pigmented with White Lead has a relaxation spectrum that is broad and fairly even, which correlates to mechanical stability over a range of near-ambient temperatures. The relaxation spectrum of the Malachite-pigmented film is nearly equally broad, but because its  $\tan \delta$  peak is much

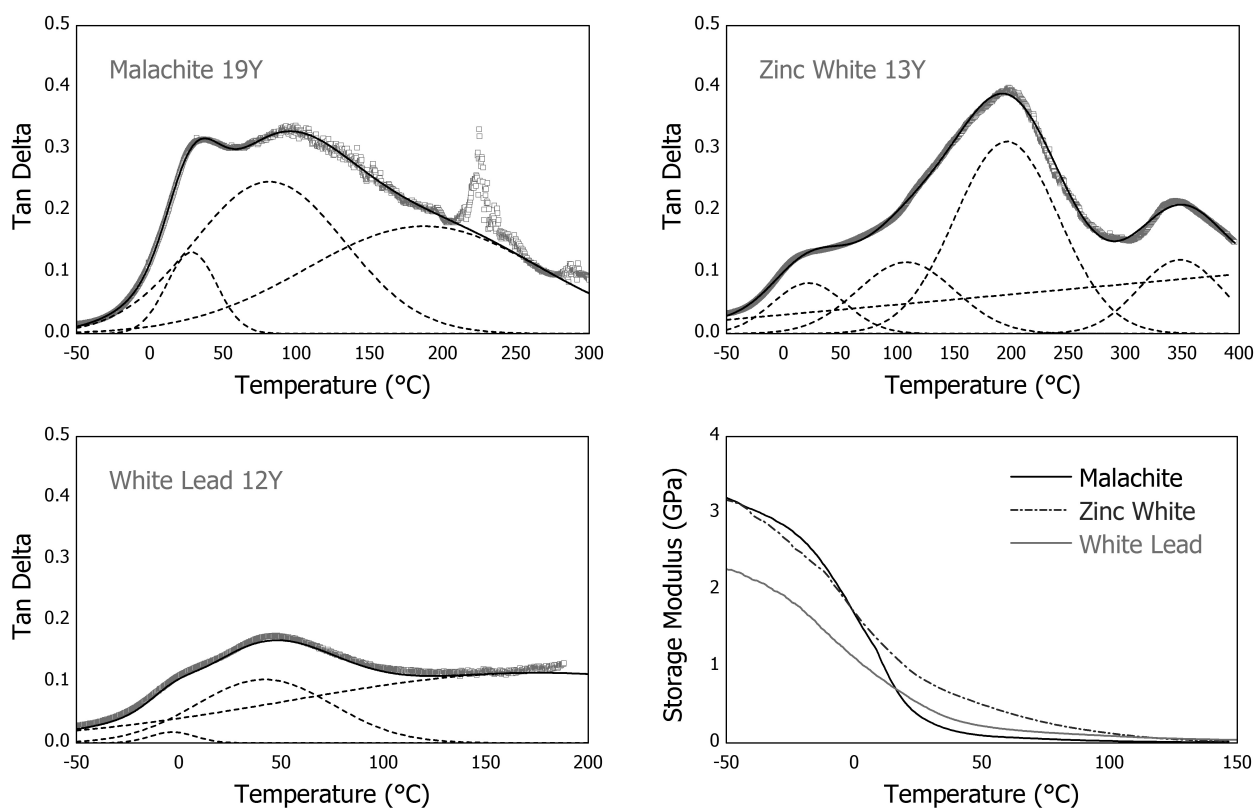


**Figure 1.4.**  $\tan \delta$  and storage modulus plots of aged oil paint films. Each film's age at the time of testing and its constituent pigment are labeled. (Results were qualitatively similar for the older films that contained the same pigments so only one dataset per pigment is shown.) On the  $\tan \delta$  plots, solid lines indicate Gaussian curves that were fit to each peak while dashed lines indicate the Gaussian components.

higher, it is much softer and more flexible than the White Lead film at ambient conditions. (Since  $\tan \delta$  is the ratio of the loss modulus to the storage modulus,  $E''/E'$ , high values of  $\tan \delta$  indicate samples that are more viscous while low values, samples that are more elastic.)

Notably, none of these films exhibit a conventional single peak that could easily identify a value of the glass transition temperature,  $T_g$ . Complex  $\tan \delta$  plots are well-known in some polymeric systems – ionomers, polymer blends having bimodal distributions of molecular weight, copolymers having incompatible blocks, some semicrystalline polymers, – but the physical processes that give rise to multiple peaks vary widely from system to system. Such complex plots are often deconvoluted into Gaussian components. There exists no theoretical basis that explains the shape dependence of  $\tan \delta$  on temperature. However, the Gaussian line shape is established empirically as providing fits far superior to those obtained using the Lorentzian function [39]. Nonetheless, such deconvolution should be used only with caution when the  $\tan \delta$  peaks are asymmetrical, as with the current data, since the glass transition peak is not expected to be symmetrical in all cases. Therefore, broad and shallow Gaussian peaks cannot be unequivocally assigned to physical processes unless corroborated by external evidence, since they may alternately be artifacts of the symmetrical fitting procedure [39].

Here, each of the films is expected to experience a glass transition due to the motions in the amorphous regions of the crosslinked network. This transition should be similar across the different films because the amorphous regions of the same starting drying oil should not be affected greatly by the constituent pigments. However, if some pigments produce additional structures, such new morphologies may exhibit additional relaxation peaks.

Only one of the Gaussian peaks appears in a consistent manner across all films and may, therefore, be due to the bulk glass transition. This peak is centered at 25-45°C and has comparable heights and areas across the five samples. Further, this temperature region agrees with the primary drop in the storage modulus, which occurs between approximately -30 and +30°C. (Features that are associated with the glass transition occur at lower temperatures on the storage modulus plot than the  $\tan \delta$  plot.) Unfortunately, the differences in peak heights and areas are not statistically significant

because repeatability was poor – i.e., two samples from the same film produced qualitatively similar but quantitatively different  $\tan \delta$  curves. Nonetheless, this assignment of the bulk glass transition is useful because the remaining  $\tan \delta$  peaks may then be considered in relation to the glass transition peak: those that occur at lower temperatures (e.g. in White Lead) must be due to structures that are more mobile than the bulk of the network, while peaks located at higher temperatures indicate structures whose motion is more constricted.

Finally, it should be noted that the maximum of the  $\tan \delta$  peak is not the glass transition temperature in a rigorous sense. This is important for the present set of films because they have not been exposed to temperatures above ambient so they would not be able to achieve a  $T_g$  above 25°C (such as 42°C for White Lead) due to vitrification. While  $T_g$  is commonly identified from the  $\tan \delta$  maximum, this is done primarily due to this measure's good repeatability. The drop in the storage modulus is not always sharp so identification of its onset or midpoint often is operator-dependent. Similarly, the loss modulus peak is at times difficult to observe, but the  $\tan \delta$  peak is unambiguous. Of these DMA metrics, the loss modulus peak is perhaps the closest to the true  $T_g$ . For the present samples, this occurs at -4°C for the film of Zinc White and at 4°C for White Lead and Malachite. (Supplementary data are shown in Appendix C.) Therefore, all the films are above  $T_g$  at ambient conditions, consistent with the expectations.

#### **1.4.5. Differential Scanning Calorimetry**

DSC may be instrumental in identifying the  $T_g$  to complement the DMA data. However, DSC is far less sensitive than DMA, so oftentimes, the transition is missed altogether. Such was the case for the present set of samples: although DSC thermograms of the films had many weak features in the region of interest, none of them could be unambiguously assigned to  $T_g$ . (Data are shown in Appendix C.) This was not surprising, because thermosets have a smaller amorphous fraction than non-crystalline thermoplastics, and the glass transition is experienced only by the amorphous material. The effect on the heat capacity of the sample that is measured by DSC is consequently less strong in accord.



A far more pressing question was to the sources of the additional relaxation peaks that were seen on the  $\tan \delta$  plots. IR had shown that metal soaps were present within the intact paint films. The next question was, then, whether any of the relaxations observed by DMA may be attributed to metal soaps – i.e., whether any of the  $\tan \delta$  peaks correlate with phase transition temperatures of any of the soaps that may assemble within the aged paint films. To this end, a set of metal soaps was synthesized and used as reference standards. Conservation literature establishes that only three fatty acids – azelaic, palmitic, and stearic, – comprise the bulk of the monomeric content in aged oil paint films [5, 14-15]. The reference library was assembled of azelate, palmitate, and stearate soaps to reflect this.

Phase transitions of metal soaps are often characterized by DSC. Although DSC is less conclusive than optical microscopy for the identification of phase transition temperatures in pure samples (because processes other than melting exhibit endotherms that manifest on DSC thermograms), DSC has the advantage for the present study in that it is capable of detecting thermodynamic processes not only in soap standards but also in the composite paint films. For this reason, DSC was used to characterize the soaps as well as the films. Further, to narrow the investigation's focus to phase transitions other than decomposition (such as melting), TGA was used to identify temperatures at which soap standards lose weight, and this data was correlated with DSC endotherms, as summarized in Table 1.4. (DSC thermograms and TGA plots that were used to compose this table are provided and discussed in Appendix B.)

In order to decide whether a given endotherm exhibited by a soap standard corresponds to an

**Table 1.4.** Locations of features (°C) observed by thermal analyses of the oil paint films and the corresponding metal soaps. For the films pigmented with Zinc White and White Lead, data are shown for the younger films to enable comparison with  $\tan \delta$  plots in Figure 1.4. The copper-containing pigment was Malachite. DMA features are the locations of the Gaussian peak components. Numbers in (parentheses) indicate soap DSC peaks that correspond to sample decompositions identified by TGA. ~~Strikethrough~~ denotes features of soap standards that were assigned to impurities of the starting reagents. **Bold** highlights corresponding sets of features for each metal.

	Zn	Pb	Cu
DSC, azelate soap	<b>360</b>	( <del>289</del> ), ( <b>382</b> ), (467)	<del>80</del> , (269), (283), (302)
DSC, palmitate soap	133	107, 113, (274-289)	99, 101, 114
DSC, stearate soap	131	110, 114	100, 103, 116
DSC, paint film	<b>329</b> , 422	203, 263, <b>274</b> , 340, <b>373</b> , 396	220, 302
DMA, paint film	32, 108, 196, <b>348</b> , +	-3, 42, 176, +	29, 82, 187

endotherm on the paint film's thermogram, the sensitivity of DSC to likely experimental inconsistencies must first be considered. The properties of metal soaps are notoriously sensitive to the methods that are used to synthesize them due to the many types of compounds that are often produced [32, 40-41]. A given metal cation may have one, two, or (in the case of iron) three fatty acid ligands, with any remaining valences being filled by OH<sup>-</sup> anions from the aqueous reaction medium, or by anions from the salt that was used as the starting reagent due to incomplete reaction. Alternately, the cation formed by the reaction may be much more complicated, such as [Fe<sub>3</sub>O(St)<sub>6</sub>(H<sub>2</sub>O)<sub>3</sub>]<sup>+</sup> for iron(III) stearate [32]. Further, dicarboxylic fatty acids including azelaic may bridge two metal centers when the reaction with the metal proceeds to completion [15], but incomplete reaction is likely to produce mixtures of mono- and di-azelate complexes. However, even unobvious purity problems are commonplace, including the presence of starting acids in the final soap products.

All these factors strongly affect the melting points of the soaps. In one literature study, melting points of several products that were all intended to be iron stearate had been found to range from 61 to 118°C [32]. This is an extreme example, wherein much of the variation was explained by the presence of unreacted stearic acid in some of the (commercial) products. Nearly-pure iron stearate complexes that were synthesized as part of that study had much less variation among their melting points, 110-118°C. Nonetheless, this example is instructive because it highlights the uncertainty inherent in the present attempt to relate transitions of fairly pure soap standards to transitions of soaps that are situated within paint films, since the films may be alternately conceptualized as soaps suffering from extremely high levels of impurities.

Returning to the DSC results, only films pigmented with Zinc White or White Lead had features that were comparable to any of the soap standards – and, with that, only those of metal azelates (Figure 1.5). The correlation between the thermograms of zinc-based soaps and films was particularly explicit since there was no sample decomposition to complicate the interpretation, and since the endotherms had sharp shapes consistent with melting. Between the lead-based samples, the relationship was not as obvious because both the thermograms contained combinations of sharp and broad features, and since TGA showed that lead azelate decomposed during both of the sharp peaks whose locations correlated

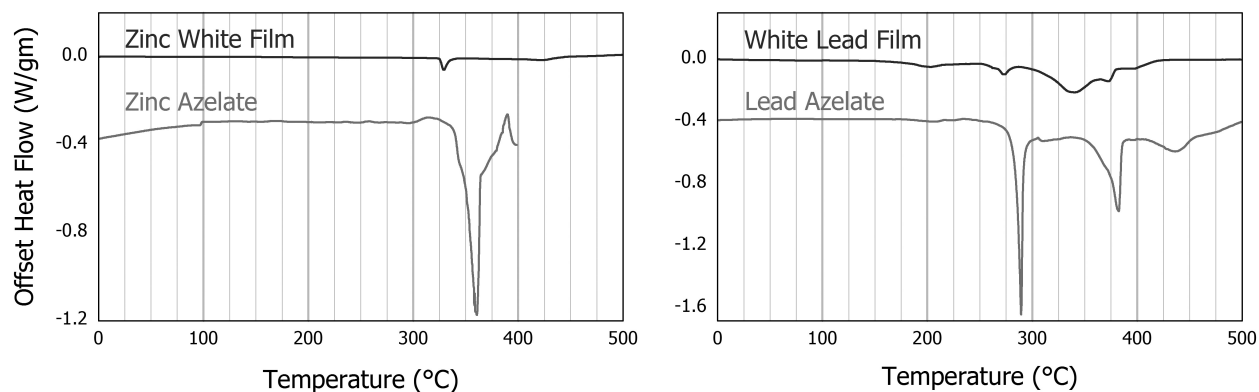


**Figure 1.5.** DSC thermograms of selected oil paint films and the corresponding metal azelates. Thermograms are shown for the younger films in order to correlate with the  $\tan \delta$  plots in Figure 1.4.

with the White Lead film. Nonetheless, the endotherm located at 289°C was tentatively assigned to melting – because melting was consistent with the asymmetrical peak shape, and because the corresponding TGA weight loss was near-negligible at 0.65 wt%, whereas the DSC endotherm was quite strong.

In addition, DSC may be considered simply as a fingerprinting technique, and for that purpose, any correspondence would suffice. However, the finding of melting is additionally interesting because melting could potentially be the source of some of the DMA features. Indeed, Zinc White film's DSC endotherm at 329°C is consistent with its  $\tan \delta$  peak at 348°C. (Physical processes are usually observed at higher temperatures on  $\tan \delta$  plots than on DSC thermograms.) Unfortunately, a similar connection cannot be conclusively made for the film pigmented with White Lead because it decomposes before the DMA temperature sweep is able to approach 289°C.

No copper or iron-based soaps were observable by DSC. The thermogram of the film pigmented with Malachite had only broad and weak features. An endotherm at 220°C was consistent with decomposition of the copper carbonate pigment, and a broad shallow endotherm at 302°C had a shape which also suggested a process other than melting. Similarly, thermograms of iron-based films were nearly featureless, although an exception was provided by the film pigmented with Raw Sienna, which exhibited some very weak features. However, those features did not match iron azelate, palmitate, or

stearate standards – in accord with the IR finding that this film contained carboxylates of a metal other than iron.

This inability of DSC to find soaps in the Malachite-pigmented film, despite the IR finding to the contrary, is disappointing but not surprising. In order for a constituent to demonstrate an endotherm by DSC, it must form sizable phase domains within the bulk material. For example, in a related matter, the smallest domain size that can experience a glass transition has been estimated as  $(50-100 \text{ \AA})^3$  or  $150 \text{ \AA}$  in segmental length [42-44]. Further, the melting point of a crystalline phase scales inversely with its size, as described by the Gibbs-Thomson equation, so for a melting point of a phase to have a value similar to the bulk material, it must have crystalline domains that are at least 10s of nanometers in extent [45]. The absence of calorimetric evidence indicates only that soap structures that are present in the films are not large and organized enough to be observable by DSC.

An illustrative example is provided by an external study which analyzed the same lead-based films that are discussed here, but using a technique which is much more sensitive than DSC, Time-of-Flight Secondary Ion Mass Spectrometry (ToF-SIMS) [46]. Data collected as part of that study are included for convenience in Appendix D. Although lead azelates appeared to be the most abundant soap within each White Lead film, lead palmitates and lead stearates were also present. Yet, these palmitate and stearate soaps did not manifest DSC features ( $\sim 110^\circ\text{C}$ ) on the thermograms of the White Lead films. Unfortunately, as of this writing, ToF-SIMS analyses of the remaining films in this collection have not been performed.

## **1.5. Discussion**

### **1.5.1. Introduction**

This study examined a library of model oil paint films that had been prepared from only cold-pressed linseed oil and inorganic pigments. Most films had been drawn down 20-22 years ago; some supplementary younger films were 12-13 years old. In addition to several inert pigments, the library contained four pigments that were known to react with the linseed oil medium: those containing iron, lead, zinc, and copper. The main goal was to understand the mechanisms by which pigments impart very different physical and mechanical properties to their containing films.

Iron-based films had cured initially but they lost all their mechanical integrity shortly after. IR analysis had shown that iron-based films were more hydrolyzed (contained more acid) than controls, which were the unpigmented film and the films containing the inert pigments. This effect is well-known in the field of art conservation, as well as outside of it, since iron is used widely as a pro-degradant. The remainder of the investigation focused on the three pigments that caused oil paint to remain intact – White Lead, Zinc White, and Malachite.

IR analysis had shown that all three of these intact films contained metal carboxylates, or soaps of metals with fatty acids. For over a century, soap formation has been said to cohere oil paint films, but this subject did not attract much attention until the late 90s, when disfiguring lumps protruding from oil paintings, that are now known to be very common, were first conceived [9] to be the product of metal soaps. Since then, art conservation research has focused on questions relevant to the formation of these protrusions, such as identifying their constituents (and finding mineralized metal compounds at their centers) as well as considering the mobility of fatty acids through the oil paint films. However, comparatively little attention has been given to the effects of soaps outside of such aggregates, which is the interest of the present study.

### **1.5.2. Current Working Model of Mature Oil Paint**

It is generally thought that, after 50-100 years, the crosslinked network is no longer intact because too many ester bonds have by that time been hydrolyzed [6-7, 47-48]. Instead, it is often said that paint films are cohered by an ionomeric network of metal soaps, with metals originating from pigments and from driers [6, 29]. According to this model, a coordination network is formed when multivalent metal cations are bridged by diacids that are present in the film, azelaic and otherwise, as shown schematically in Figure 1.6. In the younger films (such as the ones in the present study), the covalent network is linked to the coordination network at some junctures. This could happen, for instance, when an unsaturated fatty acid is hydrolyzed at the double bond yet is still bonded to the triglyceride ester, and the hydrolyzed moiety becomes coordinated to a metal cation. Monoacids including palmitic and stearic are also coordinated to the metal cations, but since monoacids are coordinated at only one point rather than chelated to the network, they become detached from the network much more

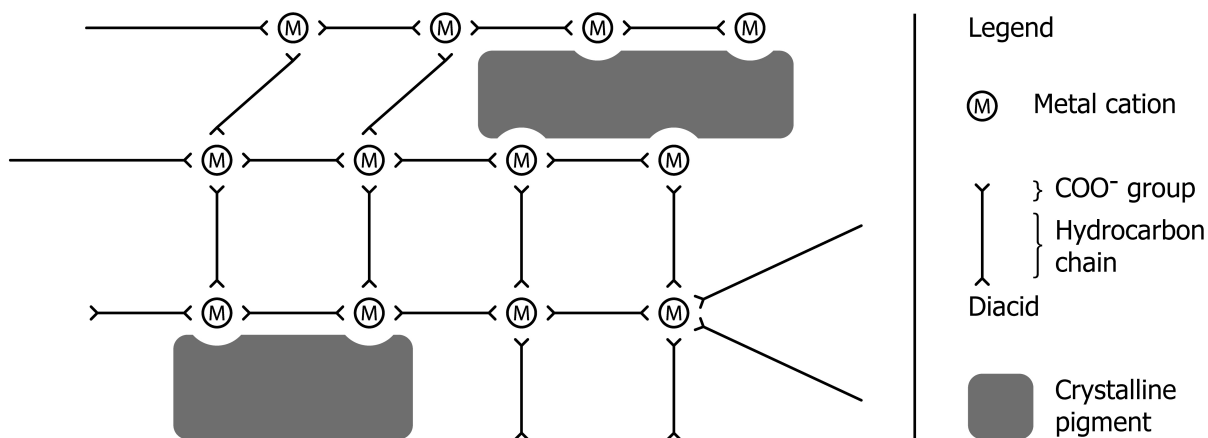


**Figure 1.6.** Schematic of the existing working model for metal-coordinated oil paint, redrawn from [32].

easily than do azelates. This explains why the unsightly protrusions that are found in lead- and zinc-pigmented paintings contain metal palmitates and stearates, but not metal azelates.

Conversely, it has been remarked that metal cations cannot function as crosslinks in accord with this model to an extent that is significant enough to appreciably impact the mechanical properties of the paint [8, 49]. The abundance of metal ions in oil paint is often much higher than the concentration of acid groups in the material. This varies widely depending on the pigment, as some pigments decompose into ions much more readily than do others. An illustrative example is provided by the ~20-year-old lead-based paints in the current study (Appendix D). For the film pigmented with White Lead (basic lead carbonate), the concentration of free lead ions is two orders of magnitude higher than the concentration of free acids. Meanwhile, for the film pigmented with Naples Yellow (lead antimonate), the concentrations of free lead and free acids are on the same order. As a result, for both films – but especially for the one pigmented with White Lead – it is improbable that one metal cation would be coordinated to multiple fatty acid ligands.

The above argument is strengthened by considering that, in order to function as a crosslink rather than as a chain extender, the metal cation would require not just two, but at least three fatty acid ligands. However, many metals that are said to be involved in this coordination network – lead, zinc, copper – are incorporated into the paint in a +2 oxidation state. No suggestion has been made that the metals are oxidized to a +3 or +4 state to enable coordination to three or four ligands, and indeed for

zinc, higher oxidation states are not possible. As a result, zinc cations cannot function as crosslinks, and the ability of lead and copper cations to function as crosslinks is almost as doubtful.

Overall, the present working model for oil paint [6, 29] is crucially flawed. In order to function as a crosslink, a metal cation must be coordinated to three or more fatty acid ligands. However, many metals of interest are incorporated into paint in a divalent state, and some (notably, zinc) are incapable of higher coordination states. In addition, the concentration of free metal in oil paint (notably, lead) may be much higher than the concentration of the fatty acid groups, which renders the coordination of a single metal to multiple acids highly improbable, even when steric and mobility difficulties are ignored. Plainly, metal cations cannot function as crosslinks. However, this model is widely used because (to this author's knowledge) no alternative has yet been proposed.

### **1.5.3. Revised Working Model of Mature Oil Paint**

The recognition that this working model suffers from this particular set of problems becomes startling if one considers that mature oil paint is widely likened to ionomers, yet in the field of ionomers, individual metal ions are never said to function as crosslinks. Instead, physical crosslinks are due to *multiplets* of metal ions, which has key emergent effects on the properties of the resulting materials. Presently it is proposed that similar multiplets may form in oil paint, so in order to understand the structure of oil paint, a brief review of ionomers is in order.

Ionomers are a class of polymers that was first established in 1964 and is by now well understood [44]. Ionomers are polymers that contain low concentrations of ionic groups, typically through copolymerization of ionic and neutral monomers. The ionic groups are often sulfonate or carboxylate, but other ionic groups are also common. In most ionomers, the ionic moieties are pendant to the polymer backbone. End-functionalized (monochelic and telechelic) ionomers have been also studied as models for random ionomers, and they do not usually differ from random ionomers in their properties and morphologies. Of all the subclasses of ionomers, monochelic and telechelic polymers are the ones that bear the closest resemblance to the mono- and dicarboxylic fatty acids that are present in oil paint. However, as will be elaborated below, direct analogies between them and the fatty acids cannot be drawn due to stark differences in molecular weight. Indeed, the term telechelic originates from the

Greek words *telos*, far, and *chelos*, claw, thus describing a molecule that has two claws (such as COO<sup>-</sup> moieties) that are far apart [50] – whereas azelaic acid is only 9 carbons long. Further, polymers containing high concentrations of ionic groups are not classified as ionomers (and instead e.g. as polyelectrolytes) because their morphologies and properties have little in common with those of the ionomer class.

Nearly all ionomers fit the description of the cluster-multiplet model [44, 51] which is firmly established within the field. As explained by the model, just as individual ions are strongly driven to associate with counterions, ion pairs (anion-cation) are driven to aggregate with other ion pairs, and thus form quartets, octets, and larger *multiplets*. The driving force for this phenomenon is the lack of compatibility between ions and the nonpolar polymer media.

Since the multiplets consist of only several ion pairs, they are too small (6-8 Å) to manifest their own  $T_g$ , so they behave simply as physical crosslinks. However, additional phenomena arise because in the region immediately surrounding each multiplet, polymer mobility is reduced relative to that of the bulk material. This immobilization is due to several factors: the anchoring of the polymer chains to the multiplet, the crowding of chains near the multiplet, and the consequent chain extension. When the concentration of multiplets in the polymer is low, the material behaves similarly to a conventional polymer in that it has only one  $T_g$  that is due to the bulk matrix phase. When the concentration of multiplets is higher, regions of reduced mobility that are produced by the different multiplets overlap. When the concentration of multiplets is high, these overlapping regions of reduced mobility become large enough to behave as a separate phase (said to be a region greater than 50-100 Å), – at which point, they exhibit their own  $T_g$  which is much higher than the bulk. The term *cluster* describes a set of multiplets whose regions of restricted mobility behave as a separate phase.

One consequence that provides a bridge back to the present results is that the  $\tan \delta$  plots of many ionomers exhibit two distinct peaks, one due to the cluster  $T_g$  and one due to the matrix  $T_g$ . The  $\tan \delta$  plots of the oil paint films here had multiple peaks as well. However, whether or not these films have multiple  $T_g$ s is far from clear, and cannot be determined using DMA data alone. First, it is not



certain that ion groups aggregate into multiplets within oil paint films. Multiplets certainly would explain why many oil paint films remain intact after the covalent network disintegrates from hydrolysis, and they would explain this in a manner that is much more convincing than the current model for mature oil paint. However, obtaining direct evidence to the existence of such multiplets would be far from a formality. After 20 years of degradation, oil paint films may be fairly polar, so the driving force for phase separation may be low. In that case, ion pairs may not be driven to aggregate into multiplets. Second, fatty acids that are present in oil paint films have very low molecular weights as compared to the size of those segments that space apart ionic groups along ionomer chains. This is important because the size of the restricted mobility region in random ionomers is on the order of 10 Å [52], which is also approximately the size of azelaic acid, the most abundant diacid in oil paint films. Thus, even if multiplets were able to form within the oil paint films, nearly all the organic material would be in the restricted mobility regions, – provided that the coordination network spanned the entire film. This provision may be invalid in the 20-year-old films under study, which are not yet fully hydrolyzed [6-7], so the multiple  $\tan \delta$  peaks may still be attributable to multiple  $T_g$ s. However, no such attribution is warranted until the presence of ion clusters is established. Overall, while the multiplet model proposed here explains a wider range of phenomena than the existing model, many important questions remain to be answered so its validity is only tentative.

#### **1.5.4. Azelate Phases in Oil Paint**

Mature oil paint is notorious for its heterogeneity. In addition to structures that may assemble throughout the bulk of the paint that were discussed above, DSC showed that some metal azelates have formed discrete inclusions phase-separated from the polymer matrix. Namely, Zinc White paint contained domains of zinc azelate that were large and organized enough to exhibit an endotherm on the film's DSC thermogram. White Lead paint seemed to contain comparable domains of lead azelate, although that interpretation was less definitive. This discussion will, therefore, focus on the film of Zinc White.

Structures and thermal transitions of zinc azelate were not investigated in detail. However, the phase transition that was observed by DSC, whether it was melting or a liquid crystalline order-disorder transition, had occurred at similar temperatures in both the zinc azelate standard and the Zinc White film,

and the difference in temperatures was small enough to be attributable to the smaller domain size that would be expected to develop within the film. This suggests that zinc azelate has a similar packing arrangement when it self-assembles domains within the paint as it does in the fairly pure zinc azelate standard – an imperfect crystal.

The order-disorder transition of this phase was also observed as a distinct peak on the  $\tan \delta$  plot of the Zinc White paint. Since this relaxation transpired far above the  $T_g$  of the paint, its effect on the near-ambient mechanical properties was not explicit from the DMA data: for example, the modulus was already extremely low before the start of this relaxation since the rubbery state of the polymer matrix dominated the properties of the film. Yet, implicitly, from a composite standpoint, the assembly of previously amorphous material into crystalline domains would render their containing films stiff and perhaps also brittle. These are properties for which Zinc White paint is infamous in art conservation. It is, therefore, likely that the mechanical properties of Zinc White paint are dominated primarily by crystal formation, and not by the formation of a coordination network.

Since White Lead paint also stiffens with age, but to a far lesser extent than Zinc White, this could be because crystal formation is less favorable in the White Lead paint. For example, a literature SEM image of one cross-section of paint that contained White Lead showed an aggregate that was still amorphous even four centuries after preparation [4, 11]. More generally, soap aggregates in paintings are not yet fully understood, and there are other reported cases where paintings of similar age contain lead soap aggregates organized into lamellar structures [4, 10]. Nonetheless, lead soap domains in the current, much younger films are expected to be highly disordered. Of course, it is also possible that the mechanisms that increase the overall stiffness are different for lead as compared to zinc.

The likely crystalline structure of metal azelate domains warrants some further consideration. Although the structure of zinc azelate is not known, the crystalline structure of lead azelate had previously been reported [15]. Lead azelate forms a 3D structure with lead(II) cations linked by azelate bridges, in which infinite stacks of  $(\text{PbO}_4)_n$  units are connected by hydrocarbon chains that are arranged parallel to one another and perpendicular to the stacks. This framework of struts and joints can be appreciated from the perspective of metal organic frameworks (MOFs), crystals which find applications in

gas storage and catalysis as a consequence of their high porosity [53]. Unfortunately, within an intact film, the formation of such porous crystals would have an adverse effect on the properties of the paint: the polymer matrix would have to expand in order to accommodate the growing crystal, which would build up internal stress in a cohesive, elastic polymer.

If a crystal such as this continued to grow and expand, it would eventually distort and rupture its containing film, which is to say, it would form a protrusion. Indeed, lead azelates have been found in some protrusions in oil paintings, but importantly, always in combinations with palmitates and stearates [17, 19, 54-55]. Analyses of other protrusions have found lead palmitates and stearates but little or no evidence of azelates [14-15, 18]. (Analyses of zinc-based protrusions have been more limited and have not differentiated between the various zinc soaps [18, 20-21].) In the present study, although palmitates and stearates were present within the intact films, they did not constitute domains that were large enough to be observable by DSC. This tempers the connection between the azelate domains observed here and the protrusions found in centuries-old paintings, since in protrusions, monoacid domains are more pervasive. However, multiple mechanisms appear to be involved in the formation of protrusions [19], so the possibility that these azelate phase domains would grow over centuries into protrusions cannot presently be eliminated.

Overall, while any connection between azelate phase domains and protrusions is unclear, the finding of azelate phase domains in zinc- and, perhaps, lead-based paints remains important. Not only is this work the first instance when such phase domains have been observed, their presence in oil paint has not even been postulated. The crystalline (or liquid crystalline) nature of these inclusions warrants further study because it is likely that, for some metals, the mechanical properties of aging oil paint – i.e., increases in stiffness and brittleness – are due primarily to crystal formation, and not the formation of a coordination network. This last hypothesis could be tested by analyzing a series of relatively young Zinc White films as composites of crystals, pigments, and the polymer matrix.

## **1.6. Conclusion**

The present work examined a collection of model paint films that were prepared using only inorganic pigments and linseed oil and were stored under museum conditions for 12-22 years prior to

characterization. The goal was to explore how different pigments interact with this bio-based paint to produce, in the long term, widely different morphologies and mechanical properties. The focus of the investigation was on those films whose pigments enabled them to remain intact – Zinc White, White Lead, and Malachite. FTIR showed that these intact films (and one additional film of borderline cohesion) were the only ones to contain metal soaps. Since metal soaps have long been said to cohere oil paint films, this possibility was explored next in some further detail.

The present study had two notable findings – one from DMA, and one from DSC. Surprisingly,  $\tan \delta$  plots of each of these three films had multiple peaks that could be deconvoluted into Gaussian components. Such complex  $\tan \delta$  plots are seldomly seen in coatings. For the film pigmented with Zinc White, one of the  $\tan \delta$  peaks was assigned to an order-disorder phase transition (e.g. melting) of zinc azelate soap based on DSC data. Further, another peak that appeared at comparable temperatures across all films was tentatively assigned to the bulk glass transition. Other distinct  $\tan \delta$  peaks could not be assigned at present. However, since additional peaks may have been due to multiple glass transitions, – as in ionomers, which were discussed in detail, – these additional peaks suggested that complex morphologies were present which might be elucidated by a future structural investigation.

The second notable finding was that films pigmented with Zinc White contained phase domains of zinc azelate that were large and concentrated enough to be observable by DSC. Films pigmented with White Lead appeared to have similar lead azelate phases, although that determination was less certain. These phases were likely crystalline or liquid crystalline. The finding of these phases suggested that the stiffening and embrittling of oil paint films that is well-known to occur with age, particularly with zinc, may be due primarily to the formation of crystals, and not to the growth of a coordination network as previously thought. In addition, these discrete phases may be early precursors of protrusions which develop over centuries within paintings and which have been the subject of intense interest within the field of art conservation.

Identifying the mechanisms by which metal soaps of fatty acids are able to produce competent coatings is important now that fossil sources of raw materials are known to be unsustainable while the properties of bio-based polymers remain lacking. The present research has advanced the understanding

of structures that self-assemble within mature oil paint films, a subject that has bearing on the continued conservation of art and other cultural objects. It also shows that it may be possible to compensate for the effects of degradation by integrating the ensuing small molecular fragments into a secondary coordination network so that, on the balance, structural integrity is maintained.

## 1.7. References

- [1] M.F. Mecklenburg, C.S. Tumosa. Traditional oil paints: The effects of long-term chemical and mechanical properties on restoration efforts. *MRS Bull.* **2001**, *26*, 51-54.
- [2] M.F. Mecklenburg, C.S. Tumosa, E.P. Vicenzi. The influence of pigments and ion migration on the durability of drying oil and alkyd paints. In M.F. Mecklenburg, A.E. Charola, R.J. Koestler, Eds.; *New insights into the cleaning of paintings: Proceedings from the Cleaning 2010 International Conference*, Valencia, 26-28 May 2010. Smithsonian Institution Scholarly Press: Washington, D.C., **2013**, 59-67.
- [3] D. Rogala, S. Lake, C. Maines, M. Mecklenburg. Condition problems related to zinc oxide underlayers: Examination of selected abstract expressionist paintings from the collection of the Hirshhorn Museum and Sculpture Garden. *J. Am. Inst. Conserv.* **2010**, *49*, 96-113.
- [4] K. Keune, A. van Loon, J.J. Boon. SEM Backscattered-Electron images of paint cross sections as information source for the presence of the lead white pigment and lead-related degradation and migration phenomena in oil paintings. *Microsc. Microanal.* **2011**, *17*, 696-701.
- [5] J.S. Mills, R. White. *The Organic Chemistry of Museum Objects*, 2<sup>nd</sup> Ed. Butterworth-Heinemann: Oxford, **1994**, 35-40.
- [6] J.D.J. van den Berg, K.J. van den Berg, J.J. Boon. Chemical changes in curing and ageing oil paints. In J. Brigland, J. Brown, Eds.; *ICOM Committee for Conservation, Preprints of the 12<sup>th</sup> Triennial Meeting*, Lyon, 29 August-3 September 1999. James & James: London, **1999**, 1:248-253.
- [7] J.D.J. van den Berg. *Analytical Chemical Studies on Traditional Linseed Oil Paints*, Ph.D. Thesis, FOM Institute for Atomic and Molecular Physics, Amsterdam, **2002**.
- [8] D. Erhardt, C.S. Tumosa, M.F. Mecklenburg. Long-term chemical and physical processes in oil paint films. *Stud. Conserv.* **2005**, *50*, 143-150.
- [9] P. Noble, J. Wadum, K. Groen, R. Heeren, K.J. van den Berg. Aspects of 17<sup>th</sup> century binding medium: Inclusions in Rembrandt's *Anatomy Lesson of Dr. Nicolaes Tulp*. In J. Goupy, J.-P. Mohen, Eds.; *Art et Chimie, la Couleur: Actes du Congrès*, Paris, 16-18 September 1998. CNRS Éditions, Paris, **2000**, 126-129.
- [10] J.J. Boon, J. van der Weerd, K. Keune. Mechanical and chemical changes in Old Master paintings: Dissolution, metal soap formation and remineralization processes in lead pigmented ground/intermediate paint layers of 17<sup>th</sup> century paintings. In R. Vontobel, Ed.; *ICOM Committee for Conservation, Preprints of the 13<sup>th</sup> Triennial Meeting*, Rio de Janeiro, 22-27 September 2002. James & James: London, **2002**, 1:401-406.
- [11] K. Keune, P. Noble, J.J. Boon. Chemical changes in lead-pigmented oil paints: On the early stage of formation of protrusions. In R. van Grieken, K. Janssens, L. Van't dack, G. Meersman, Eds.; *Proceedings of ART 2002, the 7<sup>th</sup> International Conference on Non-Destructive Testing and*

*Microanalysis for the Diagnostics and Conservation of the Cultural and Environmental Heritage*, Antwerp, 2-6 June 2002. University of Antwerp: Antwerp, **2002**, 1-9.

- [12] P. Noble, J.J. Boon, J. Wadum. Dissolution, aggregation and protrusion. Lead soap formation in 17<sup>th</sup> century grounds and paint layers. *ArtMatters* **2002**, *1*, 46-61.
- [13] J. van der Weerd, J.J. Boon, M. Geldof, R.M.A. Heeren, P. Noble. Chemical changes in Old Master paintings: Dissolution, metal soap formation, and remineralization processes in lead pigmented paint layers of 17<sup>th</sup> century paintings. *Z. Kunsttechnol. Konserv.* **2002**, *16*, 36-51.
- [14] C. Higgitt, M. Spring, D. Saunders. Pigment-medium interactions in oil paint films containing red lead or lead-tin yellow. *National Gallery Technical Bulletin* **2003**, *24*, 75-91.
- [15] M.J. Plater, B. De Silva, T. Gelbrich, M.B. Hursthouse, C.L. Higgitt, D.R. Saunders. The characterization of lead fatty acid soaps in 'protrusions' in aged traditional oil paint. *Polyhedron* **2003**, *22*, 3171-3179.
- [16] J.J. Boon, E. Gore, K. Keune, A. Burnstock. Image analytical studies of lead soap aggregates and their relationship to lead and tin in 15<sup>th</sup> C lead tin yellow paints from the Sherborne triptych. In M. Picollo, Ed.; *Proceedings of the Sixth Infrared and Raman Users Group Conference (IRUG6)*, Florence, 29 March-1 April 2004. Il Prato: Padova, **2005**, 66-74.
- [17] J. Boon, K. Keune, J. Zucker. Imaging analytical studies of lead soaps aggregating in preprimed canvas used by the Hudson River School painter F.E. Church. *Microsc. Microanal.* **2005**, *11*(Suppl 2), 444-445.
- [18] K. Keune. Chapter 5 in *Binding Medium, Pigments and Metal Soaps Characterised and Localised in Paint Cross-Sections*, Ph.D. Thesis, FOM Institute for Atomic and Molecular Physics, Amsterdam, **2005**.
- [19] K. Keune, J.J. Boon. Analytical imaging studies of cross-sections of paintings affected by lead soap aggregate formation. *Stud. Conserv.* **2007**, *52*, 161-176.
- [20] K. Beltinger, G. Englisch, D. Gros, C. Herm, A. Stoll. A technical study of Ferdinand Hodler's painting technique – work in progress. In R. Vontobel, Ed.; *ICOM Committee for Conservation, Preprints of the 13<sup>th</sup> Triennial Meeting*, Rio de Janeiro, 22-27 September 2002. James & James: London, **2002**, 1:388-393.
- [21] J. van der Weerd, M. Geldof, L. Struik van der Loeff, R.M.A. Heeren, J.J. Boon. Zinc soap aggregate formation in 'Falling leaves (Les Alysamps)' by Vincent van Gogh. *Z. Kunsttechnol. Konserv.* **2003**, *17*, 407-416.
- [22] M. Gunn, G. Chottard, E. Rivière, J.-J. Girerd, J.-C. Chottard. Chemical reactions between copper pigments and oleoresinous media. *Stud. Conserv.* **2002**, *47*, 12-23.
- [23] A. Burmester, J. Koller. Known and new corrosion products on bronzes: Their identification and assessment, particularly in relation to organic protective coatings. In J. Black, Ed.; *Recent advances in the conservation and analysis of artifacts, Jubilee Conservation Conference*, London, 6-10 July 1987. University of London: London, **1987**, 97-103.
- [24] M.-C. Corbeil, L. Robinet. X-ray Powder Diffraction data for selected metal soaps. *Powder Diffr.* **2002**, *17*, 52-60.
- [25] F. Zimmermann, E. Meux, N. Oget, J.-M. Lecuire, J.-L. Mieloszynski. Solubility of Ca, Cu, Ni, Pb, and Zn azelates in pure water at 20°C. *J. Chem. Eng. Data* **2005**, *50*, 1833-1836.

- [26] H.-O. Johansson, E. Feitosa, A. Pessoa Jr. Phase diagrams of the aqueous two-phase systems of poly(ethylene glycol)/sodium polyacrylate/salts. *Polymers* **2011**, *3*, 587-601.
- [27] A. Phenix. The swelling of artists' paints in organic solvents. Part 2, comparative swelling powers of selected organic solvents and solvent mixtures. *J. Am. Inst. Conserv.* **2002**, *41*, 61-90.
- [28] J. van der Weerd, A. van Loon, J.J. Boon. FTIR studies of the effects of pigments on the aging of oil. *Stud. Conserv.* **2005**, *50*, 3-22.
- [29] J.J. Boon, F. Hoogland, K. Keune. Chemical processes in aged oil paints affecting soap migration and aggregation. In *The AIC Paintings Specialty Group Postprints: Papers Presented at the 34<sup>th</sup> Annual Meeting of the American Institute for Conservation and Historic Works*, Providence, 16-19 June 2006. American Institute for Conservation: Washington, D.C., **2006**, 18-25.
- [30] A. Ammala, S. Bateman, K. Dean, E. Petinakis, P. Sangwan, S. Wong, Q. Yuan, L. Yu, C. Patrick, K.H. Leong. An overview of degradable and biodegradable polyolefins. *Prog. Polym. Sci.* **2011**, *36*, 1015-1049.
- [31] T.A. Ibadapo. Polymeric structure in some molten groups IIA and IIB metal dicarboxylates. *Macromolecules* **1989**, *22*, 1480-1484.
- [32] H.B. Abrahamson, H.C. Lukaski. Synthesis and characterization of iron stearate compounds. *J. Inorg. Biochem.* **1994**, *54*, 115-130.
- [33] L. Robinet, M.-C. Corbeil. The characterization of metal soaps. *Stud. Conserv.* **2003**, *48*, 23-40.
- [34] R.J. Meilunas, J.G. Bentsen, A. Steinberg. Analysis of aged paint binders by FTIR spectroscopy. *Stud. Conserv.* **1990**, *35*, 33-51.
- [35] D. Bikiaris, Sister Daniilia, S. Sotiropoulou, O. Katsimbiri, E. Pavlidou, A.P. Moutsatsou, Y. Chrissoulakis. Ochre-differentiation through micro-Raman and micro-FTIR spectroscopies: Application on wall paintings at Meteora and Mount Athos, Greece. *Spectrochim. Acta A* **1999**, *56*, 3-18.
- [36] C.G. Juliá, C.P. Bonafé. The use of natural earths in picture: study and differentiation by thermal analysis. *Thermochim. Acta* **2004**, *413*, 185-192.
- [37] C. Genestar, C. Pons. Earth pigments in painting: characterisation and differentiation by means of FTIR spectroscopy and SEM-EDS microanalysis. *Anal. Bioanal. Chem.* **2005**, *382*, 269-274.
- [38] A. Phenix. Thermal mechanical transitions in artists' oil paints and selected conservation materials: a study by Dynamic Mechanical Analysis (DMA). In *The AIC Painting Specialty Group Postprints: Papers Presented at the 37<sup>th</sup> Annual Meeting of the American Institute for Conservation and Historic Works*, Los Angeles, 21-22 May 2009. American Institute for Conservation: Washington, D.C., **2009**, 72-89.
- [39] G. Rotter, H. Ishida. Dynamic Mechanical Analysis of the glass transition: Curve resolving applied to polymers. *Macromolecules* **1992**, *25*, 2170-2176.
- [40] T.J.R. Cyr, W.R. Janzen, B.A. Dunell. Effect of thermal history and impurities on phase transitions in long-chain fatty acid systems. In R.S. Porter, J.S. Johnson, Eds.; *Ordered Fluids and Liquid Crystals*. American Chemical Society: Washington, D.C., **1967**, 13-25.
- [41] M.S. Akanni, E.K. Okoh, H.D. Burrows, H.A. Ellis. The thermal behavior of divalent and higher valent metal soaps: A review. *Thermochim. Acta* **1992**, *208*, 1-41.

- [42] D.S. Kaplan. Structure-property relationships in copolymers to composites: molecular interpretation of the glass transition phenomenon. *J. Appl. Polym. Sci.* **1976**, *20*, 2615-2629.
- [43] H.E. Bair, P.C. Warren. Morphology of lightly plasticized PVC. *J. Macromol. Sci. B* **1981**, *20*, 381-402.
- [44] A. Eisenberg, J.D. Kim. *Introduction to Ionomers*. Wiley-Interscience: New York, **1998**.
- [45] E. Roduner. Size matters: why nanomaterials are different. *Chem. Soc. Rev.* **2006**, *35*, 583-592.
- [46] Z. Voras, K. deGhetaldi, B. Baade, J. Mass, T.P. Beebe, Jr. A closer look at historic paint materials using Time-of-Flight Secondary Ion Mass Spectrometry. Unpublished work, **2013**.
- [47] J.J. Boon, S.L. Peulvé, O.F. van den Brink, M.C. Duursma, D. Rainford. Molecular aspects of mobile and stationary phases in ageing tempera and oil paint films. In T. Bakkenist, R. Hoppenbrouwers, H. Dubois, Eds.; *Early Italian Paintings: Techniques and Analysis*, Maastricht, 9-10 October 1996. Limburg Conservation Institute: Maastricht, **1997**, 35-56.
- [48] M.R. Schilling, J. Mazurek, T.J.S. Learner. Studies of modern oil-based artists' paint media by Gas Chromatography/Mass Spectrometry. In T.J.S. Learner, P. Smithen, J.W. Krueger, M.R. Schilling, Eds.; *Modern Paints Uncovered: Proceedings from the Modern Paints Uncovered Symposium*, London, 16-19 May 2006. Getty Conservation Institute: Los Angeles, **2007**, 129-139.
- [49] C.S. Tumosa, D. Erhardt, M.F. Mecklenburg, X. Su. Linseed oil paint as ionomer: Synthesis and characterization. *Mater. Res. Soc. Symp. P.* **2005**, *852*, 003.2.
- [50] E.J. Goethals. Introductory remarks. In E.J. Goethals (ed.), *Telechelic Polymers: Synthesis and Applications*. CRC Press: Boca Raton, **1988**, 1.
- [51] A. Eisenberg, B. Hird, R.B. Moore. A new multiplet-cluster model for the morphology of random ionomers. *Macromolecules* **1990**, *23*, 4098-4107.
- [52] Y. Miwa, T. Kondo, S. Kutsumizu. Subnanoscopic mapping of glass transition temperature around ionic multiplets in sodium-neutralized poly(ethylene-*random*-methacrylic acid) ionomer. *Macromolecules* **2013**, *46*, 5232-5237.
- [53] R.W. Corkery. Metal organic framework (MOF) liquid crystals. 1D, 2D and 3D ionic coordination polymer structures in the thermotropic mesophases of metal soaps, including alkaline earth, transition metal and lanthanide soaps. *Curr. Opin. Colloid In.* **2008**, *13*, 288-302.
- [54] J. Sirois, D. Miller, E. Moffatt. Analysis of transparent white inclusions protruding from the surface of the painting *Portrait of Admiral Sir J. Ross*. Internal report, Canadian Conservation Institute, January 1992. Cited in P. Noble, J.J. Boon, J. Wadum. Dissolution, aggregation and protrusion. Lead soap formation in 17<sup>th</sup> century grounds and paint layers. *ArtMatters* **2002**, *1*, 46-61.
- [55] J. Sirois, S. Williams. Analysis of transparent white inclusions protruding from the surface of the painting *Portrait of Surgeon James Heron Conroy*. Internal report, Canadian Conservation Institute, January 1992. Cited in P. Noble, J.J. Boon, J. Wadum. Dissolution, aggregation and protrusion. Lead soap formation in 17<sup>th</sup> century grounds and paint layers. *ArtMatters* **2002**, *1*, 46-61.



# CHAPTER 2. IMPACT OF CROSSLINK DENSITY ON STRUCTURES IN CHEMISTRY-AGNOSTIC THERMOSETS

## 2.1. Introduction

Thermoset coatings and adhesives mandate high barrier properties which must stave off incessant environmental trespasses if the materials are to fulfill their purpose, as do many materials. Yet, foreign species progressively infiltrate coatings even in the absence of any extrinsic defects – scratches, pinholes, bubbles – and even before polymer degradation is effected by an aggressive environment. The mechanisms of ion and water transport through perfectly formed films have long presented interest to investigators working to develop more impervious barriers and to date are still poorly understood [1, 2]. This renders the question suitable for study by computer simulations, which complement real-world experiments through their power to access properties which cannot be characterized in the lab.

Thermosets are a diverse class of polymers. Two-component (2K) thermosets alone include epoxies, polyurethanes, polyesters, and phenolics as major constituents. Translating this variety of chemistries into classical mechanical models is not straightforward due to the empirical nature of the potential energy functions, also termed force fields, which are used to compute the net force acting on each particle at any point in time. The parameters of the most appropriate potential energy functions depend on the thermodynamic state of the simulated system, which is determined by variables such as temperature and composition, as well as on the properties studied by the simulation experiment (due to trade-offs in accuracy that arise when function parameters are optimized for a particular property) [3]. That is, there is no universal force field, only one most fitting for a particular problem. Therefore, instead of exploring a wide variety of chemistries, simulation literature focuses on model systems that are usually selected for their commercial significance or simplicity. For example, one popular system is  $n=0$  epoxy, diglycidyl ether of bisphenol A or F (DGEBA or DGEBF), crosslinked with diethyltoluene diamine (DETDA) [4-10]. Such studies hold the promise of one day being able to develop materials having target properties through primarily computational experimentation.

For the barrier properties of thermoset coatings and adhesives, arguably the most important controllable variable is the network topology, as opposed mainly to chemistry. Certainly, a polymer matrix is less receptive to the ingress of a particular foreign specie when it is less compatible chemically with that specie. However, when permeability is considered in general terms, without regard to individual aggressors, outcomes are determined by the characteristics of the available diffusion pathways – which, in thermoset coatings and adhesives, are thought to depend primarily on the crosslink density of the polymer. Since covalently bonded atoms have shorter average interparticle distances than do nonbonded atoms which interact via only the van der Waals forces, crosslinking increases the density of the system while reducing the mobility of the polymer chains. This is thought to constrict the diffusion pathways, rendering material transport through the polymer much more prohibitive.

A large library of simulation literature already exists on this subject, whose focus rests primarily with the thermo-mechanical properties of the networks. Some investigators had examined systems with intermediate extents of reaction [6, 7, 9-11] or systems that were off stoichiometry [8, 12]. Some had varied the functionality [13-17] or the chain length [9-10, 12, 17, 18] of one of the components. Here, the goal was to explore the effects of both functionality and molecular weight between crosslinks on parameters that likely affect the barrier properties of the thermoset. However, in realistic models, changing monomer functionality while fixing all other factors is not straightforward. Therefore, to focus on network topology while removed from the complexities of different chemistries, coarse-grained models were adopted by the present investigation, with some architectures based on those studied by Stevens and colleagues [13-16], which are also directly comparable to models studied by Duering, Kremer, and Grest [12].

In coarse-grained models such as ones used here, one bead represents not one atom but, rather, a group of atoms. In this manner, an entire DETDA molecule may be represented as one four-functional bead. Often, coarse-grained models are designed to describe specific chemical systems, – for example, by choosing which real atoms correspond to each coarse-grained bead, choosing the potential energy functions to model intra- and interchain interactions, and then optimizing free parameters of the potentials until the structure of the coarse-grained model closely reproduces the structure of the all-atom

model [3, 19]. The coarse-graining methods that have been developed have been motivated largely by the demands of multiscale modeling, wherein atomistic details are eventually reinserted into the coarse-grained structure, or where different levels of resolution (atomistic and coarse-grained) are present concurrently in the simulation.

However, when chemistry-agnostic properties and behaviors are the primary subject of interest, linking coarse-grained models to specific chemical systems is not always the most fitting option. The present study has called for a series of monomers that differed only in the number of their functionalities. However, despite best efforts, any such array of real monomers is bound to have other properties that differ slightly from one co-monomer to another – flexibility, molecular weight and size, chemical compatibility with the other co-monomer. These variations would be reflected in the coarse-grained models and they could complicate the interpretation of results. An alternative approach is to use simplified coarse-grained models that are fictional – i.e., not linked specific to real-world systems – with the goal of understanding the emergent properties self-consistently across the series [19, 20]. In such studies, only minimal features and interactions are accounted for by the models, and generic interaction potentials are used when those interactions are included at all, which has the effect of disregarding chemical details. This was the approach employed here.

This chapter is organized as follows. In the next section, the model is described, and end-linked network specimens are prepared by crosslinking a stoichiometric two-component mixture of monomers at a temperature well above  $T_g$  until a conversion of  $\sim 98\%$ . In Section 2.3, macroscopic thermo-mechanical properties are determined for each model. Glass transition temperatures and coefficients of volumetric thermal expansion are identified from stepwise cooling simulations. Then, elastic moduli and Poisson's ratios, both above  $T_g$  and below, are established from dynamical simulations through a stepwise application of tensile stress. Finally, in Section 2.4, network defects are described statistically through the prevalences of primary loops and dangling chains and are visualized using software that was developed as part of this work. All results are explained comprehensively by building close ties to experimental data for real-world polymers and to the predictions of classical theory of rubber elasticity.

## 2.2. Model Description

### 2.2.1. Monomers

Monomers that were used to create the two-component (2K) systems explored throughout this study are shown in Figure 2.1. One component, here called *crosslinker*, was varied across the series, while the other component, here called *chain extender*, was the same in each system. Crosslinkers were chosen such that differing crosslink densities of the resulting networks would arise from differences in both crosslinker functionality,  $f$ , and molecular weight between crosslinks,  $M_c$ . This is reflected in the nomenclature, with each system (or model) named according to the pattern of  $f$ - $M_c$ . For example, model 4-5 has a 4-functional crosslinker and 5 beads between the centers of crosslink junctions, as shown in Figure 2.2. A further discussion is provided in Section 2.4.1.

In models 4-3 and 6-3, one chain extender molecule was bonded to each crosslinker molecule prior to starting molecular dynamics, as shown in Figure 2.1. This was done for continuity from work that had been performed by Mark Stevens and colleagues on very similar models [13-16]. Pre-bonding was also a feature of very similar models that were studied by Duering, Kremer, and Grest, which had much larger  $M_c$ s [12]. Subsequent investigation established that such pre-bonding had no significant effects on the resulting network connectivity, as shown in Appendix G. Therefore, the effects of pre-bonding may be disregarded.

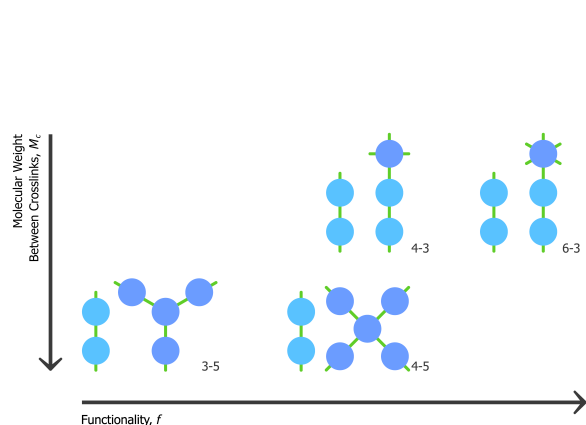


**Figure 2.1.** Monomers used to create the crosslinked networks that were investigated in this study, shown flattened to two dimensions for readability. Model names follow the format  $f$ - $M_c$  as labeled.

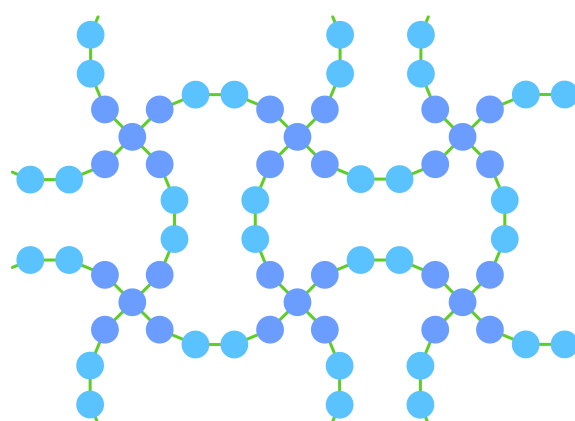


**Figure 2.2.** Schematic diagram of a two-dimensional equivalent of a defect-free network segment of model 4-5. The real, three-dimensional network is necessarily more complicated and is shown in a later section.

### 2.2.2. Particle Interactions

Molecular dynamics were performed using the Large-scale Atomic/Molecular Massively Parallel Simulator (LAMMPS) software package [21]. The Lennard-Jones system of reduced units was used, as traditionally done in coarse-grained simulations. The fundamental units were  $m$  for mass,  $\sigma$  for length, and  $\varepsilon$  for energy, and the units of time were derived as  $\tau \equiv \sqrt{m\sigma^2/\varepsilon}$ . The Boltzmann constant  $k_B$  had the value of unity. All particles (beads) were identical except for their bonding behaviors, each having the mass of  $1m$ , and each interacting through the same potentials regardless of bead type – i.e., regardless of whether it belonged to a crosslinker or a chain extender molecule. Such an idealized representation removes the possibility of phase separation among components, which is sometimes a problem in real systems.

Beads that were not bonded directly interacted via the shifted Lennard-Jones potential. This empirical potential has a long-range attractive tail that represents van der Waals interactions and a strongly repulsive core that represents Pauli repulsion due to overlapping electron orbitals (Figure 2.3). It has the following form:

$$U_{LJ}(r) = 4\varepsilon \left[ \left( \frac{\sigma}{r} \right)^{12} - \left( \frac{\sigma}{r} \right)^6 \right] \quad (2.1)$$

The distance between the centers of particles  $r$  has the units of  $\sigma$ , so the quantity in brackets is dimensionless and the overall expression has the units of energy. To improve simulation speed, this potential was truncated at  $r_c = 2.5 \sigma$ , when the value of the function would otherwise have

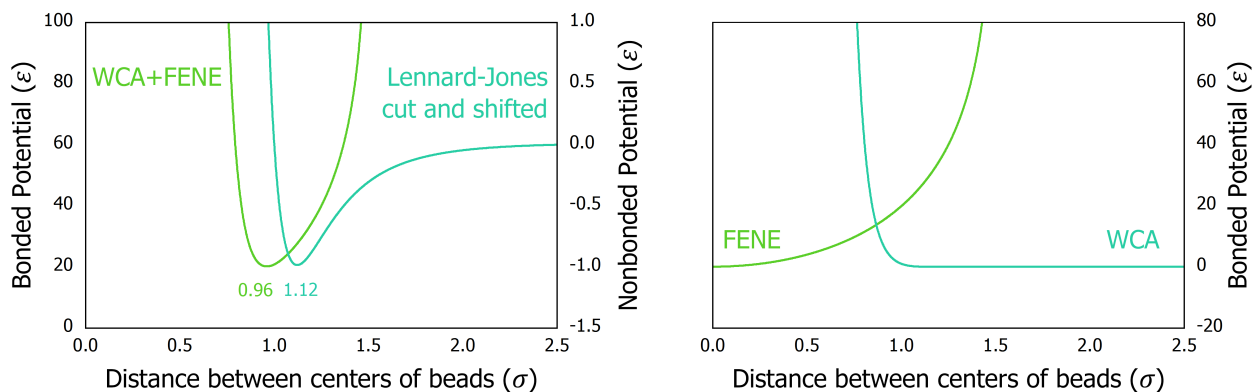


**Figure 2.3.** Potentials used to model interactions between particles (left) and separated components of the bonded potential (right).

been  $-0.016 \varepsilon$ , and the potential was shifted up by  $+0.016 \varepsilon$  to avoid a discontinuity:

$$U_{non-bonded}(r) = \begin{cases} U_{LJ}(r) - U_{LJ}(r_c), & r \leq r_c \\ 0, & r > r_c \end{cases} \quad (2.2)$$

Since the force vector acting on a particle is the negative gradient of the potential energy function, shifting the potential function in this manner avoids creating infinitely large forces at  $r \approx r_c$ .

Bonded particles interacted through the Weeks-Chandler-Anderson (WCA) potential to model nonbonded interactions, combined with the finite extensible nonlinear elastic (FENE) potential to model bonds:

$$U_{bonded}(r) = U_{WCA}(r) + U_{FENE}(r) \quad (2.3)$$

The WCA potential is the repulsive component of the Lennard-Jones potential, shifted up to eliminate the discontinuity [22]:

$$U_{WCA}(r) = \begin{cases} U_{LJ}(r) - U_{LJ}(r_{min}), & r < r_{min} \\ 0, & r \geq r_{min} \end{cases} \quad (2.4)$$

where  $r_{min} = 2^{1/6} \sigma \cong 1.12 \sigma$  and  $U_{LJ}(2^{1/6} \sigma) = -\varepsilon$  (Figure 2.3).

In contrast, the FENE potential is purely attractive and has the following form [23]:

$$U_{FENE}(r) = \begin{cases} -0.5Kr_0^2 \ln \left[ 1 - \left( \frac{r}{r_0} \right)^2 \right], & r < r_0 \\ \infty, & r \geq r_0 \end{cases} \quad (2.5)$$

where  $r_0 = 1.5 \sigma$  is the maximum extent of the bond. The strength of the interaction was scaled by the spring constant  $K = 30 \varepsilon/\sigma^2$  which is strong enough so that maximum extension of the bond is always less than  $1.2 \sigma$  at  $k_B T = 1 \varepsilon$ . This renders physically unrealistic chain crossing energetically infeasible in the model [23]. Figure 2.3 shows that bonded particles had an optimal bond length of  $0.96 \sigma$ , compared to an optimal interparticle separation of  $1.12 \sigma$  for non-bonded beads interacting through the Lennard-Jones potential.

No bond angle or dihedral interactions were incorporated into the model, so the molecules acted as freely-jointed chains. This would be an unrealistic assumption for an atomistic model, but in a coarse-grained model, that is not necessarily the case. Conformations of any polymer strand may be described by a freely-jointed chain that is composed of Kuhn nodes, which are stiff segments whose characteristic

size depends on the polymer chemistry, concentration, temperature, pressure, and other factors. Many thermoplastics have Kuhn lengths on the order of 1 nm at the typical experimental conditions [24]. In the present models, the size of a coarse-grained bead may be estimated by mapping one of the 2K systems on to a real system, for example an  $n=0$  DGEBA epoxy crosslinked with a ring-based diamine such as DETDA (Appendix F). The diameter obtained from this mapping is also on the order of 1 nm, so the current freely-jointed model is consistent with some possible polymer chemistries. However, as a brief caution, many thermosets have Kuhn lengths that are longer than 1 nm due to stiff aromatic groups that are often present as part of the backbone. If the present models were intended to reflect any specific thermoset chemistries, then angle and dihedral interactions would also have been required. But, since the goal here was to describe trends while remaining chemistry-agnostic, the simplicity of the freely-jointed model was preferred instead.

### 2.2.3. Simulation Procedure

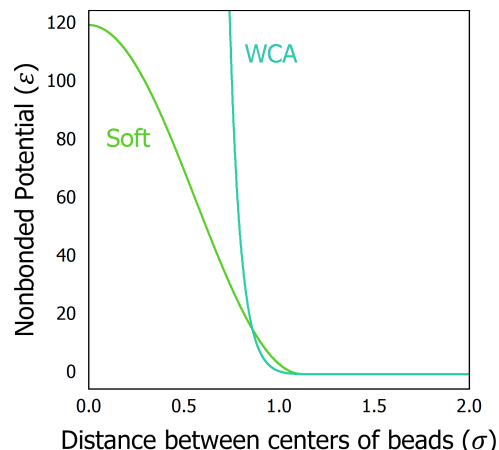
#### 2.2.3.1. Starting Configuration

Stoichiometric amounts of crosslinker and chain extender molecules were used such that the total system size was  $\sim 11,400$  beads, depending on the model (Table 2.1). Periodic boundary conditions (PBCs) were used to avoid boundary layer effects, so the simulated system represented a physical region in the bulk of the material, away from any interfaces. The use of PBCs is equivalent to creating a tiling system, analogous to a unit cell of a perfect crystal, wherein the simulation cell repeats infinitely in three dimensions. As a consequence, atoms exiting the simulation region through one bounding face reenter it

**Table 2.1.** Monomer amounts used to simulate each network model.

Model	Number of Molecules		Number of Beads
	Crosslinker	Chain Extender	
3-5	1,632	2,448	11,424
4-5	1,270	2,540	11,430
4-3	2,285	4,570	11,425
6-3	1,632	4,896	11,424

► **Figure 2.4.** Soft nonbonded potential used during the push-off run at the start of the simulation procedure, as compared to the WCA potential.



through the opposite face with unchanged velocity. And, atoms positioned near one boundary interact with atoms near the opposite boundary, - here, through the Lennard-Jones or the FENE potential, depending on whether or not they are bonded. Although PBCs succeed in overcoming surface effects, a small periodic system remains different from a macroscopic system because periodicity inhibits fluctuations in properties that would otherwise develop over distances larger than the cell size.

Size dependence of coarse-grained systems had been previously studied as part of adhesion work conducted at Sandia National Laboratories [14]. No qualitative effects were found on either tensile or shear properties for systems between 14,000 and 170,000 beads in size. Since models in the present study follow closely ones designed as part of that work, the system size of  $\sim 11,400$  particles was considered sufficient for exploring the qualitative trends across the series.

A cubic simulation cell was set up with a side length of  $\sim 24.3 \sigma$ , depending on the number of beads in the system, in order to obtain a final particle density of  $0.8 \sigma^{-3}$  at which Lennard-Jones systems are liquid. Monomers were inserted into the cell one by one, each at a coordinate chosen at random, and each oriented in a direction chosen randomly, in order to reduce the time that would be required to equilibrate the system. In this manner, 5 independent configurations were generated for each model for a total of 20 samples. During this stage, beads were allowed to overlap one another slightly so that the initial configuration could be generated in a timely manner.

Overlap was then removed by performing a short push-off run for  $10 \tau$  with a time step of  $0.001 \tau$ . During this run only, nonbonded beads interacted via a soft cosine potential instead of the Lennard-Jones potential:

$$U_{soft}(r) = \begin{cases} A \left[ 1 + \cos\left(\frac{\pi r}{r_c}\right) \right], & r < r_c \\ 0, & r \geq r_c \end{cases} \quad (2.6)$$

A cutoff distance  $r_c = 2^{1/6} \sigma$  and an amplitude  $A = 60 \varepsilon$  were used. This potential was chosen because it is far less repulsive at small interparticle distances compared to the Lennard-Jones potential (Figure 2.4). Beads were set in motion by assigning random velocities, and temperature was ramped over the run



from  $0.1 \varepsilon/k_B$  to  $1.0 \varepsilon/k_B$  by rescaling velocities of the beads. This process was performed at a constant volume. Time stepping, thermostating, and barostating in MD are explained briefly in Appendix E.

Next, the cosine potential was replaced with the Lennard-Jones potential and the system was equilibrated further to remove artifacts of the initial state. Equilibration was conducted for  $2,000 \tau$  at NVT followed by  $250 \tau$  at NPT. A time step of  $0.005 \tau$  was used here and throughout the rest of the simulations. In the NVT ensemble, the dimensions of the simulation cell are constrained, while in the NPT ensemble, the external pressure is constrained instead, so that cell dimensions expand and contract to match the setpoint pressure. The NPT stage was conducted at an external stress of  $0 \varepsilon/\sigma^3$  which, when periodic boundary conditions are used, enables the simulation cell to dissipate any internal stress. In this study, the NVT ensemble was implemented using the Langevin thermostat [25, 26], and the NPT ensemble, using the Nosé-Hoover chains thermostat and barostat [27, 28].

#### 2.2.3.2. Network Formation

The polymer network was formed dynamically at the same thermodynamic conditions as the previous stage. Every  $10 \tau$ , the simulation identified potential bonding partners as those crosslinker beads and chain extender beads that had available functionalities (as shown in Figure 2.1) and that were no farther apart than  $1.3 \sigma$ . Since each bead could thus have several potential bonding partners, in order for each bead to form no more than one bond at a time, bonding partners were narrowed down as follows: for each crosslinker bead, the nearest potential bonding partner was identified, and if that crosslinker bead was conversely that chain extender bead's nearest potential bonding partner, then that pair of beads could bond. A bond between each such pair of beads was created with a probability of 10%. The low probability allowed the network to form fairly slowly, although still much faster than in real-life systems.

In order to obtain conversions of  $\sim 98\%$  (Table 2.2), this procedure was conducted for a period of  $10,000 \tau$  for systems with  $M_c=5$  and for  $15,000 \tau$  for systems with  $M_c=3$  (because more bonds had to be created in the systems having higher final crosslink densities even despite the pre-bonding). The crosslinking reaction itself is discussed in some detail in Appendix G. The sol fraction was low for all

systems (Table 2.2), although it was higher for models with smaller  $M_c$ s due to their greater tendency to loop formation, which is discussed in Section 2.4.3. A snapshot of the simulation cell of one of the systems is shown in Figure 2.5. Alternative network representations are furnished in Section 2.4.3.

The simulation cell was allowed to relax (expand and contract) during the crosslinking reaction. Afterward, the systems were equilibrated at the same conditions for another  $500 \tau$ . Configurations saved at the end of this equilibration period were used for later analyses. The average density for each model is shown in Figure 2.6, with error bars indicating the lowest and the highest sample density for each set. Variation in sample densities was very low, which suggests that the systems were well-equilibrated at this stage. System density increased with crosslink density, as expected.

### 2.2.3.3. Cooling

The systems were next cooled to  $T=0.3 \varepsilon/k_B$  in three stages. First, the temperature was quenched to the new setpoint by rescaling the velocities of the beads throughout a short period of  $5 \tau$ , keeping the dimensions of the simulation cell fixed. Next, the system was equilibrated at NVT over  $2,000 \tau$ . Finally, the system was equilibrated at NPT, also over  $2,000 \tau$ . However, later, it was found that systems at the end of this period were not yet sufficiently relaxed for reliable characterization, as detailed in Section 2.3.2.2, so equilibration was continued for another  $1,000,000 \tau$ . Configurations saved at the end of this period were used for elastic characterization.

Final system densities increased very weakly with crosslink density (Figure 2.6). They were influenced far more by  $M_c$  than they were by crosslinker functionality. This may seem surprising at first, as bulk density is expected to increase with crosslink density by thermodynamics, whether such increases are effected through  $f$  or through  $M_c$  – because covalently bonded particles have shorter equilibrium interparticle spacings than do nonbonded beads, and because the number of bonds per particle increases

**Table 2.2.** Extents of the crosslinking reactions.

Model	Extent of Reaction (%)	Sol Fraction (%)
3-5	$97.8 \pm 0.1$	$0.86 \pm 0.20$
4-5	$97.7 \pm 0.2$	$0.29 \pm 0.17$
4-3	$98.6 \pm 0.1$	$1.31 \pm 0.28$
6-3	$97.9 \pm 0.1$	$0.45 \pm 0.10$

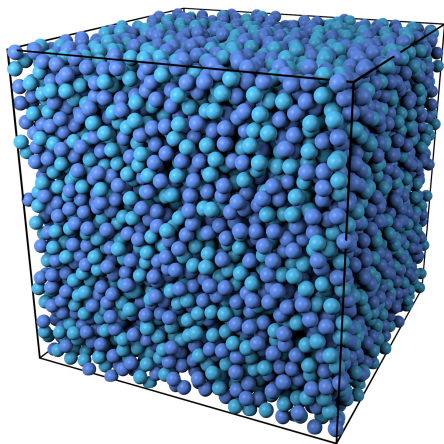


**Figure 2.5.** Snapshot of one of the samples of model 4-5 at  $T=1.0 \epsilon/k_B$  following crosslinking and equilibration. Colors distinguish between crosslinkers and chain extenders using the same convention as in Figure 2.1. Beads are shown using a space-filling representation with a diameter of  $1.0 \sigma$ .

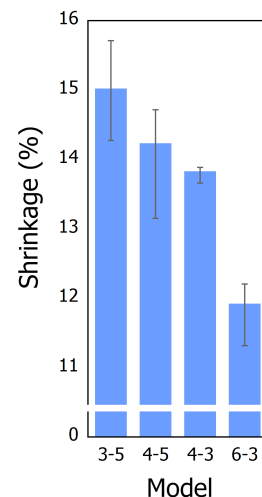
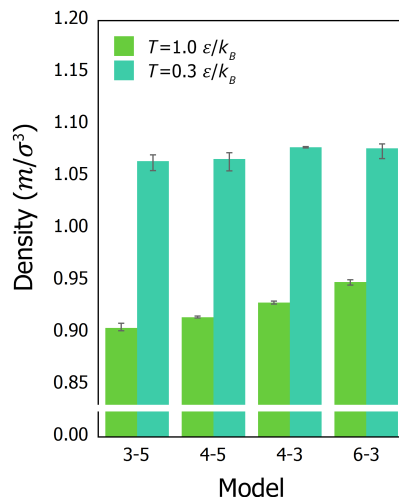


**Figure 2.6.** System densities at hot and cold temperatures used throughout the study (left) and the the extent of shrinkage upon cooling (right).

with crosslink density. However, these factors are in strong competition with the kinetic barriers to volume relaxation, so much so that sometimes, increasing crosslink density has the effect of lowering the bulk density [29]. In the present case, since bulk density increased weakly with crosslink density, the kinetic restrictions were not that severe. However, it is clear that volume relaxation was inhibited far more when it required cooperative motion amongst crosslink sites (as may be concluded by considering the trends in  $f$ ) rather than cooperative rearrangements of the intervening chains (seen by comparing models 4-3 and 4-5). This is well within expectations, since the rearrangement of crosslink junctions requires cooperative motion over far larger lengths.

Shrinkage was calculated as  $\frac{V_{1.0} - V_{0.3}}{V_{1.0}}$ , where  $V_T$  was the specific volume at the subscripted temperature. The results are shown in Figure 2.6. Shrinkage decreased as crosslink density increased because systems with high crosslink densities had higher bulk densities at high temperature, so they were not able to shrink as much upon cooling.

## 2.3. Macroscopic Characteristics

### 2.3.1. Volumetric Properties

Glass transition temperature was determined from the discontinuity in the coefficient of volumetric thermal expansion,

$$\alpha_v \equiv \frac{1}{V_0} \left( \frac{\partial V}{\partial T} \right)_P \quad (2.7)$$

Figure 2.7 shows the experimental procedure graphically for one of the samples of model 6-3. This model had the most nonuniform data for several reasons. First, it shrunk the least on cooling, as indicated in Figure 2.6, which resulted in a lower signal-to-noise ratio. Second, since it had the highest crosslink density of the series, it had a smaller fraction of material that was capable of changing its configuration and experiencing a glass transition. Third, its  $T_g$  was in the closest proximity to  $0.5 \varepsilon/k_B$ , which was one of the temperature steps used as input for the experiment. Nonetheless, the determination of  $T_g$  was unambiguous, and error bars (1 standard deviation) in the plot of  $V$  vs.  $T$  are not shown because they are approximately the same size as the square symbols.

In order to create such plots, simulations were performed at NPT, at an external stress of  $0 \varepsilon/\sigma^3$ . Temperature was lowered stepwise from  $1.0 \varepsilon/k_B$  to  $0.1 \varepsilon/k_B$ , at a rate of  $0.1 \varepsilon/k_B$  per step of  $2,000 \tau$ .

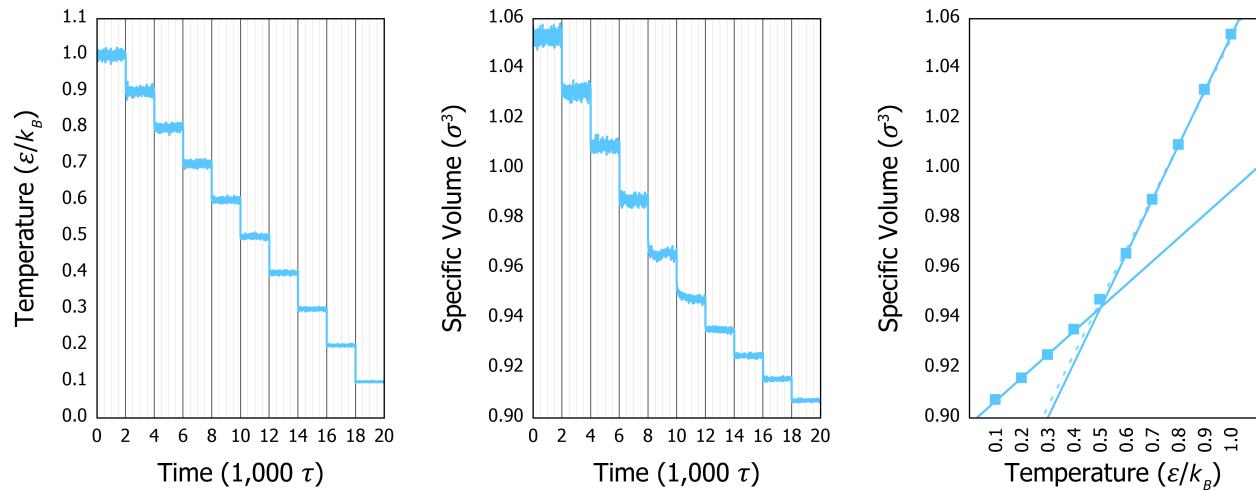


**Figure 2.7.** Calculation of the glass transition temperature for one of the samples of model 6-3. **Left:** Applied temperature. **Center:** Resulting specific volume. **Right:** Specific volume as a function of temperature. The dotted line is fit to points at temperatures 0.5-1.0  $\varepsilon/k_B$ . The dotted line is shown for comparison only.  $T_g$  was determined as temperature at the intersection of the solid lines.

Datapoints (temperature and cell dimensions) were recorded every  $5 \tau$ . Datapoints collected during the last  $500 \tau$  of each step were averaged together in order to create the  $V$  vs.  $T$  plots such as one in Figure 2.7. In other words, the first  $1,500 \tau$  of each step were treated as an equilibration period. As raw data in Figure 2.7 shows, this time period was sufficient to equilibrate the samples for all steps except for the one conducted at a temperature of  $0.5 \varepsilon/k_B$  because that temperature was very close to the  $T_g$ s of the samples. For this reason, this point was not included in the following linear fitting procedure.

Linear fits were performed using the method of York *et. al.* [30] and assuming no correlation between x and y errors. The  $T_g$  for each sample was determined as the intersection of these lines. The  $T_g$  for each model was then taken as the average of the five samples. The results are shown in Table 2.3.  $T_g$ s found in this manner increased with crosslink density, consistent with the expectations.

An alternate method of calculating the  $T_g$  was also performed. Data for each temperature step were averaged together, as above, but across all five samples of each model rather than for one sample at a time. Linear fitting was performed on these pooled datapoints as before. This method is equally valid physically because all simulated samples may be conceptualized as located at different coordinates within the same macroscopic sample. The difference in  $T_g$ s calculated with this alternate method was below the significance level of Table 2.3 which indicates that the results were not sensitive to the arbitrary choice of method.

Coefficients of volumetric thermal expansion were calculated using the specific volume at  $T_g$  as the reference volume  $V_0$  (Equation 2.7). Since crosslinks decrease the mobility of the polymer chains,  $\alpha_v$  decreased as crosslink density increased, and was higher in the rubbery state than the glassy state,

**Table 2.3.** Glass transition temperatures, specific volumes at  $T_g$  ( $V_0$ ), and coefficients of volumetric thermal expansion ( $\alpha_v$ ).

Model	$T_g (\varepsilon/k_B)$	$V_0 (\sigma^3)$	$\alpha_v (k_B/\varepsilon)$	
			Below $T_g$	Above $T_g$
3-5	0.448	0.952	0.114	0.286
4-5	0.452	0.950	0.111	0.273
4-3	0.465	0.945	0.105	0.258
6-3	0.502	0.944	0.098	0.231

consistent with the physical expectations. While these trends for fully-crosslinked systems have previously been observed through molecular dynamics by others [9, 18], to this author’s knowledge, this is the first such report in which the size of the simulation cell is not a confounding variable.

### 2.3.2. Elastic Properties

#### 2.3.2.1. Simulation Procedure Above $T_g$

Molecular dynamics simulations of tensile testing were conducted to determine the elastic modulus and the Poisson’s ratio of each model. As before, a Nosé-Hoover thermostat and barostat was used at a temperature of  $1.0 \epsilon/k_B$ . The procedure is shown graphically in Figures 2.7 and 2.8, which show modulus determinations, and in Figure 2.10, which shows how the Poisson’s ratio was calculated. By convention, negative pressure was tensile.

Samples were stretched in the x direction while allowed to relax (contract) in the y and z directions. Relaxation was enabled by maintaining the setpoint y and z components of the stress tensor,  $P_{yy}$  and  $P_{zz}$ , at  $0 \epsilon/\sigma^3$ . Similarly, stretching was effected by increasing the setpoint magnitude of the x component of the stress tensor,  $P_{xx}$ , from  $0 \epsilon/\sigma^3$  to a value that produced a  $\sim 10\%$  strain. This value was found for each model by trial and error. Stretching was performed in six steps, with a target step change of  $\sim 2\%$  strain per increment. The duration of each step was  $50,000 \tau$ , except for model 3-5, in which

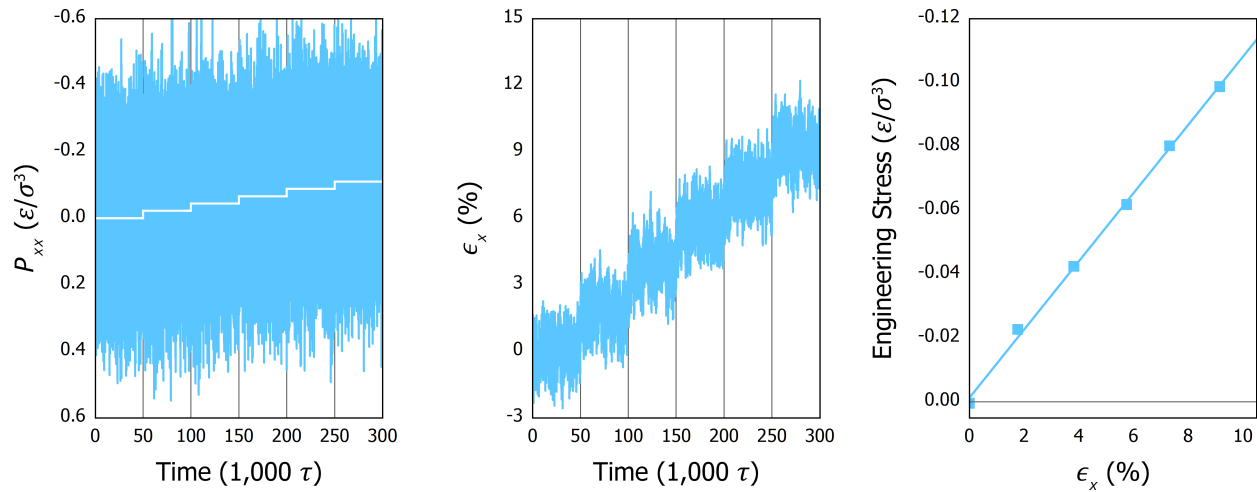


**Figure 2.8.** Determination of the elastic modulus above  $T_g$  for one of the samples of model 6-3. **Left:** Applied stress. Setpoint stress is shown in white. **Center:** Resulting strain. **Right:** Modulus calculation from the stress-strain plot.

case, a step length of 125,000  $\tau$  was used. This longer duration was chosen because model 3-5 had the lowest crosslink density of all models – which translates to the lowest modulus, which, in turn, necessitates the computational ability to distinguish smaller changes in  $P_{xx}$  at a given strain. In other words, greater sensitivity is required to accurately characterize lower values of modulus. This difficulty may be appreciated by comparing Figures 2.8 and 2.9. Also appreciated then is the high level of noise in  $P$ , which is indigenous to computer simulations as a consequence of the very small sample sizes when compared to macroscopic experiments. However, this and many other effects of small sample sizes may be offset by running the simulation over a longer time period and averaging the results. The longer stage duration used here, 125,000  $\tau$ , was considered sufficient because it resulted in a linear modulus plot, as per Figure 2.9. Finally, true stress  $P_{xx}$  was converted to engineering stress using the average cross-sectional area of the simulation cell during the first increment as the initial cross-sectional area.

Throughout the simulations, instantaneous properties (temperature, components of the pressure tensor, various energies, and cell dimensions) were recorded every 5  $\tau$ . For each datapoint, strain in the direction  $i$  (where  $i$  was  $x$ ,  $y$ , or  $z$ ) was calculated as

$$\epsilon_i(t) \equiv \frac{\Delta L_i}{L_{i,0}} = \frac{L_i(t) - L_{i,0}}{L_{i,0}} \quad (2.7)$$

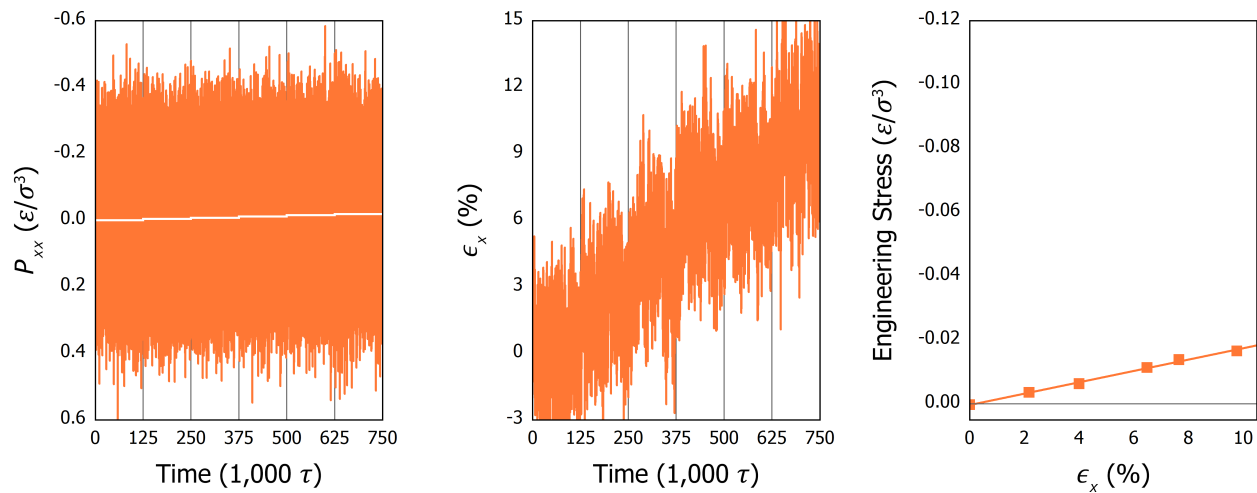


**Figure 2.9.** Determination of the elastic modulus above  $T_g$  for one of the samples of model 3-5. **Left:** Applied stress. Setpoint stress is shown in white. **Center:** Resulting strain. **Right:** Modulus calculation from the stress-strain plot.

where  $L_i(t)$  was the length of the simulation cell in the direction  $i$  at time  $t$ , and  $L_{i,0}$  was the average value of  $L_i(t)$  during the first stage of the experiment, when setpoint  $P_{xx}$  was zero. Datapoints were averaged over each stage to produce stress-strain plots such as ones in Figures 2.8 and 2.9. Error bars are not shown in these plots since, as raw data demonstrates, errors were very large, which is typical for elastic testing in molecular dynamics. Data were linear across the studied range.

Linear fits were performed using the method of York *et. al.* and assuming no correlation between  $x$  and  $y$  errors. The elastic modulus  $E$  was then defined as the slope of the line of best fit. Two methods of averaging were used, as discussed in the previous section on  $T_g$ , but same as with  $T_g$ , the difference owing to the choice of the averaging method was not significant.

Poisson's ratio  $\nu$  was calculated as the average of  $\nu_y$  and  $\nu_z$ :

$$\nu(t) \equiv \frac{\nu_y(t) + \nu_z(t)}{2} = \frac{1}{2} \left[ \frac{-\Delta\epsilon_y}{\Delta\epsilon_x} + \frac{-\Delta\epsilon_z}{\Delta\epsilon} \right] = -\frac{\Delta\epsilon_y + \Delta\epsilon_z}{2\Delta\epsilon_x} \quad (2.8)$$

For a macroscopic sample,  $\nu_y$  and  $\nu_z$  are equivalent. However, for small samples such as ones used here, these two values at a given time  $t$  are distinct. Averaging the two values in this manner has the effect of reducing the magnitude of the errors, as shown graphically in Figure 2.10. Error bars in model-wide  $\nu$  show the smallest and the largest value of sample  $\nu$  to indicate the variability of results across each model. Noise is best assessed by considering the raw data.

Values of Poisson's ratio were consistent with the physical expectations. However, values weakly decreased as the strain increased. Although the precise reason for this was not clear, it appears to be an artifact of the averaging together of  $\nu_y$  and  $\nu_z$  – because the plots of  $\nu_y(t)$  and  $\nu_z(t)$  are fairly symmetrical while a plot of  $\nu(t)$  is not, and because no comparable trends appear in the bar graphs of  $\nu_y(\text{target } \epsilon_x)$  or  $\nu_z(\text{target } \epsilon_x)$  (data not shown). However, since this trend was very weak, and since averaging  $\nu_y$  and  $\nu_z$  together was effective in counteracting a large amount of noise, the benefit of noise reduction outweighed the problem of the slight inaccuracy as a consequence of this possible artifact, at least for the present qualitative purposes.



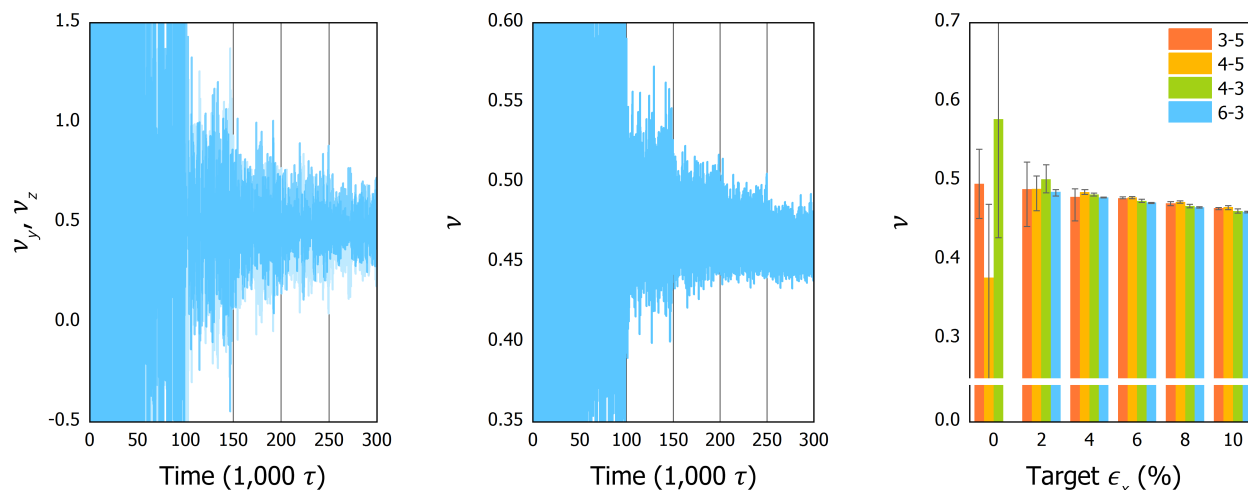


**Figure 2.10.** Determination of the Poisson's ratio above  $T_g$ . **Left and Center:** Instantaneous values of Poisson's ratio before and after averaging together the y and z dimensions, respectively, for one of the samples of model 6-3. Notice the difference in scales. Traces of  $\nu_y$  and  $\nu_z$  are translucent to show overlap. **Right:** Poisson's ratio for the four models as a function of (target) strain.

To focus on the differences among the different models, only one value of Poisson's ratio above  $T_g$  is reported in Section 2.3.2.3 for each model. This value is the model-wide average  $\nu$  for the stage conducted at the maximum strain,  $\sim 10\%$ . This stage was chosen because the level of noise decreased as the strain increased, which could be explained by the definition of Poisson's ratio: since the calculation of  $\nu$  involves division by  $\epsilon_x$ , at low strains this calculation approaches a division by zero. For this reason, some of the model-wide  $\nu$ 's that were obtained at low strains (0-4%) were statistically unreliable, as can be judged by considering data in Figure 2.10, right.

### 2.3.2.2. Simulation Procedure Below $T_g$

Simulations of tensile testing conducted below  $T_g$  were, in most respects, identical to the ones conducted above  $T_g$ , except that a temperature of  $0.3 \epsilon/k_B$  was used. One welcome difference was the lower level of noise, which is expected of glassy materials, that enabled using the same stage duration of 50,000  $\tau$  for all models. In other words, a longer stage length of 125,000  $\tau$  was not required for model 3-5, as it was at  $T=1.0 \epsilon/k_B$ . One other difference was the use of a smaller maximum strain. Finally, a pre-equilibration period was required before tensile testing could begin, as explained below.

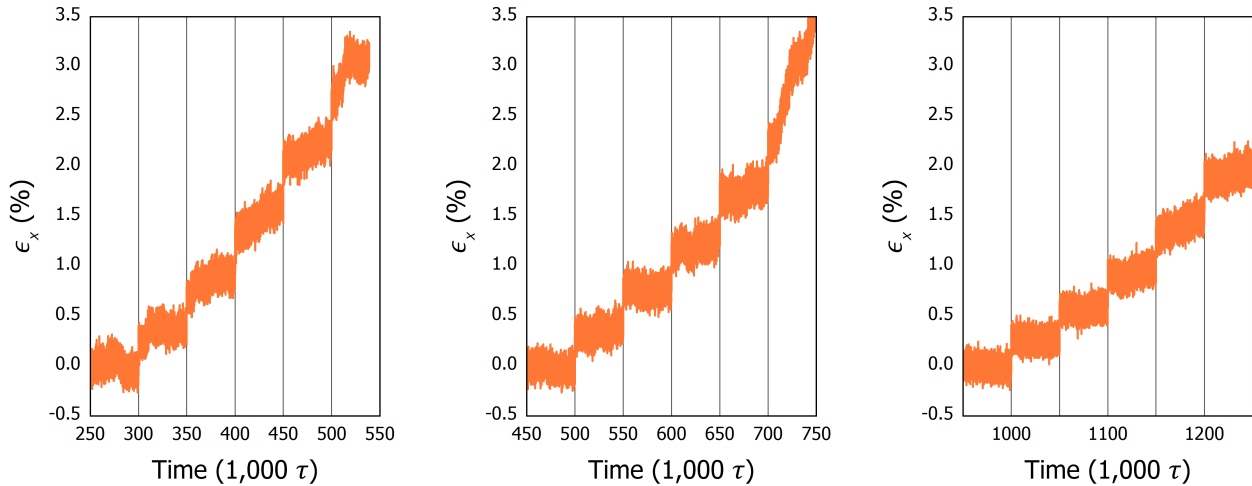


**Figure 2.11.** Influence of the duration of the pre-equilibration period on the results of tensile testing conducted below  $T_g$  for one of the samples of model 3-5. The pre-equilibration period increases from left to right from 300,000  $\tau$ , to 500,000  $\tau$ , to 1,000,000  $\tau$ . The tensile testing routine was the same for each test.

At first, the tensile testing procedure was attempted on samples that, as detailed in Section 2.2.3.4, had been equilibrated at  $T=0.3 \text{ } \varepsilon/k_B$  and an external stress of  $0 \text{ } \varepsilon/\sigma^3$  for a duration of 2,000  $\tau$ . However, these samples yielded dramatically during the first increment of the test (Figure 2.11), when setpoint  $P_{xx}$  was still  $0 \text{ } \varepsilon/\sigma^3$ , so a much longer equilibration period was in order. A pre-equilibration period of 300,000  $\tau$  was attempted, which was extended to 500,000  $\tau$ , and then to 1,000,000  $\tau$ . The

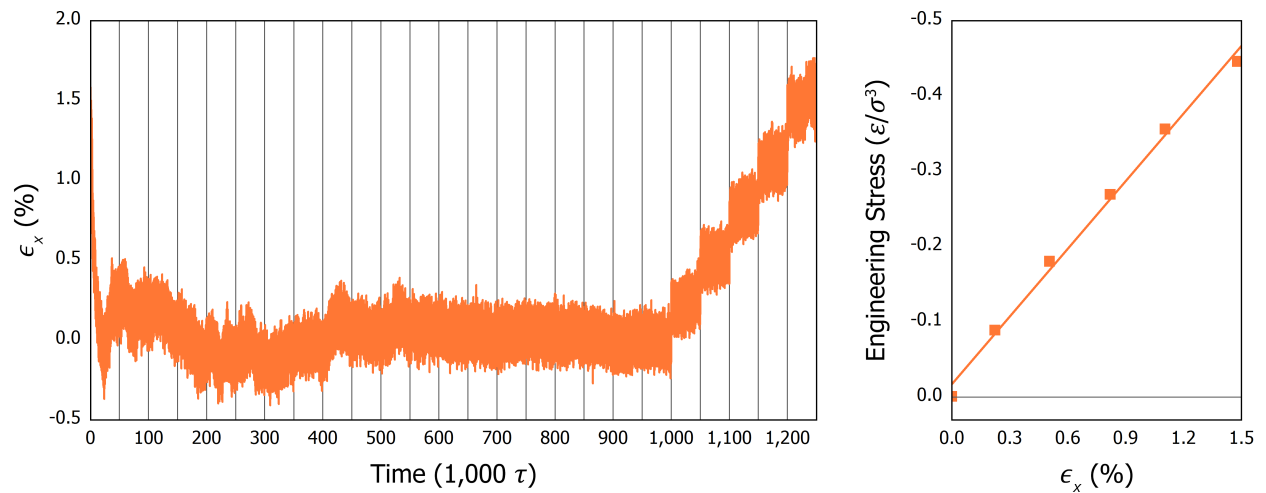


**Figure 2.12.** Determination of the elastic modulus below  $T_g$  for one of the samples of model 3-5. **Right:** Strain recorded during the pre-equilibration period, when the applied stress had been zero, and during the subsequent tensile test. **Left:** Modulus calculation from the stress-strain plot.

configurations at the end of the 1,000,000  $\tau$  pre-equilibration period were used for all subsequent testing.

The tensile tests are shown in Figure 2.11. The last 50,000  $\tau$  of the pre-equilibration period doubled as the first increment in the tensile testing experiment. Note that that the average x-strain during this first increment was zero by definition, per Equation 2.8. The sample of model 3-5 shown in Figures 2.11 and 2.12 provides the broadest representation of features that were exhibited by the various samples. In general, however, there was much diversity from sample to sample, as may be expected from non-equilibrium configurations.

While the shorter equilibration periods appeared sufficient for some of the 20 samples, it was only after the period of 1,000,000  $\tau$  that most samples exhibited no appreciable yielding at lower strains. Yet, some yielding still occurred at the higher strains used. During these initial tests, the target maximum strain was 2%, compared to a maximum strain of 10% that was used in the rubbery state. While a lower maximum strain was an important part of experimental design (because samples were expected to be more rigid in the glassy state), its value of 2% was chosen arbitrarily. Therefore, it was straightforward to reduce the target maximum strain to 1.5%, a value below which yielding was less pronounced.

Tests performed in this manner showed less appreciable yielding, which may be noted by comparing Figure 2.11 (right), conducted to 2% maximum strain, and Figure 2.12 (left), conducted to 1.5% maximum strain, everything else between the two tests being equal. Further, the stress-strain plots were sufficiently linear (Figure 2.12), so it was decided that additional pre-equilibration was not warranted since it would not qualitatively affect the results. Nonetheless, since some samples yielded somewhat during the testing, it should be noted that additional pre-equilibration would have had a slight quantitative influence on results, producing slightly higher calculated values of modulus.

Calculation of Poisson's ratio was straightforward, uncomplicated by the strain-dependence that had been observed above  $T_{g,r}$  as shown in Figure 2.13. This may be explained by the lower level of data noise below  $T_{g,r}$ , which is relevant because the artifact responsible for the strain-dependence of  $\nu$  above  $T_g$  appeared proportional to the level of noise. For consistency, results reported in the next section are

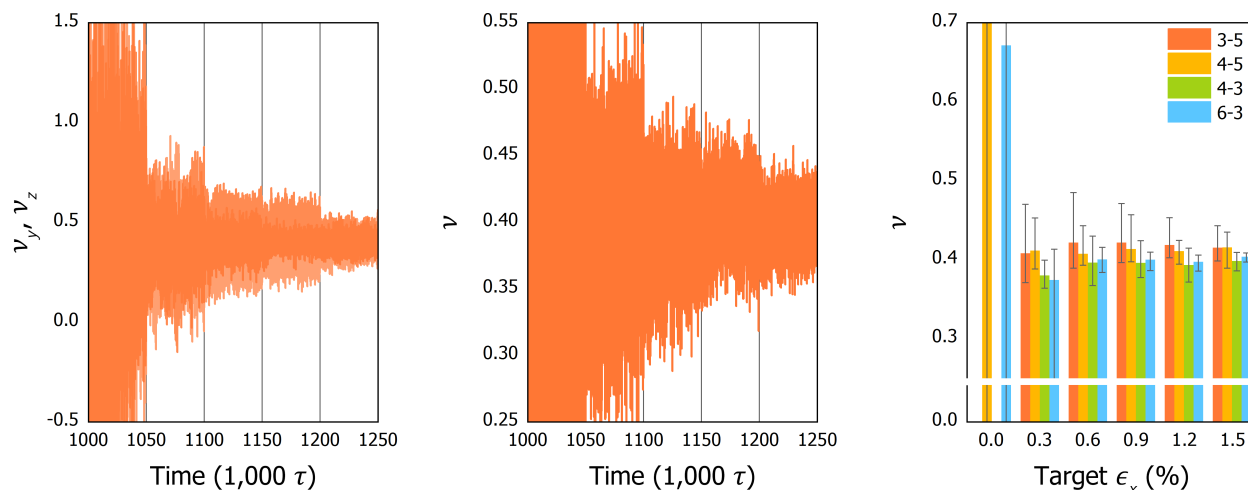


**Figure 2.13.** Determination of the Poisson's ratio below  $T_g$ . **Left and Center:** Instantaneous values of Poisson's ratio before and after averaging together the y and z dimensions, respectively, for one of the samples of model 3-5. Notice the difference in scales. Traces of  $\nu_y$  and  $\nu_z$  are translucent to show overlap. **Right:** Poisson's ratio for the four models as a function of (target) strain.

the mean values of Poisson's ratio for each model averaged over the stage that was conducted at the maximum strain,  $\sim 1.5\%$ .

### 2.3.2.3. Results and Discussion

Molecular dynamics simulations of tensile testing were conducted to determine the elastic modulus and the Poisson's ratio of each model in both the glassy and the rubbery temperature regions. A broader range of elastic behaviors had previously been examined at Sandia National Laboratories as part of investigations into the adhesive properties of thermosets, including shear and high-strain tensile phenomena [13-16]. In the present study, the motivating interests were in degradation and in permeability of the thermoset networks to foreign species, which do not entail large-scale deformations of material, so the focus was narrowed to such properties which are important at low strains.

**Table 2.4.** Elastically active network fractions and elastic moduli at  $T=1.0 \text{ } \epsilon/k_B$ . Modulus values from simulations are compared to the predictions of the rubber elasticity theory for defect-free networks using two limiting-case assumptions about the severity of the diffusional constraints that impinge on the crosslink junctions.

Model	Elastically Active Fraction (%)	$E (\epsilon/\sigma^3)$		
		Phantom Model	Affine Model	Simulation Result
3-5	81	0.13	0.26	0.17
4-5	87	0.22	0.44	0.31
4-3	80	0.32	0.64	0.51
6-3	73	0.43	0.86	1.02

The elastic modulus above  $T_g$  increased monotonically with crosslink density and was sensitive to both the crosslinker functionality  $f$  and the molecular weight between crosslinks  $M_c$  (Table 2.4). This trend was in qualitative agreement with the statistical mechanical theory of rubber elasticity [31]. To check quantitative agreement, calculations were performed for the two limiting-case scenarios elaborated by the theory. Very briefly, in a *phantom network*, crosslink junctions fluctuate around their mean positions in a Gaussian manner, whereas for an *affine network*, such diffusional fluctuations are completely suppressed. According to the Flory-Erman model [32, 33], the behavior of real thermoset networks lies between these extremes when the fluctuations of the crosslink sites are restricted somewhat by their *entanglements*, which are localized correlations between displacements of neighboring crosslink sites, and which may be due to bonded interactions as well as such nonbonded interactions that inhibit the local rearrangements of chains. This deviation from either of the ideal behaviors is reflected in the theory through a parameter that characterizes the severity of constraints, such that for the limiting values of this parameter, the generic equations reduce to the specific cases of a phantom or an affine network.

To calculate the elastic moduli for these two cases, a network search algorithm was developed following literature descriptions [34-36] and was used to determine the following parameters for each sample:

- the number of elastically active junctions,  $\mu_{ar}$ , where an *active junction* is a crosslink site that is connected by at least 3 paths to the gel;
- the number of elastically active chains,  $\nu_{ar}$ , where an *active chain* is a path that is composed of chain extender beads and inactive junctions and that is terminated by active junctions on both its ends; and
- the number of elastically active beads, which includes all beads that are located in either the active junctions or the active chains.

The fraction of elastically active beads,  $p_{ear}$ , spanned a large range across the series, with the highest value attained by model 4-5 (Table 2.4). Its value of 87% was lower than the 93-96% that had been obtained by Duering, Kremer, and Grest for their series of thermosets, which were also 4-functional

but which had much larger  $M_c$ s [12]. From these two datasets, it may be inferred that as  $M_c$  increases,  $p_{ea}$  increases quickly at first and eventually asymptotes at a value that is close to 1.

For models with higher crosslink densities, the value of  $p_{ea}$  showed a monotonic decrease. This trend may be explained by the same phenomena as the relationship between normalized effective functionality and crosslink density which is discussed in Section 2.4. However, while normalized effective functionality was higher for model 3-5 than for model 4-5,  $p_{ea}$  showed the inverse trend. Thus, although as shown in Section 2.4, junctions in model 3-5 had on average more connections to their first-neighbor junctions, many of these junctions were not elastically active (for example, because model 3-5 had a higher sol fraction), such that model 3-5 exhibited a lower rubbery modulus despite better local connectivity.

Next, the shear modulus for the phantom model was calculated using

$$G_{ph}(T) = \zeta \cdot \frac{k_B T}{V} \quad (2.9)$$

where the relationship  $\zeta = \nu_a - \mu_a + 1$  was used to calculate the cycle rank [34, 37]. Similarly, the shear modulus for the affine model was calculated using

$$G_{aff}(T) = \nu_{eff} \cdot \frac{k_B T}{V} \quad (2.10)$$

where the relationship  $\nu_{eff} = 2\zeta$  was used for the number of elastically *effective chains* [34, 37]. These equations emphasize that the modulus is always lower for phantom networks than for their affine analogues, which reflects the inference that in the phantom model, strain transforms only the mean positions of the crosslink sites, having no effect on fluctuations about these positions [M33]. Finally, elastic moduli were estimated from the respective shear moduli using  $E = 2G(1 + \nu)$ ,  $\nu$  being Poisson's ratio the values of which are presented later in this section.

The results of these calculations are shown in Table 2.4 alongside results from molecular dynamics. Except for model 6-3, obtained values were within the limits of the predictions: model 3-5, which had the lowest crosslink density in the series, was closer to the phantom case, model 4-5 was intermediate between phantom and affine cases, and model 4-3 was closer to the affine prediction. This

is consistent with the theory of rubber elasticity since increases in the crosslink density may be expected to increase the severity of entanglements of the junctions, thereby reducing the diffusional mobility of the crosslink sites. This concord is somewhat surprising because the Flory-Erman model assumes that Gaussian statistics apply to the polymer chains that intervene between crosslink junctions, but those chains consist of only 3 or 5 beads in the current networks.

The modulus of model 6-3, which had the highest crosslink density of the series, was extremely high: it was two times greater than the modulus of the model having the second-highest crosslink density, and it slightly exceeded the prediction of the affine model. Previous simulations of similar coarse-grained materials had shown that moduli in excess of the affine prediction are in part due to the effect of excluded volume, which is not accounted for by the Flory-Erman model, since excluded volume effectively constrains the motions of crosslink junctions [12]. The present discrepancy may then be interpreted to reflect the importance of excluded volume to the structure of network 6-3, which is reasonable considering that model 6-3 represents an extreme case wherein 6 functionalities are concentrated in a very small physical region.

Moving on, elastic moduli below  $T_g$  were similar across all the models (Table 2.5). To review, the tensile properties above  $T_g$  are controlled by the decrease in entropy upon extension, which occurs when randomly coiled polymer chains are stretched taut into less probable configurations. This is an intrachain phenomenon, and it is affected by crosslink density because crosslinking couples previously independent chains. However, when experimental temperature decreases, entropy has far less impact on material properties, as either a cause or a consequence of the sharp kinetic slowdown that characterizes the glass transition [38]. Instead, below  $T_g$ , intermolecular (e.g. Lennard-Jones) interactions control properties,

**Table 2.5.** Elastic moduli and Poisson’s ratios determined at  $T=1.0$  and  $T=0.3 \text{ } \epsilon/k_B$ .  $T_g$  values are repeated from Table 2.3 for convenience, and density values are repeated from Figure 2.6.

Model	$T_g (\epsilon/k_B)$	Above $T_g$			Below $T_g$		
		$\rho (m/\sigma^3)$	$E (\epsilon/\sigma^3)$	$\nu$	$\rho (m/\sigma^3)$	$E (\epsilon/\sigma^3)$	$\nu$
3-5	0.448	0.905	0.17	0.465	1.065	30.8	0.415
4-5	0.452	0.915	0.31	0.466	1.067	34.0	0.415
4-3	0.465	0.929	0.51	0.461	1.078	36.4	0.398
6-3	0.502	0.949	1.02	0.460	1.077	35.2	0.404

such that crosslinking affects the modulus mainly through its indirect effect on  $\rho$ , the bulk density [39]. For the present systems,  $\rho$  increased weakly with crosslink density, and the elastic modulus increased as well.

Interestingly, the density and the modulus of model 6-3 were slightly lower than those of model 4-3. This may happen when high kinetic barriers to mobility trap free volume within the material. The presence of trapped free volume may be inferred from the presence of internal strain, which in turn is may be illuminated by considering the average bond lengths. For models 3-5 through 4-3, the average bond lengths at  $T=0.3 \epsilon/k_B$  were within  $<0.01\%$  of their average, and there was no correlation between bond length and crosslink density, - which indicates that internal strain in these systems was negligible. However, the average bond length for model 6-3 was  $0.08\%$  greater than the average bond length of models 3-5 through 4-3, indicating a small degree of internal strain. Since results were similar at  $T=0.3 \epsilon/k_B$ , it is possible that this strain was introduced during crosslinking. (However, data analysis showed that it was not attributable to the large prevalence of loops.) This informs the interpretation of data, but it does not affect the validity of results because real-world crosslinking reactions often build up internal strain [6, 40].

Next, the low-temperature modulus values for models 4-3 and 6-3, which had been designed following the work of Stevens and colleagues, are in general agreement with their data [14, 15]. This agreement is qualitative because Stevens's work focused on high-strain behavior, so elastic moduli had not been reported – but they may be estimated from the published stress-strain plots. Then, moduli obtained by Stevens for similar system sizes appear to be slightly higher than the ones obtained in this work. This slight discrepancy may be explained by the slight difference in potential functions used to model bonded interactions here and in Stevens's work, since the force field used by Stevens had a shorter equilibrium bond length ( $\Delta r=0.03 \sigma$ ) and produced networks with higher densities. With this procedural difference in mind, the two sets of results come in accord.

Finally, Poisson's ratio was higher in the rubbery region than the glassy region, and it decreased weakly as the crosslink density increased (Table 2.5). These results are consistent with the physical literature on thermosets. In the glassy region, Poisson's ratio typically has values between  $\sim 0.35-0.42$ ,



depending on the polymer, which increases slowly as the temperature is increased [41, 42, 43, 44, 45]. Although one study of Poisson's ratios in the glassy region found no relationship between  $\nu$  and the crosslink density (XLD) in the range of XLDs studied [44], another study which examined a broader range of XLDs found that Poisson's ratio decreased from  $\nu=0.395$  to  $\nu=0.37$  as the crosslink density increased [42]. This was consistent with the modest range of Poisson's ratios,  $\Delta\nu=0.017$ , for the moderate range of crosslink densities considered in this study, as well as the direction of the trend. Further, it has long ago been suggested that crosslinking would depress the Poisson's ratio as a consequence of increasing the rigidity of the material [46]. This is consistent with the present simulation results. However, since Poisson's ratio for the highest-crosslinked system was only 0.40, whereas values as low as 0.35 have been reported in the literature, this suggests that the simulated materials are somewhat less rigid than some of their real-world counterparts. This flexibility is an expected consequence of using freely-jointed chains for the material model. The same conclusion was reached by the unit mapping study provided in Appendix F: the subsequent comparison of moduli and  $\alpha_s$ s showed that the simulated thermosets are flexible, yet within the range exhibited by real-world thermosets.

When the temperature is raised in the region surrounding the glass transition ( $T_g \pm \sim 20\text{K}$ ), Poisson's ratio rises sharply to an asymptotic value. That value is sometimes said to be 0.5 because that describes the ideal case of an incompressible solid [43, 44]. However, experimental reports of Poisson's ratio in highly-crosslinked thermosets such as ones studied here are sparse as a result of the high instrumental accuracy that is necessary for its measurement, – and the measurement of  $\nu$  in the rubbery region is more difficult yet [41, 44, 45]. To date, the only study that had thoroughly examined  $\nu$  above  $T_g$  in such systems found Poisson's ratios that were no higher than 0.46 at temperatures far above the glass transition, with an asymptote that seemed to be located much lower than at  $\nu=0.5$  [41, 45]. This is consistent with the current simulation results of  $\nu$  between 0.460-0.466 at temperatures that were even farther above  $T_g$ .

As a last word, it should be noted that Poisson's ratio decreased as density increased, which is inverse of the relationship typical for most materials [47]. To this author's knowledge, this exception for

thermosets has not previously been observed. One simulation study of DGEBA/DETDA systems did report that Poisson's ratio increased as the length of the DGEBA co-monomer ( $M_c$ ) increased [9]. However, in that study, density increased with  $M_c$ , contrary to expectations. The study authors attributed this and certain other outcomes to the finite size effect, which had been invoked because systems with different  $M_c$ s also differed significantly in their sizes. As a result, the authors advised against comparing properties of systems with different  $M_c$ s in that study – such that comparison with the present results cannot be made. In a later study, the same authors reported Poisson's ratios for series that that was constant in system size [10]. Yet, since system densities were not also reported, the relationship between Poisson's ratio and density was indeterminate.

### 2.3.3. Section Conclusion

The glass transition temperatures were in the range of 0.45-0.50  $\varepsilon/k_B$  and they increased with crosslink density. The elastic modulus below  $T_g$  increased weakly with crosslink density, which was attributed to the trend in bulk density – i.e.,  $\rho$  at  $T=0.3 \varepsilon/k_B$  also increased with XLD. The elastic modulus above  $T_g$  increased with crosslink density and was in qualitative agreement with predictions of the theory of rubber elasticity, which had been calculated for the present series by determining the cycle rank of each network using an algorithm that was developed as part of this work. This data was also consistent with simulation results that were obtained for similar molecular models by a different research group. Poisson's ratio had values between 0.40-0.47 which were significantly higher above  $T_g$  than below, and which decreased weakly as crosslink density increased. These values and trends were in agreement with literature data for real-world thermosets.

Values of Poisson's ratio gently suggested that the simulated materials were slightly less rigid than their physical counterparts. Although this inference was far from conclusive, any additional flexibility could be explained by the material model which represented the molecules as coarse-grained freely-jointed chains. However, despite flexibility, modulus values and bond lengths for the most densely crosslinked model in the series suggested that it experienced high barriers to mobility when compared to the other models.

Overall, the macroscopic properties of the series followed the expected trends with increases in crosslink density and were in quantitative agreement with literature results when such comparisons had been possible. These findings help to validate the model before proceeding to more novel experimentation.

## **2.4. Local Network Topologies**

### **2.4.1. Definitions of Terms**

Macroscopic connectivities of the networks were described in the previous section through the property of cycle rank,  $\zeta$ . Although cycle rank is often said to be the most important topological property of a network, it is not always the one that is the most relevant, since the set of features that warrants inquiry depends crucially on the bulk property that motivates the interest of the investigation. With protective coatings, both elastic and barrier properties must be considered. These two treatments are distinct: while elastic behavior involves cooperative movement of material over a macroscopic scale, diffusion is a local phenomenon. For example, sol fragments are said to contribute nothing to elastic properties: since they are not connected to the macroscopic network, they cannot provide a retractive force when the macroscopic sample is stretched. (For simplicity, current treatments of elasticity do not account for the scenario of sol fragments that are connected to the gel physically using loops [48].) However, sol fragments must contribute something to barrier properties: it would be implausible for a sol section to have the same permeability as an equivalent mass of uncrosslinked monomers. Therefore, this final section examines the most common short-range defects which affect both barrier and elastic properties – dangling chain ends and primary loops.

To start off, some intuitive terms must be defined to avoid ambiguity. The *crosslink site* or the *network junction* is any bead whose functionality is greater than 2. In this study, each crosslinker molecule had exactly one crosslink site. The familiar property of the molecular weight between crosslinks,  $M_c$ , may then be defined as the weight of material that resides between the centers of such crosslink junctions, which in this work is numerically equivalent to the number of beads (because the weight of each bead was simply  $1m$ ). For example, if one travels from junction A to junction B in Figure 2.14, or

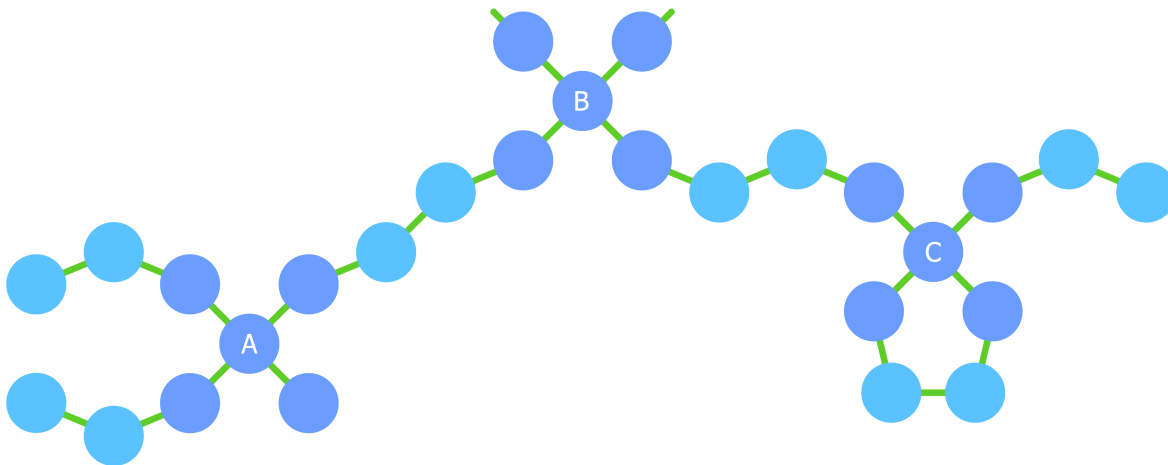


**Figure 2.14.** Schematic diagram of a portion of a network of model 4-5. Network junctions labeled A, B, and C are discussed in the text.

from junction B to junction C, one will traverse  $\frac{1}{2}+1+2+1+\frac{1}{2}=5$  beads, such that  $M_c=5m$ . To improve readability,  $M_c$  is expressed with implicit units (i.e.,  $M_c=5$ ) throughout this chapter and the related appendices.

Connectivity was characterized in a simple manner, by accounting for the presence of the most common network defects. A *dangling chain end* occurs when one chain extender molecule is bound to a crosslinker molecule at only one end. *Dangling chains* are a type of dangling ends, where other types include dangling trees, dangling rings, and more complex unnamed structures. Dangling chains contribute nothing to elastic recovery. Their impact on permeability is, most likely, more complicated: they are likely to provide less of a barrier to diffusion than such chains which are connected to crosslink sites at both ends [49], while providing more barrier than unreacted chain extender molecules (i.e., ones that are not connected to the network at all), as a result of the latter's greater mobility. However, the mobility of chain segments per se was not investigated in this study.

The other network defect reviewed here, a *primary loop*, occurs when one chain extender molecule makes two bonds to a single crosslinker molecule. Although primary loops may contribute to elastic and barrier properties via entanglements, this is improbable because they are unlikely to be large enough to be penetrated by other chains. Therefore, to a first approximation, primary loops may be treated as though they are not network effective at all, in a manner analogous to dangling chains. As a caveat, the likelihood of a loop being speared by other chains increases as the size of the loop increases,

so that for models having higher  $M_c$ s (here, models 3-5 and 4-5), some sparring of primary loops cannot be ruled out. However, the extent of such entanglements was not explored because the prevalence of primary loops in these models was found to be low, as shown below, so their contribution to the overall network effectiveness, if any, would still be negligible.

As a precaution, the phrase *network effectiveness* used here should not be confused with elastic effectiveness. It is not related or to the concepts of elastically effective network chains and cycle rank or to the distinct but related concept of elastically active network chains, which had been discussed in the previous section. An original parameter was used because, while elastic behavior involves the movement of material over a macroscopic scale, diffusion is a local phenomenon.

#### 2.4.2. Analytical Procedure

A depth-first search was used to identify the numbers of bonds, primary loops, and dangling chains at each crosslink site. (Since crosslinking reactions had been performed to conversions of ~98% rather than 100%, the average number of bonds for a given model was slightly lower than its functionality. The average number of bonds is sometimes called the average functionality  $\bar{f}$ , but that term is not used here so as not to confuse it with similar-sounding terms.) From these counts, a net property termed *effective functionality* was calculated for each crosslink junction as follows:

$$\text{Effective Functionality} = \frac{\text{Bonds Made}}{2} - \text{Primary Loops} - \text{Dangling Chains} \quad (2.11)$$

The effective functionality may be understood intuitively as the number of bonds that a given crosslink junction has to its neighboring crosslink sites. In the absence of secondary loops, effective functionality is the number of crosslink junctions that are a given junction's topological first neighbors. For example, junction A in Figure 2.14 has an effective functionality of 1 (3 bonds, 0 loops, 2 dangling chains), as does junction C (4 bonds, 1 loop, 1 dangling chain). For each of these junctions, the crosslink junction that is its sole topological first neighbor is junction B. The effective functionality of junction B in Figure 2.14 is indeterminate because two of its bonds lead to a portion of the network which is not shown in the diagram.

### 2.4.3. Results and Discussion

Simulation cells of the two boundary cases are shown in Figure 2.15, highlighting the various network defects. These visualizations were produced in Blender [50] using add-on software developed as part of this work. Statistical results are shown later in this section. While the incidence of dangling chains was minimal for all models, the occurrence of loops increased with increasing crosslink density. The 6-functional model had, on average, almost one loop per crosslinker molecule, such that its effective functionality was only 4.2. Thus, while model 6-3 still reflects a limiting-case scenario because an effective functionality of  $\sim 4$  in such a small molecule would be impossible in a real-world system for steric reasons, its crosslink density is only slightly higher than the upper limit obtainable in the real world.

Models with  $M_c=3$  were especially prone to forming loops. This was expected based on the small size of their crosslinker molecules because the number density of primary loops  $\rho_{loop}$  is a power law in in loop size. For the present case, expressions derived by Jacobson and Stockmayer [51] for Gaussian chains simplify to the following:

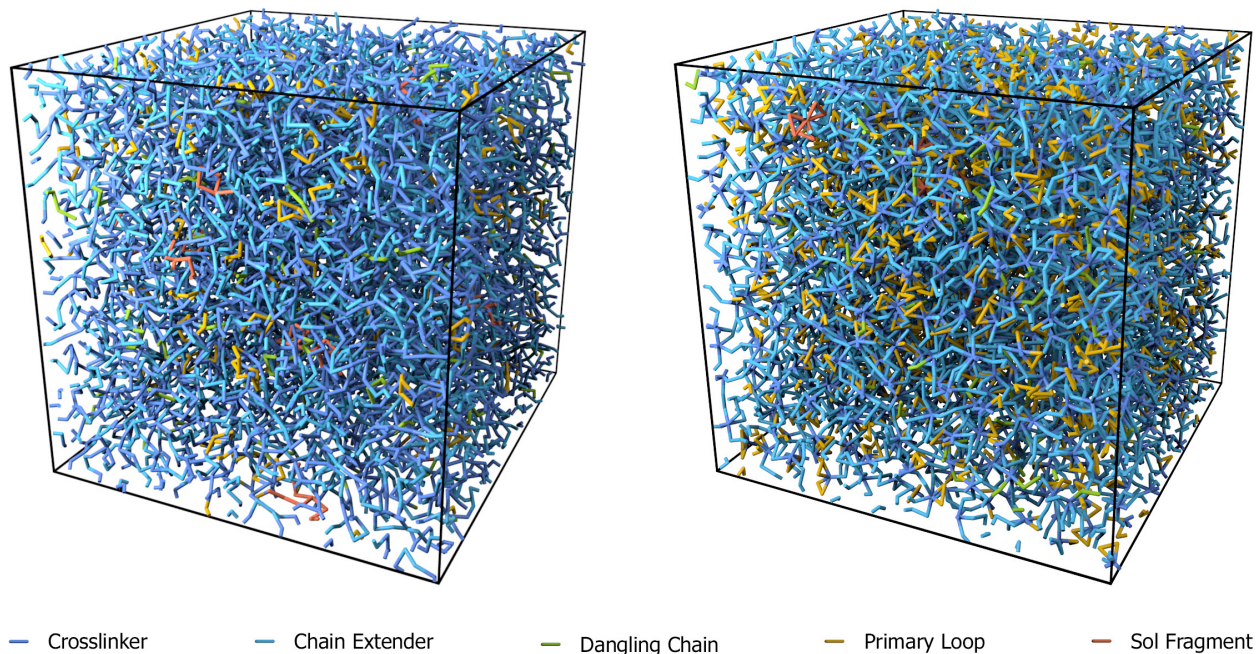


**Figure 2.15.** Snapshots of a one of the samples of each model 3-5 and model 6-3 at  $T=1.0 \epsilon/k_B$  following crosslinking and equilibration. The legend lists color-coded features in order of coloring priority.

$$\rho_{loop} = \frac{1}{2} \left( \frac{3}{2\pi l^2} \right)^{3/2} \cdot X^2 \cdot n^{-3/2} \quad (2.12)$$

where  $n$  is the number of bonds that comprise the loop,  $l$  is the average bond length, and  $X$  is the extent of the crosslinking reaction. For the present systems,  $n$  is numerically equivalent to  $M_c$ , and the bond length at  $T=1.0 \text{ } \varepsilon/k_B$  was  $0.966 \text{ } \sigma$ . In Figure 2.16, data for models 4-3 and 4-5 are compared to this equation and to data published by Duering, Kremer, and Grest for a series of networks which are also 4-functional and which cover a wide complementary range of  $M_c$ s [12]. The comparison is warranted because these literature systems had been modeled using interaction potentials that were similar to the ones in the current work, and had been crosslinked at  $T=1.0 \text{ } \varepsilon/k_B$  using a similar reaction procedure. The equation result is shown using  $X=.984$  which was the average conversion across the models, thus leaving no adjustable parameters. The two datasets are in excellent agreement with each other and with the theoretical prediction.

Next, to observe trends more clearly, data were normalized by the crosslinker functionality  $f$  (Figure 2.17). Then, it may be easily seen that the effectiveness of bonding decreased as the theoretical crosslink density increased. This trend was expected based on simple steric considerations, and it is consistent with real-world results available in the literature. While a spectrometric procedure has recently been developed that allows to quantify primary loops and dangling chains directly [52], it has not yet

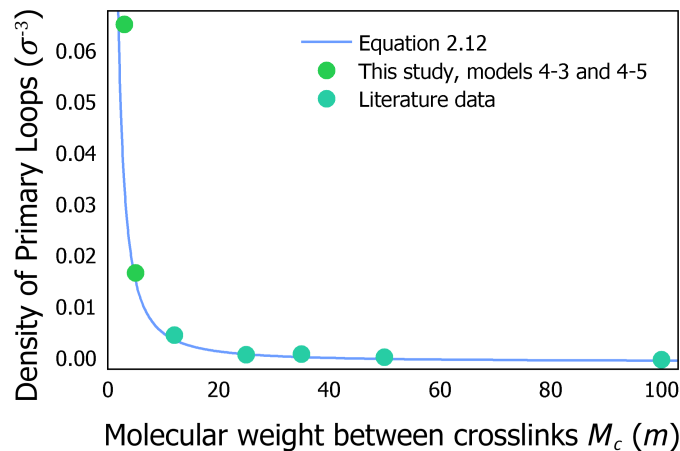


**Figure 2.16.** Comparison of the present data for models 4-3 and 4-5 with data reported by Duering, Kremer, and Grest for analogous systems [12] and with the theoretical prediction of Jacobson and Stockmayer (Equation 2.12) [51].

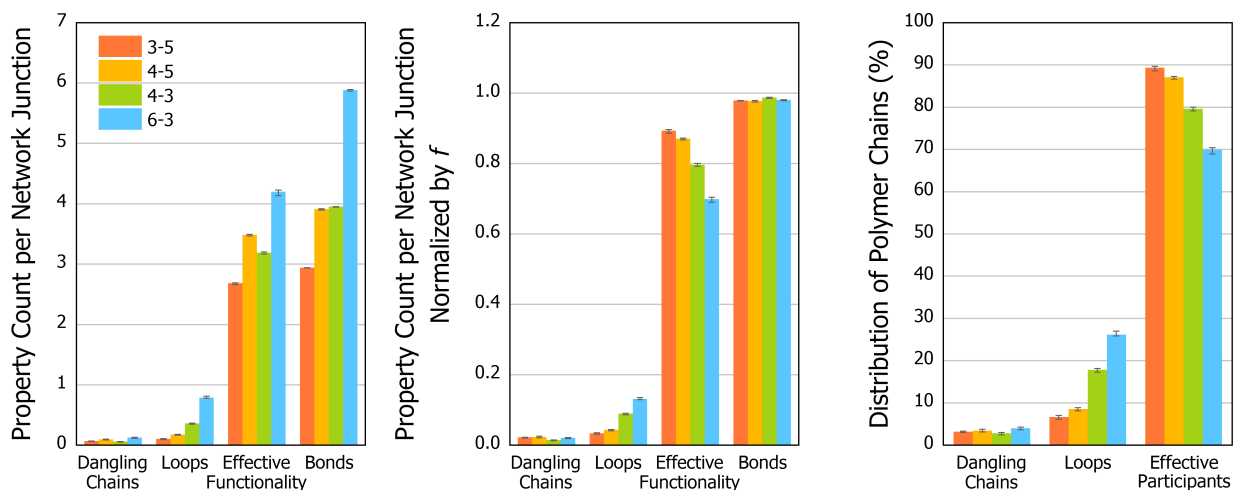


**Figure 2.17.** Prevalence of network defects in the series of thermosets under study. As with earlier figures, error bars in each model-wide property show the smallest and the largest value of the respective sample property. **Left:** Characteristics of the average network junction within each system: the numbers of bonds to chain extender molecules, the numbers of primary loops and dangling chains, and the resulting effective functionality of the average network junction. **Center:** Same data as the left graph, normalized by  $f$ . **Right:** Percentages of polymer chains located in primary loops, in dangling chains, and located topologically between two crosslink junctions.

been applied to series of thermosets. Instead, prevalences of defects are calculated indirectly, based on shear and elastic modulus measurements of bulk and diluted systems at the gel point and at complete conversion, which requires assumptions about the structure of the networks. Nevertheless, these calculations show that the prevalence of loops increases with  $f$  and with decreasing  $M_c$  [53, 54]. However, defects do not fully offset the increases in crosslink density, so that networks with higher  $f$ s and lower  $M_c$ s still have higher actual crosslink densities and higher moduli.

Further, the incidence of defects may be compared to values calculated from real-world modulus data. When these calculations are performed on fully-crosslinked samples, an assumption is made that the incidence of dangling chains is negligible, so that network defects are comprised solely of loops. Calculations are reported as the fraction of crosslinks closing elastically ineffective loops, which is comparable to the metric of primary loops because many larger loops are elastically effective, i.e. most elastically ineffective loops are primary loops. With this in mind, the fraction of crosslinks closing elastically ineffective loops has been calculated as 3-20% for some common systems [53-55]. The extent of looping depends strongly on polymer chemistry, weak for low-functionality long-arm star systems,



strong for free-radical crosslinking, such that 5-15% is considered moderate. That is in accord with the present data, wherein bonds closing primary loops account for 3-13% of all bonds.

Finally, data were normalized using an alternative method, by considering the topological distribution of polymer in each model: how much material was located in primary loops, how much was in dangling chains, and how much was network effective on the local scale. The parameter *locally effective participants* is defined as beads that are situated topologically between two different crosslink junctions. For example, in Figure 2.14, 10 beads are considered effective participants: 4 beads between junctions A and B, 4 beads between junctions B and C, and 2 beads at junction B that lead to the main network. Data are shown as a fraction of chains, rather than a fraction of all beads in each system, to avoid ambiguity that would be presented by crosslink sites such as junction C in Figure 2.14 – i.e., whether those beads should be tallied as belonging to a loop, a dangling chain, or as locally effective participants. Therefore, *chains* are defined here as all beads other than the multifunctional crosslink junctions.

The resulting graph in Figure 2.17 has the same overall shape as the graphs produced by the two prior analyses, but it is interesting quantitatively because the parameter of effective participants accounts for the effects of both  $f$  and  $M_c$ . And, comparing the monotonic trend in this graph to its macroscopic complement, elastically active fraction (Table 2.4), highlights the reason that model 3-5 has a lower elastically fraction than model 4-5: it is not because of poor local connectivity, but rather, lower connectivity on a global level, such as when a large network fraction is connected to the gel by only two paths.

Quantitatively, while in model 3-5, almost 90% of the chains were locally network effective, in model 6-3, only 70% were effective. The remaining 30% of the chains, then, acted to plasticize the network relative to an ideal, defect-free network that could have been synthesized using identical monomers.

This quantity, 30%, is an order of magnitude larger than the amounts of plasticizing additives encountered in real-world coating formulations; many 2K coatings contain no plasticizer at all. However, it is not an error. Some plasticizers are more effective than others at promoting mobility in a specific polymer system. When compared to a plasticizing additive of similar size and chemistry, loops and ends

would be far less effective at promoting mobility because they are bound to the polymer network, – so a far larger volume fraction of loops and ends would be required to achieve the same network mobility as with an additive. In other words, although for the model with the highest crosslink density, an enormous 30% of chains contributed to plasticizing the network, their contribution to plasticization was, most likely, only mild.

## 2.5. Conclusion

A simulated series of thermosets has been synthesized and thoroughly characterized for its thermo-mechanical and topological properties on both the local and the macroscopic scale. Simulation results were in agreement with real-world data, with simulation findings on comparable models published by other groups, and with theoretical considerations: the Jacobson and Stockmayer prediction for the prevalence of primary loops, the combination of Flory-Stockmayer and Carothers' predictions for the location of the gel point, and with the Flory-Erman formulation of the theory of rubber elasticity. Results were additionally explained by referencing kinetic and thermodynamic effects. Through these connections to literature, this work provides a comprehensive treatment of all features of the studied connectivity phenomena.

Further, this work has produced visualizations of topological defects that are more informative than any that exist publicly, to this author's knowledge. They are aesthetically compelling and they relay trends in crosslink density in a manner which is intuitively clear, which renders them suitable for educational purposes in such settings where results communicated solely through statistics would be quickly forgotten.

## 2.6. References

- [1] D. Greenfield, D. Scantlebury. The protective action of organic coatings on steel: A review. *J. Corr. Sci. Eng.* **2000**, 3, 5.
- [2] S.R. Taylor. The role of intrinsic defects in the protective behavior of organic coatings. In M. Kutz (ed.), *Handbook of Environmental Degradation of Materials*, 2<sup>nd</sup> Ed. William Andrew: New York, **2012**, 655-672.
- [3] K. Kremer, F. Müller-Plathe. Multiscale simulation in polymer science. *Mol. Simulat.* **2002**, 28, 729-750.

- [4] V. Varshney, S.S. Patnaik, A.K. Roy, B.L. Farmer. A molecular dynamics study of epoxy-based networks: Cross-linking procedure and prediction of molecular and material properties. *Macromolecules* **2008**, *41*, 6837-6842.
- [5] V. Varshney, S.S. Patnaik, A.K. Roy, B.L. Farmer. Heat transport in epoxy networks: A molecular dynamics study. *Polymer* **2009**, *50*, 3378-3385.
- [6] C. Li, A. Strachan. Molecular simulations of crosslinking process of thermosetting polymers. *Polymer* **2010**, *51*, 6058-6070.
- [7] C. Li, A. Strachan. Molecular dynamics predictions of thermal and mechanical properties of thermoset polymer EPON862/DETDA. *Polymer* **2011**, *52*, 2920-2928.
- [8] N. Nouri, S. Ziaei-Rad. A molecular dynamics investigation on mechanical properties of cross-linked polymer networks. *Macromolecules* **2011**, *44*, 5481-5489.
- [9] N.B. Shenogina, M. Tsige, S.S. Patnaik, S.M. Mukhopadhyay. Molecular modeling approach to prediction of thermo-mechanical behavior of thermoset polymer networks. *Macromolecules* **2012**, *45*, 5307-5315.
- [10] N.B. Shenogina, M. Tsige, S.S. Patnaik, S.M. Mukhopadhyay. Molecular modeling of thermosetting polymers using a dynamic deformation approach. *Polymer* **2013**, *54*, 3370-3376.
- [11] S. Yang, J. Qu. Computing thermomechanical properties of crosslinked epoxy by molecular dynamic simulations. *Polymer* **2012**, *53*, 4806-4817.
- [12] E.R. Duering, K. Kremer, G.S. Grest. Structure and relaxation of end-linked polymer networks. *J. Chem. Phys.* **1994**, *101*, 8169-8192.
- [13] M.J. Stevens. Manipulating connectivity to control fracture in network polymer adhesives. *Macromolecules* **2001**, *34*, 1411-1415.
- [14] M.J. Stevens. Interfacial fracture between highly cross-linked polymer networks and a solid surface: Effect of interfacial bond density. *Macromolecules* **2001**, *34*, 2710-2718.
- [15] M. Tsige, M.J. Stevens. Effect of cross-linker functionality on the adhesion of highly cross-linked networks: A molecular dynamics study of epoxies. *Macromolecules* **2004**, *37*, 630-637.
- [16] M. Tsige, C.D. Lorenz, M.J. Stevens. Role of network connectivity on the mechanical properties of highly cross-linked polymers. *Macromolecules* **2004**, *37*, 8466-8472.
- [17] N.R. Kenkare, S.W. Smith, C.K. Hall, S.A. Khan. Discontinuous molecular dynamics studies of end-linked polymer networks. *Macromolecules* **1998**, *31*, 5861-5879.
- [18] N.J. Soni, P.-H. Lin, R. Khare. Effect of cross-linker length on the thermal and volumetric properties of cross-linked epoxy networks: A molecular simulation study. *Polymer* **2012**, *53*, 1015-1019.
- [19] C. Peter, K. Kremer. Multiscale simulation of soft matter systems. *Faraday Discuss.* **2010**, *144*, 9-24.
- [20] K. Farah, F. Müller-Plathe, M.C. Böhm. Classical reactive molecular dynamics implementations: State of the art. *ChemPhysChem* **2012**, *13*, 1127-1151.
- [21] S.J. Plimpton. Fast parallel algorithms for short-range molecular dynamics. *J. Comp. Phys.* **1995**, *117*, 1-19.

- [22] J.D. Weeks, D. Chandler, H.C. Anderson. Role of repulsive forces in determining the equilibrium structure of simple liquids. *J. Chem. Phys.* **1971**, *54*, 5237-5247.
- [23] K. Kremer, G.S. Grest. Dynamics of entangled linear polymer melts: A molecular-dynamics simulation. *J. Chem. Phys.* **1990**, *92*, 5057-5086.
- [24] L.J. Fetters, D.J. Lohse, R.H. Colby. Chain dimensions and entanglement spacings. In J.E. Mark (ed.), *Physical Properties of Polymers Handbook*, 2<sup>nd</sup> Ed. Springer: New York, **2007**, 447-454.
- [25] T. Schneider, E. Stoll. Molecular-dynamics study of a three-dimensional one-computer model for distortive phase transitions. *Phys. Rev. B* **1978**, *17*, 1302-1322.
- [26] B. Dünweg, W. Paul. Brownian dynamics simulations without Gaussian random numbers. *Int. J. Mod. Phys. C* **1991**, *2*, 817-827.
- [27] W. Shinoda, M. Shiga, M. Mikami. Rapid estimation of elastic constants by molecular dynamics simulation under constant stress. *Phys. Rev. B* **2004**, *69*, 134103.
- [28] M.E. Tuckerman, J. Alejandre, R. López-Rendón, A.L. Jochim, G.J. Martyna. A Liouville-operator derived measure-preserving integrator for molecular dynamics simulations in the isothermal-isobaric ensemble. *J. Phys. A: Math. Gen.* **2006**, *39*, 5629-5651.
- [29] V.B. Gupta, L.T. Drzal, C.Y.-C. Lee., M.J. Rich. The temperature-dependence of some mechanical properties of a cured epoxy resin. *Polym. Eng. Sci.* **1985**, *25*, 812-823.
- [30] D. York, N.M. Evensen, M.L. Martínez, J. De Basabe Delgado. Unified equations for the slope, intercept, and standard errors of the best straight line. *Am. J. Phys.* **2004**, *72*, 367-375.
- [31] P.J. Flory. Molecular theory of rubber elasticity. *Polymer* **1979**, *20*, 1317-1320.
- [32] P.J. Flory. Theory of elasticity of polymer networks. The effect of local constraints on junctions. *J. Chem. Phys.* **1977**, *66*, 5720-5729.
- [33] P.J. Flory, B. Erman. Theory of elasticity of polymer networks. 3. *Macromolecules* **1982**, *15*, 800-806.
- [34] P.J. Flory. Elastic activity of imperfect networks. *Macromolecules* **1982**, *15*, 99-100.
- [35] H.J. Herrmann, D.C. Hong, H.E. Stanley. Backbone and elastic backbone of percolation clusters obtained by the new method of 'burning'. *J. Phys. A: Math. Gen.* **1984**, *17*, L261-L266.
- [36] E.R. Duering, K. Kremer, G.S. Grest. Structural properties of randomly crosslinked polymer networks. *Prog. Coll. Pol. Sci.* **1992**, *90*, 13-15.
- [37] J.P. Queslel, J.E. Mark. Molecular interpretation of the moduli of elastomeric polymer networks of known structure. *Adv. Polym. Sci.* **1984**, *65*, 135-176.
- [38] F.H. Stillinger, P.G. Debenedetti. Glass transition thermodynamics and kinetics. *Annu. Rev. Condens. Matter Phys.* **2013**, *4*, 263-285.
- [39] J. Bicerano. *Prediction of Polymer Properties*, 3<sup>rd</sup> Ed. Marcel Dekker: New York, **2002**, 366-369.
- [40] K. Sato. The internal stress of coating films. *Prog. Org. Coat.* **1980**, *8*, 143-160.

- [41] R.J. Crowson, R.G.C. Arridge. Linear viscoelastic properties of epoxy resin polymers in dilatation and shear in the glass transition region: 2. Measurement of the glass transition temperature. *Polymer* **1979**, *20*, 747-754.
- [42] K.G. Häusler, P. Hauptmann, C. Meischner, M. Fedtke, E. Härtel, S. Wartewig. Ultrasonic investigations of modified epoxies. *Polym. Commun.* **1987**, *28*, 154-157.
- [43] A. Tcharkhtchi, S. Faivre, L.E. Roy, J.P. Trotignon, J. Verdu. Mechanical properties of thermosets. *J. Mater. Sci.* **1996**, *31*, 2687-2692.
- [44] J. Verdu, A. Tcharkhtchi. Elastic properties of thermosets in glassy state. *Angew. Makromol. Chem.* **1996**, *240*, 31-38.
- [45] N.W. Tschoegl, W.G. Knauss, I. Emri. Poisson's ratio in linear viscoelasticity – a critical review. *Mech. Time-Depend. Mat.* **2002**, *6*, 3-51.
- [46] A.A. Bondi. *Physical Properties of Molecular Crystals, Liquids, and Glasses*. Wiley: New York, **1968**, 402.
- [47] G.N. Greaves, A.L. Greer, R.S. Lakes, T. Rouxel. Poisson's ratio and modern materials. *Nat. Mater.* **2011**, *10*, 823-837.
- [48] D.H. Armitage, C. Cameron, A.H. Fawcett, C.R. Hetherington, F.V. McBride, R.A.W. Mee. Cycles within micronets and at the gel point. *Macromolecules* **2000**, *33*, 6569-6577.
- [49] E.R. Duering, K. Kremer, G.S. Grest. Relaxation of randomly cross-linked polymer melts. *Phys. Rev. Lett.* **1991**, *67*, 3531-3534.
- [50] Blender Foundation. Blender version 2.70a (released 11 April 2014) is available at blender.org. The current version of Blender is 2.74.
- [51] H. Jacobson, W.H. Stockmayer. Intramolecular reaction in polycondensations. I. The theory of linear systems. *J. Chem. Phys.* **1950**, *18*, 1600-1606.
- [52] H. Zhou, J. Woo, A.M. Cok, M. Wang, B.D. Olsen, J.A. Johnson. Counting primary loops in polymer gels. *P. Natl. Acad. Sci. USA* **2013**, *109*, 19119-19124.
- [53] R.F.T. Stepto. Non-linear polymerization, gelation and network formation, structure and properties. In R.F.T. Stepto (ed.), *Polymer Networks: Principles of Their Formation, Structure, and Properties*. Blackie Academic and Professional: New York, **1998**, 14-63.
- [54] K. Dušek, M. Dušková-Smrčková, J. Huybrechts, A. Ďuračková. Polymer networks from preformed precursors having molecular weight and group reactivity distributions. Theory and application. *Macromolecules* **2013**, *46*, 2767-2784.
- [55] K. Dušek, M. Gordon, S.B. Ross-Murphy. Graphlike state of matter. 10. Cyclization and concentration of elastically active network chains in polymer networks. *Macromolecules* **1978**, *11*, 236-245.

## APPENDIX A. INFRARED ANALYSIS OF OIL PAINT AND FILMS

### A.1. Introduction

Infrared spectroscopy is used widely both in art conservation and in polymer science. The instrumentation is widely available, sample sizes are small, sample preparation is minimal, data collection is fast, and spectral interpretations are straightforward to a large extent. Infrared spectra allow to identify the presence of some functional groups within a material sample. However, their concentrations are estimated only rarely because some moieties are more IR-active than others and because the exact amount of analyte located in the spectrometer's light path cannot be known. Further, the intensity of the CH stretch vibrations, which is often used to approximate sample size with other polymers, does not appear to be a reliable marker in the case of aged oil paint, whose chemistry is especially complex [1]. For such samples, quantitative analysis requires that an inert internal standard be used.

Naturally aged oil paint models, both neat and pigmented, have already been studied in some detail by Meilunas *et al.* [2] and by van der Weerd *et al.* [1]. Therefore, the content of this appendix is presented not as a standalone study but as a supplement to the structural investigation of the same films presented in Chapter 1, which also contains the details of the analytical procedure used. Indeed, the methodology of using inverted second derivative spectra to locate absorption bands follows the study by van der Weerd *et al.*, any many of the pigments in the two libraries are the same.

### A.2. Results

#### A.2.1. Unpigmented Oil

##### A.2.1.1. Fresh Unpigmented Oils

Infrared spectra of fresh cold-pressed and refined linseed oils, Figures A.1 and A.2, are nearly identical to one another and to the literature [1,2]. Alkane CH<sub>2</sub> stretches are observed at 2926 and 2854 cm<sup>-1</sup>, with a CH<sub>3</sub> shoulder at 2955 cm<sup>-1</sup>. CH<sub>2</sub> scissor and CH<sub>3</sub> asymmetric bend both appear at 1464 cm<sup>-1</sup>, and the CH<sub>3</sub> umbrella bending is at 1377 cm<sup>-1</sup> [2]. *Cis* bonds are detected by an unconjugated, symmetrically di-substituted C-H stretch at 3010 cm<sup>-1</sup>, a *cis* C=C stretch at 1654 cm<sup>-1</sup>, and a *cis* out-of-plane bend at 723 cm<sup>-1</sup> [1]. A *trans* out-of-plane bend, which had been previously detected in

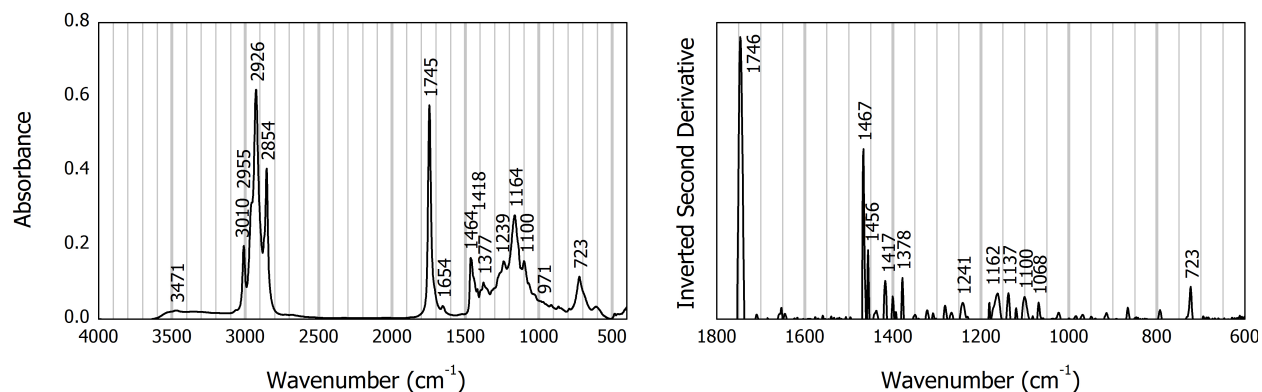


**Figure A.1.** Infrared spectrum of fresh cold-pressed linseed oil (left) and its second derivative, inverted (right).

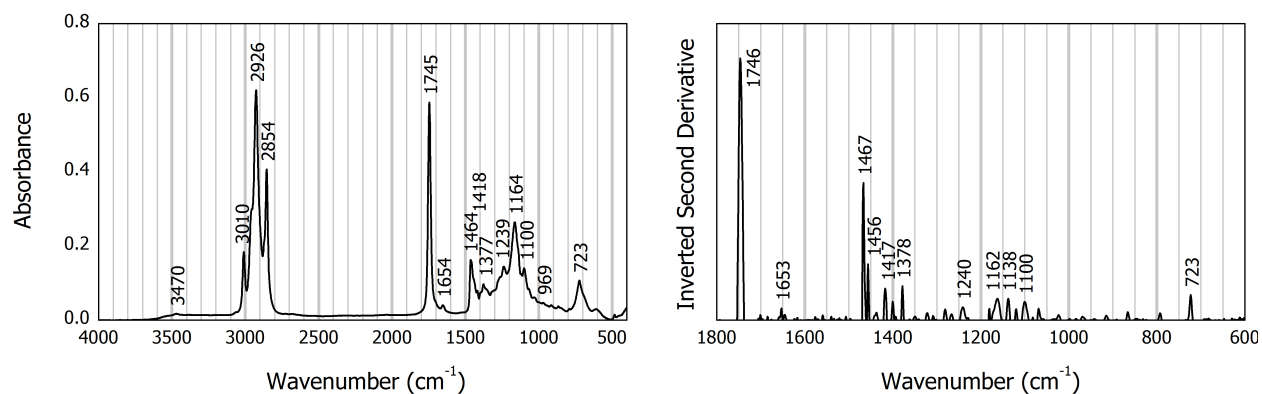


**Figure A.2.** Infrared spectrum of fresh refined linseed oil (left) and its second derivative, inverted (right).

aged films [1,2], is identifiable at 971 cm<sup>-1</sup>, but its peak size is negligible. No conjugated double bonds, which had been detected in stand oil at 947 and 988 cm<sup>-1</sup> [2], are observed.

The carbonyl band at 1745 cm<sup>-1</sup> and the C-O triplet at 1239, 1164, and 1100 cm<sup>-1</sup> are characteristic of the triglyceride ester linkages [1,2]. The weak band at 3471 cm<sup>-1</sup> is due to hydroxyls and hydroperoxides that form upon oxidation. Another weak band at 1418 cm<sup>-1</sup> is due to a combination of C-O stretching and O-H deformation vibrations in carboxylic acids. However, no acidic carbonyl band at ~1715 cm<sup>-1</sup> is observed.

#### A.2.1.2. Aged Unpigmented Oil

Infrared spectra of aged linseed oil have been studied by Meilunas *et al.* [2] and by van der Weerd *et al.* [1]. Meilunas had examined changes in spectra caused by thermally aging raw linseed oil at

120°C for 24 hours, as well as a spectrum of linseed oil film that was stored under ambient museum conditions for 55 years. Van der Weerd *et al.* had analyzed changes in spectra that occur during the first 90 hours after applying a film of cold-pressed linseed oil, as well as a spectrum of stand oil that was stored in a low-oxygen atmosphere at ambient museum conditions for 50 years after production.

The spectrum of the present naturally aged sample, Figure A.3, has a broad and strong O-H stretch which spans from 3500 to 2500  $\text{cm}^{-1}$ , somewhat broader and stronger than those reported in the above two studies. However, this might be in part an artifact of the low values of absorbance. Otherwise, this spectrum is quite similar to that of the 50-year-old stand oil reported by van der Weerd *et al.* As in that case, the carboxylic acid carbonyl peak at 1716  $\text{cm}^{-1}$  is distinct from the ester carbonyl at 1742  $\text{cm}^{-1}$ , which is weak relative to the CH stretches. Further, the ester triplet is barely distinguishable (1224, 1150, and 1081  $\text{cm}^{-1}$ ) and is deformed from its usual positions. Comparison to the spectra of fresh linseed oils shows that much of the starting triglycerides have been hydrolyzed to glycerols and free fatty acids, as expected based on the sample's lack of cohesion.

## A.2.2. Films Containing Inert Pigments

### A.2.2.1. Introduction

Several inorganic materials, including silica, barium sulfate, and calcium carbonate, are generally considered inert in the medium of oil paint. Silica is not a pigment itself, but it is a common impurity in so-called earth colors due to its ubiquity in geology. Barium sulfate and calcium carbonate are extender

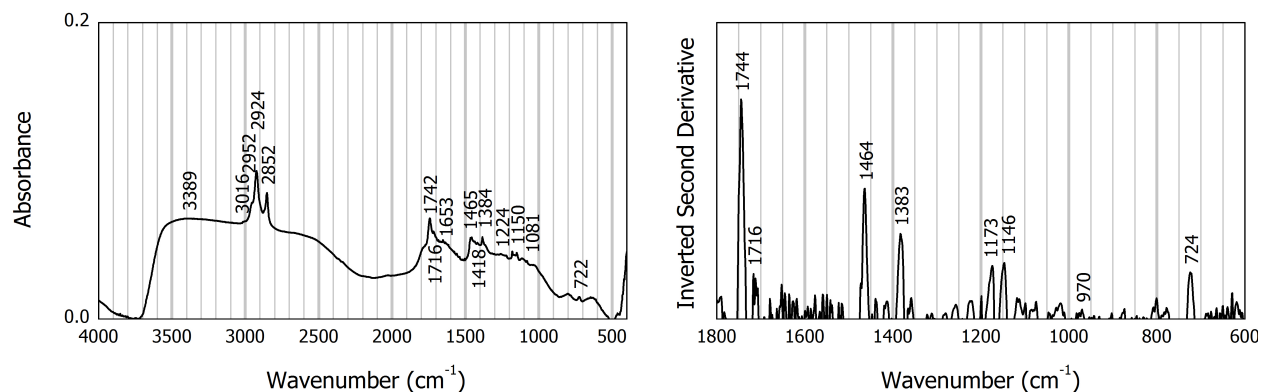


**Figure A.3.** Infrared spectrum of a 12.3-year-old unpigmented cold-pressed linseed oil film (left) and its second derivative, inverted (right).



pigments which are often mixed with primaries by pigment manufacturers. Since two of these materials are identified as impurities in some of the current paint models, films manufactured with these inert pigments are presented first, prior to discussing films which are the focus of this study.

#### A.2.2.2. Silica

Paint containing silica,  $\text{SiO}_2$ , has an IR spectrum (Figure A.4) that is superficially similar to the spectra of neat linseed oils owing to the scarcity of pigment absorption bands. In addition to sharp bands at lower wavenumbers, silica has a broad absorption from 1500 to approximately  $800\text{ cm}^{-1}$ , centered presently at  $1061\text{ cm}^{-1}$  (second derivative) [3]. This absorption does not mask organic bands but it does distort the baseline.

All the pigment peaks occur at slightly higher wavenumbers in the present spectrum than in the references [3]. The peak at  $801\text{ cm}^{-1}$  corresponds to reference peaks at  $798\text{--}777\text{ cm}^{-1}$ , the peak at  $552\text{ cm}^{-1}$  corresponds to reference peaks at  $520\text{--}511\text{ cm}^{-1}$ , and the peak at  $472\text{ cm}^{-1}$  occurs in references at  $461\text{--}459\text{ cm}^{-1}$ . As a result of this shift, and accounting for the relative intensities of these bands, the peak at  $727\text{ cm}^{-1}$  is assigned to a pigment absorption, which occurs at  $695\text{--}692\text{ cm}^{-1}$  in the references, rather than to a *cis* out-of-plane bend. Organic bands are assigned analogously here as with neat linseed oils. Organic assignments for this and all other films in this study are summarized in Section A.3.

#### A.2.2.3. Barium Sulfate

The spectrum of the paint pigmented with  $\text{BaSO}_4$ , Figure A.5, is dominated by pigment

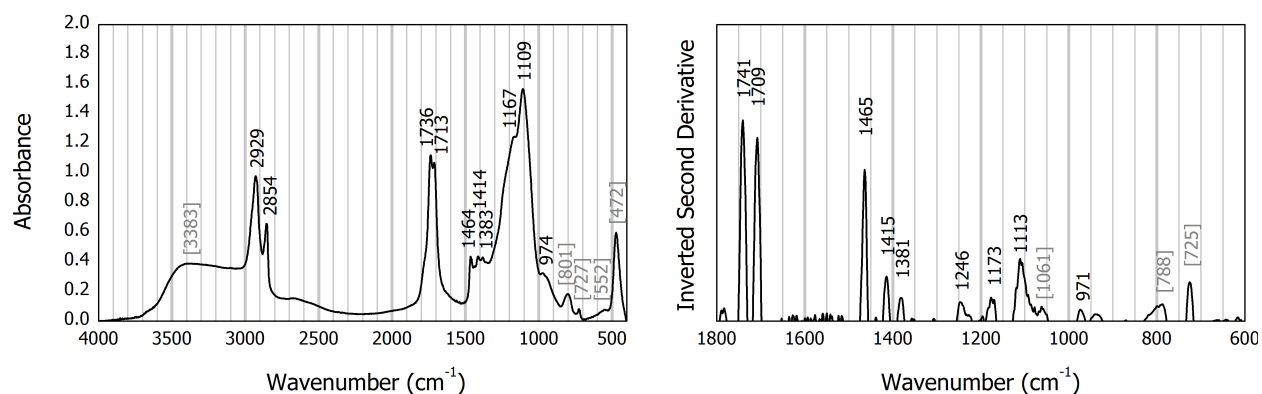


**Figure A.4.** Infrared spectrum of an 18.8-year-old oil paint pigmented with Silica (left) and its second derivative, inverted (right). [Square brackets] indicate pigment bands.

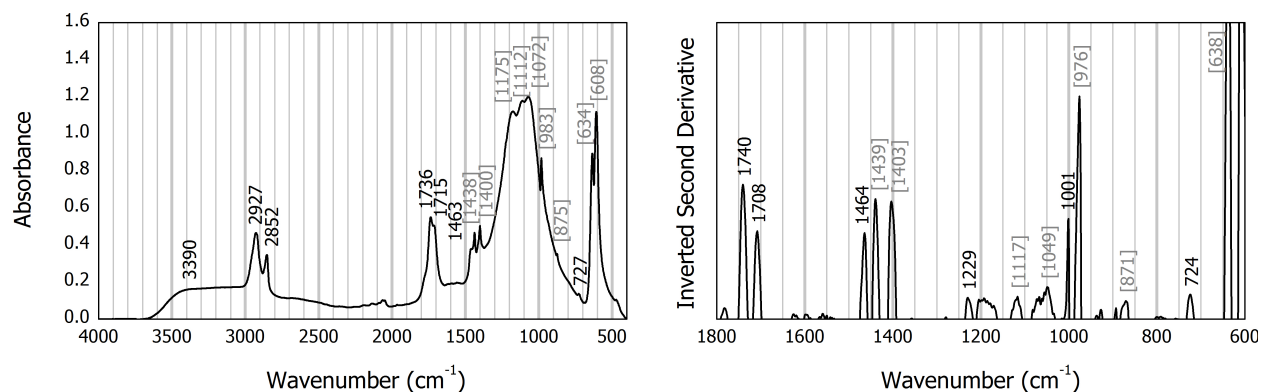


**Figure A.5.** Infrared spectrum of an 18.8-year-old oil paint pigmented with Barium Sulfate (left) and its second derivative, inverted (right).

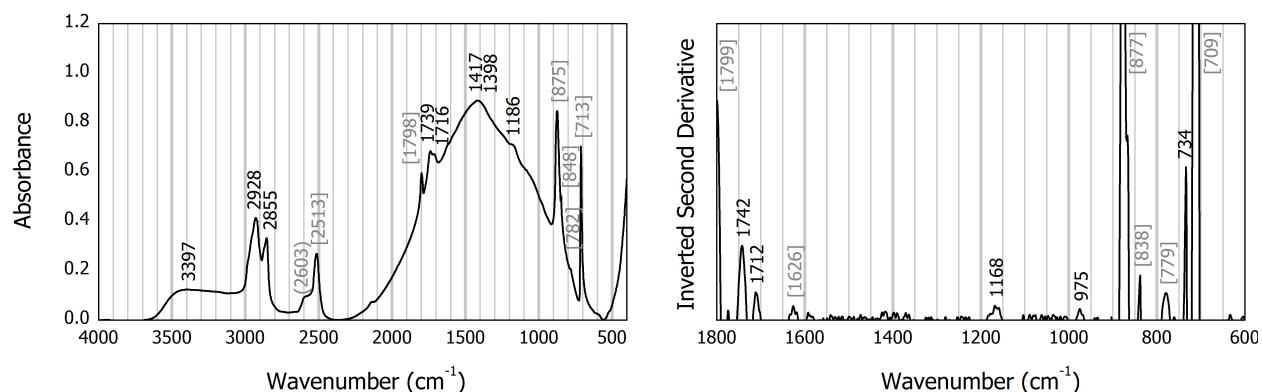


**Figure A.6.** Infrared spectrum of an 18.8-year-old oil paint pigmented with Calcium Carbonate (left) and its second derivative, inverted (right). (Parentheses) indicate a shoulder peak.

absorptions. The right-hand area of the spectrum consists almost entirely of BaSO<sub>4</sub> bands at 1175, 1112, 1072, 983, 875, 634, and 608 cm<sup>-1</sup> [4]. In addition, the pair of bands at 1438 and 1400 cm<sup>-1</sup> is present in one reference spectrum of Barium Sulfate pigment but is absent from two others [3], indicating that it is caused by common impurities. The OH absorption at 3390 cm<sup>-1</sup> may be also due to the pure pigment [3].

#### A.2.2.4. Calcium Carbonate

The pigment calcium carbonate, CaCO<sub>3</sub>, occurs in several mineralogical forms. The form that was used in the manufacture of the calcium carbonate paint whose IR spectrum is shown in Figure A.6 is identified through the absorption bands at 875 and 713 cm<sup>-1</sup> as calcite, which is also the most common form [5]. Calcium carbonate has a strong, broad absorption in the region between 2000-600 cm<sup>-1</sup> which accounts for the overall shape of the right-hand side of the spectrum. Other bands are located at 2603

(shoulder), 2513, 1798, and 848  $\text{cm}^{-1}$  [3]. A second derivative band at 1626  $\text{cm}^{-1}$  and a weak band at 782  $\text{cm}^{-1}$  are assigned to calcium oxalate,  $\text{CaC}_2\text{O}_4$ , as discussed in Section A.2.6.2.

### A.2.3. Films Pigmented with Lead

#### A.2.3.1. White Lead

Spectra of the two films pigmented with White Lead, Figures A.7 and A.8, are remarkably similar to each other and also to the literature spectra for much older films of similar composition [1]. The broad intense absorption at 1405  $\text{cm}^{-1}$  in Figure A.7 is due to carbonates in the pigment,  $2\text{PbCO}_3 \cdot \text{Pb}(\text{OH})_2$ , as are the less intense absorptions at 1044 and 773  $\text{cm}^{-1}$  and the characteristic band at 682  $\text{cm}^{-1}$  [1,6]. The absorption at 3536  $\text{cm}^{-1}$  is a pigment O-H stretch. Absorptions at 2428 and 852  $\text{cm}^{-1}$  are from neutral  $\text{PbCO}_3$ , which is a common impurity in White Lead [1].

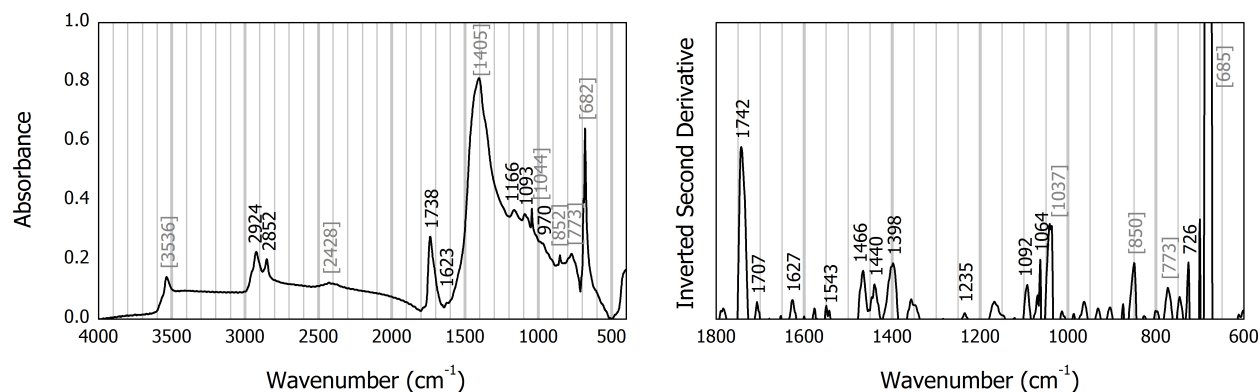


**Figure A.7.** Infrared spectrum of a 21.0-year-old oil paint pigmented with White Lead (left) and its second derivative, inverted (right).

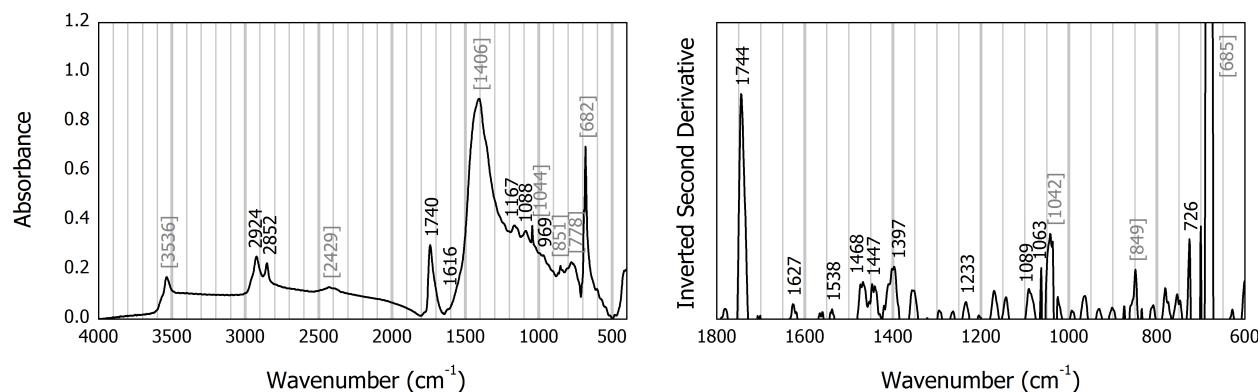


**Figure A.8.** Infrared spectrum of an 11.3-year-old oil paint pigmented with White Lead (left) and its second derivative, inverted (right).

Nearly all indications of carboxylic acids are absent. Instead, a weak feature at  $1623\text{ cm}^{-1}$  and a second-derivative band at  $1543\text{ cm}^{-1}$  signal the formation of lead carboxylates [1,2]. As degradation proceeds, carboxylic acids do not accumulate and lead carboxylate complexes are formed instead.

#### A.2.3.2. Naples Yellow

The collection of an IR spectrum of the film pigmented by Naples Yellow,  $\text{Pb}_3(\text{SbO}_4)_2$ , suffered from strong scattering (Figure A.9). Although diagnostic features are able to be located, most of them are vague, so only tentative interpretations may be made. Van der Weerd *et al.*, who collected spectra of a comparable film in a diamond cell, did not experience this problem [1]. The strong peak at  $632\text{ cm}^{-1}$  and the shoulder at  $780\text{ cm}^{-1}$  are due to the pigment [7].

In examining a much older film pigmented with Naples Yellow, van der Weerd *et al.* found little evidence of carboxylic acids and assigned the absorption at  $1413\text{ cm}^{-1}$  to the symmetric  $\text{COO}^-$  stretch of metal carboxylates [1,10]. However, that assignment was additionally based on the presence of an asymmetric  $\text{COO}^-$  band at  $1548\text{ cm}^{-1}$ , which is not apparent here.

#### A.2.4. Films Pigmented with Zinc

Pure ZnO absorbs strongly between  $590\text{--}400\text{ cm}^{-1}$  but has no distinctive bands at higher wavenumbers. However, van der Weerd *et al.* reported an impurity of  $\text{CaCO}_3$  in their sample of Zinc White paint [1]. Comparison to reference [8] confirms that the band at  $887/881\text{ cm}^{-1}$  in the present spectra of the films pigmented with Zinc White, Figures A.10 and A.11, is due to this impurity. The

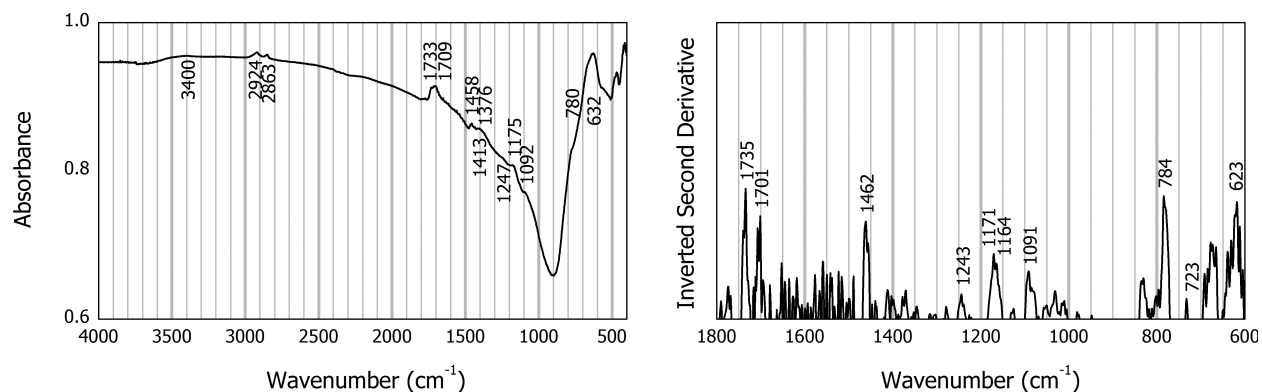


**Figure A.9.** Infrared spectrum of an 18.8-year-old oil paint pigmented with Naples Yellow (left) and its second derivative, inverted (right).

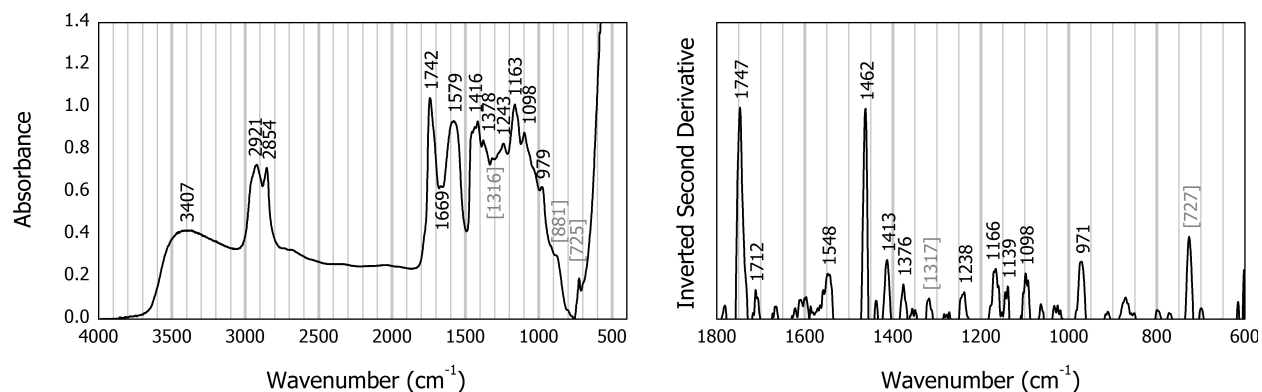


**Figure A.10.** Infrared spectrum of a 20.8-year-old oil paint pigmented with Zinc White (left) and its second derivative, inverted (right).

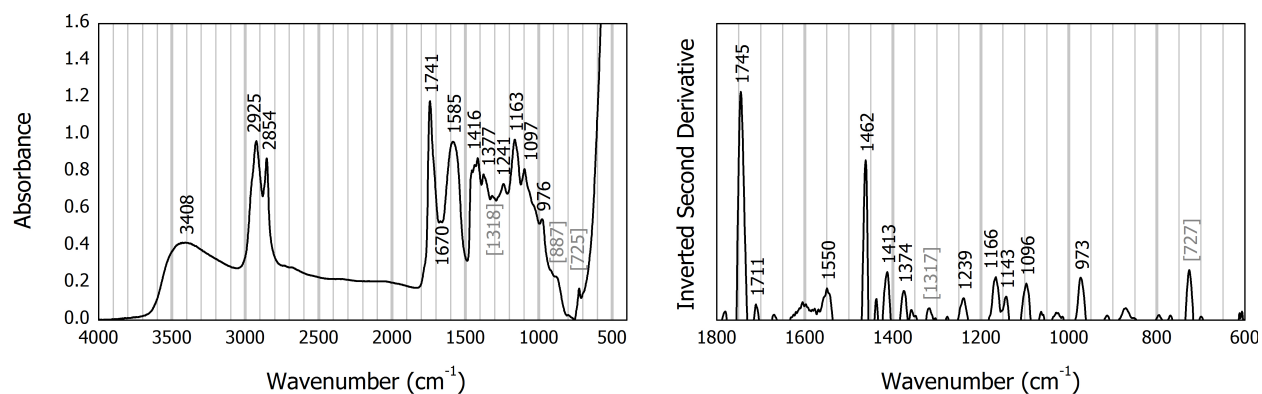


**Figure A.11.** Infrared spectrum of a 12.2-year-old oil paint pigmented with Zinc White (left) and its second derivative, inverted (right).

spectrum of  $\text{CaCO}_3$  also has a broad absorption between approximately  $2200\text{--}1000\text{ cm}^{-1}$  which is responsible for the high baseline in the corresponding region, as well as a sharp peak at  $725\text{ cm}^{-1}$  which masks one of the weak alkene features.

The broad absorption at  $1579\text{ cm}^{-1}$  was assigned by van der Weerd *et al.* to zinc carboxylates [1]. In that spectrum, the broad peak was composed of several peaks, which suggested coordination to different fatty acids. For example, zinc palmitate has its main absorption peak (which is due to the asymmetric  $\text{COO}^-$  stretch) located at  $1538\text{ cm}^{-1}$  [9]. In zinc stearate, this peak appears at  $1540\text{ cm}^{-1}$ , and in zinc oleate, at  $1526/1548\text{ cm}^{-1}$  [10]. Although the present  $\text{COO}^-$  peak cannot be conclusively resolved into such composing peaks (potentially due to greater noise), its breadth suggests that multiple coordination structures are present.

The band at  $1669\text{ cm}^{-1}$  is assigned to an alkene C=C stretch. This attribution is somewhat surprising because, given the paint film's cohesion and macroscopic rigidity, oxidative crosslinking is expected to have completed much earlier than 20 years. However, this assignment is supported by considering the spectrum of 60-year-old Zinc White paint that was reported by van der Weerd *et al.* [1]. Since that paint is much older, if crosslinking is still in progress, it would retain fewer alkene moieties than the present paint, – and indeed, its corresponding band at  $1663\text{ cm}^{-1}$  is discernible using only the second derivative spectrum. Further, in the present spectra, an impurity of calcium oxalate is assigned to the weak absorptions at  $1316/1318\text{ cm}^{-1}$ , as discussed in Section A.2.6.2. However, calcium oxalate is expected to have a second, slightly weaker band at  $\sim 1620\text{ cm}^{-1}$ , which cannot be unambiguously identified in the present spectra – so the question arises whether the  $1670\text{ cm}^{-1}$  band may be due to the oxalate C=C stretch. However, the spectrum of Zinc White paint reported by van der Weerd *et al.* resolves that concern as well: in that second derivative spectrum, the  $1663\text{ cm}^{-1}$  band is distinct from a strong  $1620\text{ cm}^{-1}$  band. Therefore, the possibility that the  $1669\text{ cm}^{-1}$  band in the present spectrum is due to oxalates must be excluded. Finally, since the 12-year-old unpigmented oil paint film in the present study (Section A.2.1.2) has a C=C stretch at  $1653\text{ cm}^{-1}$ , the finding that alkene functionality still exists after 20 years has unambiguous precedent.

### **A.2.5. Films Pigmented with Copper**

The pigment Malachite, written as  $\text{CuCO}_3\cdot\text{Cu}(\text{OH})_2$ , is not a coordination complex of copper but, rather, a lattice composed of  $\text{Cu}^{2+}$ ,  $\text{OH}^-$ , and  $\text{CO}_3^{2-}$  ions [11]. As a result, many variations of interactions are possible, and the IR spectrum of Malachite paint is dominated by pigment absorptions (Figure A.12). Cu-O bands appear at  $571, 524, 503, 427\text{ cm}^{-1}$  and at lower wavenumbers, and do not obscure organic features. However, strong carbonate absorptions at  $1506, 1418, \text{ and } 1390\text{ cm}^{-1}$  may mask a possible acid combination band. Pigment O-H have two bending modes at  $1047\text{ and } 873\text{ cm}^{-1}$  and two stretching ones at  $3402\text{ and } 3312\text{ cm}^{-1}$ . The presence of pigment hydroxyls masks any organic OH functionality that may also exist. Pigment carbonates exhibit other bands at  $1096, 820, 748, \text{ and } 712\text{ cm}^{-1}$ , and at  $1803\text{ cm}^{-1}$  on the second derivative spectrum. A weak absorption at  $775\text{ cm}^{-1}$  is likely due to an ochre-like impurity

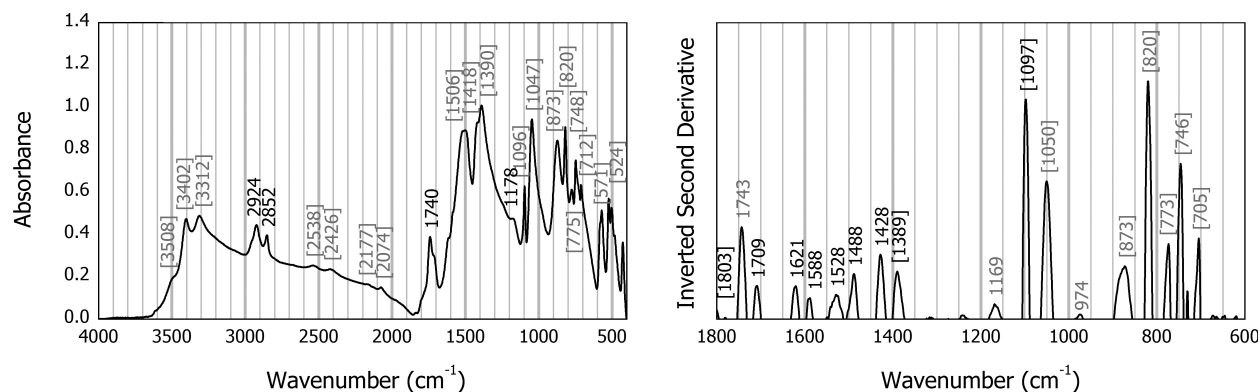


**Figure A.12.** Infrared spectrum of an 18.7-year-old oil paint pigmented with Malachite (left) and its second derivative, inverted (right).

[11]. Additional secondary bands are identified at 3508 (shoulder), 2538, 2426, 2177, 2074  $\text{cm}^{-1}$  by comparison with references [3].

Despite extensive pigment absorptions, some conclusions can be made. The acid carbonyl appears only as a shoulder at 1709  $\text{cm}^{-1}$  (second derivative), indicating that the acid content in the sample is low, but not as low as for paint pigmented with lead or zinc, where not even a shoulder is distinct. Copper soaps are identified by the second derivative peak at 1588  $\text{cm}^{-1}$ , seen as a shoulder on the absorption spectrum, by noting that copper palmitate absorbs at  $\sim 1580 \text{ cm}^{-1}$  [9] while copper stearate, at  $\sim 1586 \text{ cm}^{-1}$  [10]. (This apparent difference in band locations is most likely due to experimental differences, as metal palmitates and stearates are not expected to differ in the location of their  $\text{COO}^-$  bands [12].) Therefore, the acid content is low because some acids are consumed in soaps; however, soap-formation is not as favorable with Malachite as it is for zinc and lead-based pigments.

## A.2.6. Films Pigmented with Iron

### A.2.6.1. Introduction

Iron-based pigments are often called *earth colors* because they are sourced by mining. Once extracted from nature, they are purified to increase color strength. Nonetheless, impurities in naturally-derived iron-based pigments remain common.

### A.2.6.2. Red Iron Oxide

The film pigmented with red iron oxide, Figure A.13, contains many inorganic features. Pure  $\text{Fe}_2\text{O}_3$  absorbs at 540 and 460  $\text{cm}^{-1}$ , with a shoulder at  $\sim 610 \text{ cm}^{-1}$ , but it has no features at higher wavenumbers [13] – so the other inorganic absorptions are due to impurities. The strong absorption at 1038  $\text{cm}^{-1}$  is assigned to the Si-O-Si stretch in silica, and it affects the baseline in the region between 1200-900  $\text{cm}^{-1}$  [3,14]. Bands at 2613 (shoulder), 2527, 877, and 713  $\text{cm}^{-1}$  are assigned to  $\text{CaCO}_3$ , which also has a strong peak centered at 1437  $\text{cm}^{-1}$  (second derivative) that distorts the baseline between 1800-1100  $\text{cm}^{-1}$  [5].

The sharp band at 1317  $\text{cm}^{-1}$  is characteristic of calcium oxalate,  $\text{CaC}_2\text{O}_4$ , which has another absorption at 1621  $\text{cm}^{-1}$  due to the oxalate C=C stretch, and an additional strong band at 783  $\text{cm}^{-1}$  [8]. Oxalates are frequently encountered on outdoor cultural artifacts that are exposed to weathering, but only rarely in easels and canvas paintings which are housed indoors. In those latter cases, the oxalate anions have been said to originate from degradation of the protective varnish coating [15,16]. Clearly, such a mechanism is not relevant with unvarnished paint models, – so calcium oxalate had apparently not been considered as a possible impurity in the study by van der Weerd *et al.* [1]. For example, that library includes a paint model that is pigmented with Green Earth whose IR spectrum has distinct bands at 1624 and 1323  $\text{cm}^{-1}$  (as well as a second derivative band at 781  $\text{cm}^{-1}$ , although this last band is not characteristic on its own). The presence of  $\text{CaCO}_3$  in that film is noted. Yet, although the 1624  $\text{cm}^{-1}$  band

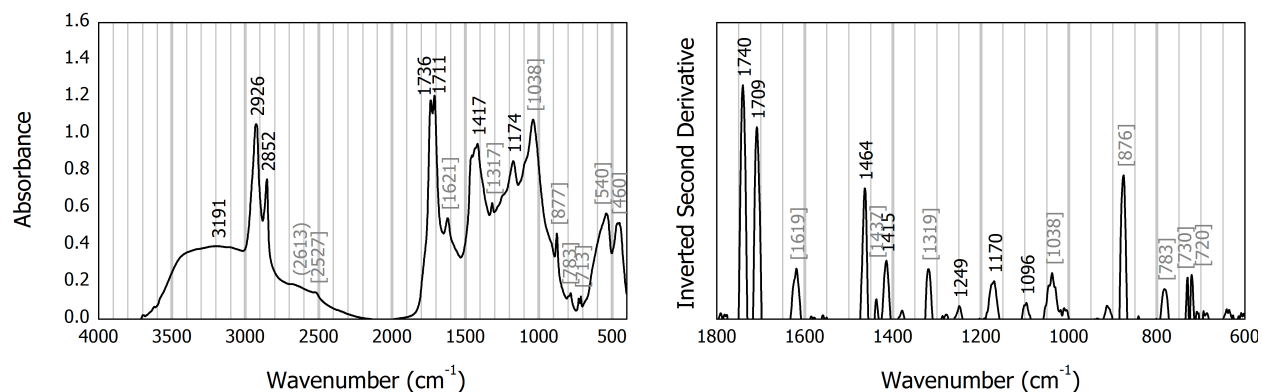


**Figure A.13.** Infrared spectrum of an 18.7-year-old oil paint pigmented with Red Iron Oxide (left) and its second derivative, inverted (right).



is discussed, it is left unattributed. In reviewing the current spectra and the spectra presented by van der Weerd, *et al.*, it becomes appreciable that unambiguous bands at  $\sim 1620$  and  $\sim 1320$   $\text{cm}^{-1}$  coincide with unambiguous  $\text{CaCO}_3$  features, which supports the assignment of calcium oxalate.

Further, in examining an embedded cross-section of an easel painting, the same group had discussed co-occurring bands at  $1650$  and  $1326$   $\text{cm}^{-1}$ , but judged the presence of oxalates as unlikely [17]. (The varnish of that painting was not discussed as a potential source of oxalate ions probably because these bands did not appear in the spectra of the varnish layer.) Instead, a hypothesis was proposed that the bands were due to  $\text{CaCO}_3$  and were altered from their usual positions by the *reststrahlen* effects [18,19] associated with the reflection mode in which those IR spectra had been collected. Although such an explanation is plausible in that particular case, it does not apply to the spectra of the paint models, either in the current study or those collected by van der Weerd *et al.*, since both these spectral libraries had been collected by transmission. While the evidence for the presence of oxalates is not conclusive, oxalates provide the best available explanation of the observed spectral features. Perhaps oxalate anions are able to originate from the degraded oil paint itself.

#### A.2.6.3. Raw Sienna

Ochres are natural substances that consist of iron oxides and clays. The pigment Raw Sienna is a variant of Yellow Ochre [13], discussed below. The spectrum of the film pigmented with Raw Sienna, Figure A.14, bears similarities to the film pigmented with Red Iron Oxide, largely due to common

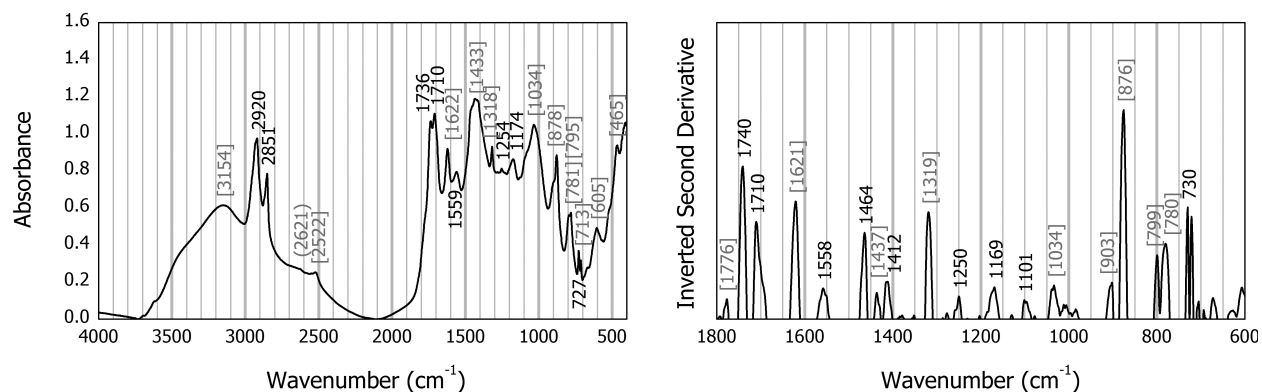


**Figure A.14.** Infrared spectrum of a 20.8-year-old oil paint pigmented with Raw Sienna (left) and its second derivative, inverted (right).

impurities. As before, the peaks at 2621 (shoulder), 2522, 878, and 713  $\text{cm}^{-1}$  are assigned to  $\text{CaCO}_3$ , which also has a very strong peak at 1433  $\text{cm}^{-1}$  affecting the baseline of the fingerprint region [5]. An additional second-derivative peak at 1776  $\text{cm}^{-1}$  is also assigned to  $\text{CaCO}_3$ . (Although van der Weerd, *et al.*, had assigned this to lactones and anhydrides [1], this scenario is less likely for these younger films. This possibility is excluded by noting that this peak is nearly absent in films that do not contain  $\text{CaCO}_3$ .) Peaks at 1622 and 1318  $\text{cm}^{-1}$  are assigned to  $\text{CaC}_2\text{O}_4$ . The peak at 781  $\text{cm}^{-1}$  may be similarly due to  $\text{CaC}_2\text{O}_4$ , but it may also be due to silica, which has a characteristic pair of peaks at 795 and 781  $\text{cm}^{-1}$ . The main silicate peak is at 1034  $\text{cm}^{-1}$ , consistent with amorphous silica, rather than at  $\sim 1080$   $\text{cm}^{-1}$  as would be expected of quartz. However, the band at 465  $\text{cm}^{-1}$  is characteristic of quartz [13]. Perhaps both amorphous and crystalline forms of silica are present.

Raw Sienna does not have a strongly characteristic IR spectrum that is separate from the combined spectra of calcium carbonate, calcium oxalate, and silica. However, the absorption at 605  $\text{cm}^{-1}$  is attributed to the pigment [13]. Second-derivative bands at 903, 524, and 469  $\text{cm}^{-1}$  are assigned to iron oxide [14]. (Iron oxide, silica, and calcium oxalate all contribute to the second-derivative band at 799  $\text{cm}^{-1}$ .) The O-H stretch at 3154  $\text{cm}^{-1}$  is also attributed to hydrated ferric oxide, and the shoulder at  $\sim 3450$   $\text{cm}^{-1}$  to hydroxyl ions in water [14].

The band at 1559  $\text{cm}^{-1}$  is assigned to metal carboxylates. Since the paint film contains several metals introduced into it via clay, the identity of the metal that forms these carboxylates cannot be ascertained without utilizing another experimental technique. However, a tentative assignment may be made. Although compositions vary extensively, metals present in highest concentrations in Raw Sienna are iron, aluminum, magnesium, and calcium [14]. The primary carboxylate peaks for the stearate soaps of these metals occur at 1573+, 1585+, 1570+, and 1550  $\text{cm}^{-1}$ , respectively [20-24]. (Metal palmitates have IR spectra that are nearly identical to those of metal stearates. Metal azelates are rarely reported in the literature, but they appear to have the  $\text{COO}^-$  asymmetric stretch located  $\sim 20$ -25  $\text{cm}^{-1}$  lower than the respective palmitates and stearates [12].) The exact location of the  $\text{COO}^-$  band depends on factors that affect the strength of the bond between the metal and the  $\text{COO}^-$  moiety, including the coordination state, e.g. di- or tristearate, and water content – as well as the electronegativity of the metal [20,22,25]. Of

these metal stearates, only calcium stearate's band is close enough to  $1559\text{ cm}^{-1}$  for a plausible correspondence. However, since calcium was present in several of the paint samples discussed earlier that contained free acids but not carboxylates, calcium is not a likely originator of this band.

On the other hand, potassium and sodium stearates both have their primary carboxylate absorption at  $1559\text{ cm}^{-1}$  [24,26]. While the actual metal content of the pigment used to manufacture the film is not known, it should be noted that potassium is normally present in Raw Sienna only in small amounts, and sodium content is lower yet or entirely absent [13,14,27]. Nonetheless, potassium and sodium are known to be highly reactive with carboxylic acids, so much so that soaps of other metals are usually synthesized in the lab using potassium or sodium carboxylates as intermediates. Therefore, it is likely that, after 20 years, potassium and any sodium that exist in the paint would be present nearly exclusively in the soap form. The band at  $1559\text{ cm}^{-1}$  is tentatively assigned to potassium and sodium carboxylates.

#### A.2.6.4. Yellow Ochre

The pigment Yellow Ochre is related to Raw Sienna, discussed above. However, the spectrum of the film pigmented with Yellow Ochre (Figure A.15) appears different on a superficial level because the peaks in the fingerprint region are less resolved, and because it has sharp O-H stretching bands at 3699, 3652 (second derivative), and  $3621\text{ cm}^{-1}$  that are characteristic of kaolinite [13,14,28]. Other bands assigned to kaolinite are the Si-O-Al stretch at  $995\text{ cm}^{-1}$  and the Al-O-H stretch at  $915\text{ cm}^{-1}$ . Quartz, which

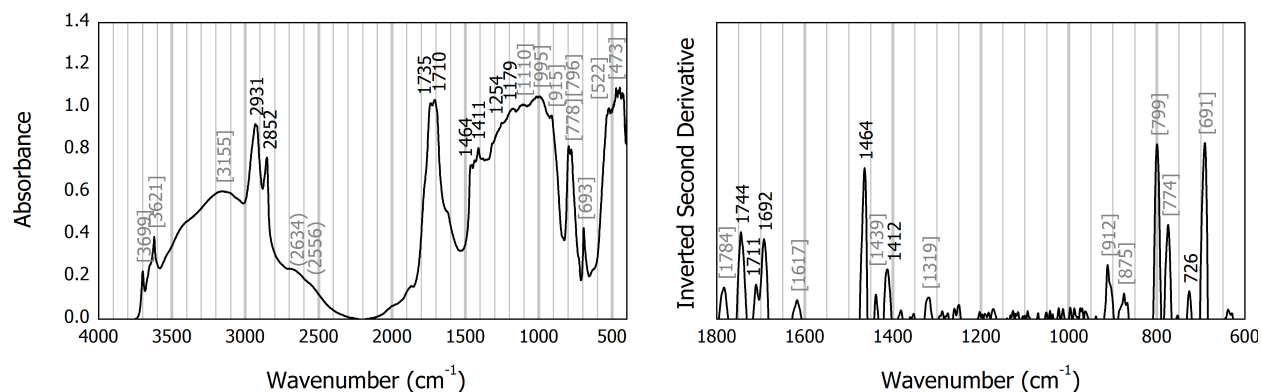


**Figure A.15.** Infrared spectrum of an 18.7-year-old oil paint pigmented with Yellow Ochre (left) and its second derivative, inverted (right).

is commonly found with kaolinite, is identified by the bands at 1110, 796, 778, and 693  $\text{cm}^{-1}$  [13,14]. The baseline distortion in the fingerprint region is probably caused by the silicate absorptions.

As with Raw Sienna, the band at 3155  $\text{cm}^{-1}$  is attributed to hydrated ferric oxide and the shoulder at  $\sim 3430 \text{ cm}^{-1}$ , to hydroxyl ions in water. The bands at 522 and 473  $\text{cm}^{-1}$  are similarly attributed to  $\text{Fe}_2\text{O}_3$ . The content of  $\text{CaCO}_3$  appears low, with respective bands identifiable only on the second derivative spectrum at 1784, 1439, and 875  $\text{cm}^{-1}$ , as well as shoulders at 2634 and 2556  $\text{cm}^{-1}$ . Consequently,  $\text{CaC}_2\text{O}_4$  bands at 1617 and 1319  $\text{cm}^{-1}$  are also distinguishable using the second derivative spectrum only.

#### A.2.6.5. Raw Umber

*Raw Umber.* The pigment Raw Umber is similar to the ochres, but it nominally contains higher levels of  $\text{MnO}_2$ . The spectrum of the film pigmented with Raw Umber, Figure A.16, superficially appears very different from Yellow Ochre because it is much better resolved. However, with the exception of quartz, which does not manifest bands on this spectrum, most of the bands that constitute the two spectra are the same.

Kaolinite is assigned to the O-H bands at 3698, 3653 (second derivative), and 3622  $\text{cm}^{-1}$ , the Si-O-Si band at 1043  $\text{cm}^{-1}$ , the Si-O-Al band at 1007  $\text{cm}^{-1}$  (second derivative), and the Al-O-H band at 919  $\text{cm}^{-1}$ .  $\text{CaCO}_3$  is assigned to the bands at 2619 (shoulder), 2525, 1795 (second derivative), 1435, 873, and 713  $\text{cm}^{-1}$ . These absorptions are fairly strong and explain the baseline distortion in the fingerprint region.  $\text{CaC}_2\text{O}_4$  is assigned to the bands at 1623, 1318, and 782  $\text{cm}^{-1}$ .

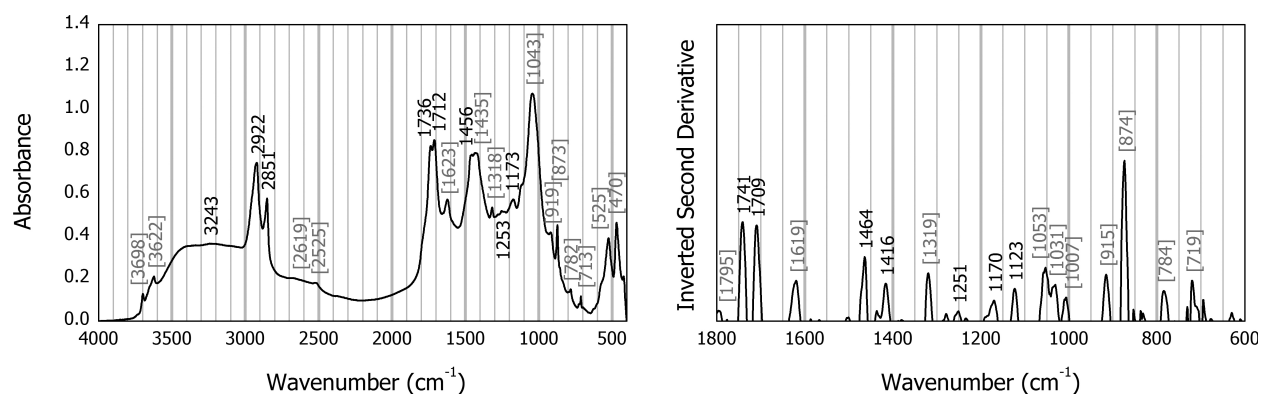


**Figure A.16.** Infrared spectrum of an 18.7-year-old oil paint pigmented with Raw Umber (left) and its second derivative, inverted (right).

$\text{Fe}_2\text{O}_3$  is assigned to bands at 525 and 470  $\text{cm}^{-1}$ . The O-H band at 3243  $\text{cm}^{-1}$  is weaker and broader than with Raw Sienna and Yellow Ochre and is assigned to acids rather than to hydrated ferric oxide.

### **A.3. Discussion**

Many spectra have been shown in this study and their absorption bands have been fully assigned. Organic and organometallic band locations for all the samples are compiled in Table A.1. Nonetheless, given the size of the collection, a discussion of every feature would be overwhelming. Instead, structures present in aged oil paints may be considered by examining the prevalences of only three functional groups: intact triglyceride esters, whose high concentration would indicate that the extent of degradation is low, and carboxylic acids and metal carboxylates, whose high concentrations would indicate that the extent of degradation is high. Unfortunately, however, in the absence of an inert internal standard, only qualitative determinations are possible [1].

The interpretations are further complicated by the strong pigment absorptions which not only coincide with some organic bands but that also distort the baseline. This last problem may be resolved by spectral subtraction when samples of pigments that were used to manufacture the original films are available. However, no such luck was had, and using substitute pigments would have been ineffective due to widespread variation in the identities and contents of IR-active impurities among artists' pigments.

Returning to the structural investigation, functional groups of interest have more than one absorption band that might be discussed. However, esters are best identified using only the carbonyl band at  $\sim 1740 \text{ cm}^{-1}$  because the C-O-C ester triplet, located between 1250-1100  $\text{cm}^{-1}$ , is often obscured by strong pigment absorptions. Carboxylic acids are best identified by the carbonyl band as well, which in acids is found at  $\sim 1710 \text{ cm}^{-1}$ , since broad O-H absorptions may be easily due to pigments, and the combination band at  $\sim 1414 \text{ cm}^{-1}$  is very weak even when it is not masked. Metal carboxylates have several bands as well, with locations that vary from pigment to pigment, but they are usually identified by the asymmetric  $\text{COO}^-$  stretch located between  $\sim 1590\text{-}1550 \text{ cm}^{-1}$  both because it is the strongest carboxylate band and because it does not usually coincide with other organic or pigment features.

**Table A.1.** Organic and organometallic IR band assignments for fresh oil paint and aged oil paint films. (Parentheses) indicate locations on the second derivative of the normal absorbance spectrum which cannot be identified otherwise, e.g. because they appear as shoulders on the normal spectrum. ~~Strikethrough~~ denotes peaks of negligible intensity. The term "masked" indicates that the presence or absence of a given organic band is indeterminate because its expected location coincides with a pigment absorption.

Attribution	0.0Y	0.0Y	12.3Y	21.0Y	11.3Y	18.8Y	20.8Y	12.2Y
	Neat Oil	Neat Oil	Neat Oil	Lead	Lead	Naples	Zinc	Zinc
	Refined	Cold Pressed	Cold Pressed	White	White	Yellow	White	White
<i>Metal Carboxylate</i>								
COO <sup>-</sup>	-	-	-	1543	1538	-	1579	1585
<i>Carboxylic acid, Hydroperoxide</i>								
C-O + O-H	1418	1418	1418	-	-	<del>1413</del>	1416	1416
C=O	-	-	1716	<del>(1707)</del>	-	<del>1709</del>	<del>(1712)</del>	<del>(1711)</del>
O-H	<del>3470</del>	<del>3471</del>	3389	-	-	3400	3407	3408
<i>Ester</i>								
C-O-C	1100	1100	1081	1093	1088	1092	1098	1097
C-O-C	1164	1164	1150	1166	1167	1175	1163	1163
C-O-C	1239	1239	1224	<del>(1235)</del>	<del>(1233)</del>	<del>1247</del>	1243	1241
C=O	1745	1745	1742	1738	1740	1733	1742	1741
<i>Alkene</i>								
C-H	723	723	722	<del>(726)</del>	<del>(726)</del>	<del>(723)</del>	masked	masked
C-H	<del>969</del>	<del>971</del>	<del>(970)</del>	970	969	-	979	976
C=C	1654	1654	1653	-	-	-	1669	1670
C-H	3010	3010	3016	-	-	-	-	-
<i>Alkane</i>								
CH <sub>3</sub>	1377	1377	1384	<del>(1398)</del>	<del>(1397)</del>	1376	1378	1377
CH <sub>2</sub> , CH <sub>3</sub>	1464	1464	1465	<del>(1466)</del>	<del>(1468)</del>	1458	<del>(1462)</del>	<del>(1462)</del>
CH <sub>2</sub>	2854	2854	2852	2852	2852	2863	2854	2854
CH <sub>2</sub>	2926	2926	2924	2924	2924	2924	2921	2925
CH <sub>3</sub>	<del>(2962)</del>	2955	2952	<del>(2959)</del>	<del>(2960)</del>	<del>(2957)</del>	<del>(2964)</del>	<del>(2962)</del>

**Table A.1.** Organic and organometallic IR band assignments for fresh oil paint and aged oil paint films (continued from the previous page).

Attribution	18.7Y Malachite	18.7Y Iron Oxide	20.8Y Raw Sienna	18.7Y Yellow Ochre	18.7Y Raw Umber	18.8Y Silica	18.8Y Barium Sulfate	18.8Y Calcium Carbonate
<i>Metal Carboxylate</i>								
COO <sup>-</sup>	(1588)	-	1559	-	-	-	-	-
<i>Carboxylic acid, Hydroperoxide</i>								
C-O + O-H	masked	1417	(1412)	1411	(1416)	1414	-	1417
C=O	(1709)	1711	1710	1710	1712	1713	1715	1716
O-H	masked	3191	masked	masked	3243	masked	3390	3397
<i>Ester</i>								
C-O-C	masked	(1096)	(1101)	masked	(1123)	1109	masked	-
C-O-C	1178	1174	1174	1179	1173	1167	masked	1186
C-O-C	-	(1249)	1254	1254	1253	(1246)	-	-
C=O	1740	1736	1736	1735	1736	1736	1736	1739
<i>Alkene</i>								
C-H	(734)	(720)	727	(726)	(719)	masked	727	(734)
C-H	(974)	-	-	-	-	971	masked	(975)
C=C	(1621)	masked	masked	masked	masked	-	-	masked
C-H	masked	-	-	-	-	-	-	-
<i>Alkane</i>								
CH <sub>3</sub>	masked	(1379)	-	-	-	1383	-	1398
CH <sub>2</sub> , CH <sub>3</sub>	(1488)	(1464)	(1464)	1464	1456	1464	1463	-
CH <sub>2</sub>	2852	2852	2851	2852	2851	2854	2852	2855
CH <sub>2</sub>	2924	2926	2920	2931	2922	2929	2927	2928
CH <sub>3</sub>	-	(2959)	(2960)	(2958)	(2960)	(2960)	(2960)	(2960)

Several of the films in the collection had lost all cohesion: the unpigmented aged film and the films containing inert and iron-based pigments. In these (and only these) films, the acid C=O at  $\sim 1710\text{ cm}^{-1}$  is distinct from the ester C=O at  $\sim 1740\text{ cm}^{-1}$ . This indicates that the concentration of carboxylic acids is high within these films, which in turn necessitates a high extent of degradation. IR data thus concurs with macroscopic observations.

The remainder of the collection has remained intact and consists of films pigmented with copper, zinc, and lead. (The film of Naples Yellow,  $\text{Pb}_3(\text{SbO}_4)_2$ , had retained some cohesion but was not fully intact. However, since its IR spectrum was poor, it will not be discussed.) For the films pigmented with Zinc White and Malachite, the acid band is much less distinct than for the incoherent films and is resolvable only using the second derivative spectrum. However, the corresponding shoulder on the normal spectrum is much stronger for Malachite than it is for Zinc White, indicating a higher prevalence of free acids. For the films pigmented with White Lead, the acid band is scarcely resolvable even using the second derivative spectrum. Therefore, the acid content is highest in the film pigmented with copper, followed by zinc, followed by lead.

One mechanism by which free acids may be consumed is a reaction with free metal ions to form metal carboxylates. Indeed, all cohesive films have in their spectra the characteristic  $\text{COO}^-$  band at  $1590\text{--}1540\text{ cm}^{-1}$ . This band is weak and partly obscured by its proximity to the strong carbonyl absorptions, so while it indicates that metal carboxylates are present, it cannot be used to gauge their prevalence. However, in art conservation, lead carboxylates are encountered with the highest frequency within paintings, followed by zinc carboxylates, followed by copper, – which suggests their likely abundances within the present set of films. Noting that this mirrors the trend in acid contents, the abundance of metal carboxylates is inferred to be the highest with White Lead, followed by Zinc White, followed by Malachite.

Finally, a curious case is presented by the film pigmented with Raw Sienna, which unambiguously contains metal carboxylates even while the other iron-based films do not. Therefore, these carboxylates must be due to a metal which was introduced into the film via a clay. Although the pigments Yellow Ochre and Raw Umber also contain clays, compositions of clays vary extensively based on geographical origin. As a consequence, it is possible that metal carboxylates are present in the Raw Sienna film but not



in others because Raw Sienna contains a somewhat atypical metal. A more thorough speculation is detailed in the results section and this structure is tentatively assigned to potassium or sodium carboxylates. However, another characterization technique must be used to conclusively identify the metal.

#### A.4. Conclusion

Infrared spectra have been presented to identify the prevalences of several functional groups within the library of naturally aged oil paint films as part of a larger structural investigation. All paints that had lost cohesion demonstrate high acid contents as a result of degradation. All paints that remained intact contain metal carboxylates. As a result, free acid contents are the lowest in White Lead paint, followed by Zinc White, followed by Malachite.

#### A.5. References

- [1] J. van der Weerd, A. van Loon, J.J. Boon. FTIR studies of the effects of pigments on the aging of oil. *Stud. Conserv.* **2005**, *50*, 3-22.
- [2] R.J. Meilunas, J.G. Bentsen, A. Steinberg. Analysis of aged paint binders by FTIR spectroscopy. *Stud. Conserv.* **1990**, *35*, 33-51.
- [3] K. Castro, M. Pérez, M.D. Rodríguez-Laso, L.A. Fernández, J.M. Madariaga. FTIR spectra database of inorganic art materials. *Anal. Chem.* **2003**, *75*, 214A-221A.
- [4] R.L. Feller. Barium Sulfate – Natural and Synthetic. In R.L. Feller (ed.), *Artists' Pigments: A Handbook of their History and Characteristics*, Volume 1. Cambridge University Press: Cambridge, 1986, 47-64.
- [5] R.J. Gettens, E.W. Fitzhugh, R.L. Feller. Calcium Carbonate Whites. In A. Roy (ed.), *Artists' Pigments: A Handbook of their History and Characteristics*, Volume 2. Oxford University Press: Oxford, 1993, 203-226.
- [6] R.J. Gettens, H. Kühn, W.T. Chase. Lead White. In A. Roy (ed.), *Artists' Pigments: A Handbook of their History and Characteristics*, Volume 2. Oxford University Press: Oxford, 1993, 67-82.
- [7] I.N.M. Wainwright, J.M. Taylor, R.D. Harley. Lead Antimonate. In R.L. Feller (ed.), *Artists' Pigments: A Handbook of their History and Characteristics*, Volume 1. Cambridge University Press: Cambridge, 1986, 219-254.
- [8] SDBSWeb: <http://riodb01.ibase.aist.go.jp/sdbs/> (National Institute of Advanced Industrial Science and Technology, Accessed Feb 22 2011).
- [9] R. Mazzeo, S. Prati, M. Quaranta, E. Joseph, E. Kendix, M. Galeotti. Attenuated total reflection micro FTIR characterization of pigment-binder interaction in reconstructed paint films. *Anal. Bioanal. Chem.* **2008**, *392*, 65-76.

- [10] L. Robinet, M.-C. Corbeil. The characterization of metal soaps. *Stud. Conserv.* **2003**, *48*, 23-40.
- [11] R.J. Gettens, E.W. Fitzhugh. Malachite and Green Verditer. In A. Roy (ed.), *Artists' Pigments: A Handbook of their History and Characteristics*, Volume 2. Oxford University Press: Oxford, 1993, 183-202.
- [12] C. Higgitt, M. Spring, D. Saunders. Pigment-medium interactions in oil paint films containing red lead or lead-tin yellow. *National Gallery Technical Bulletin* **2003**, *24*, 75-91.
- [13] D. Bikiaris, Sister Daniilia, S. Sotiropoulou, O. Katsimbiri, E. Pavlidou, A.P. Moutsatsou, Y. Chrissoulakis. Ochre-differentiation through micro-Raman and micro-FTIR spectroscopies: Application on wall paintings at Meteora and Mount Athos, Greece. *Spectrochim. Acta A* **1999**, *56*, 3-18.
- [14] C. Genestar, C. Pons. Earth pigments in painting: characterisation and differentiation by means of FTIR spectroscopy and SEM-EDS microanalysis. *Anal. Bioanal. Chem.* **2005**, *382*, 269-274.
- [15] G. van der Snickt, K. Janssens, J. Dik, W. de Nolf, F. Vanmeert, J. Jaroszewicz, M. Cotte, G. Falkenberg, L. van der Loeff. Combined use of synchrotron radiation based Micro-X-ray Fluorescence, Micro-X-ray Diffraction, Micro-X-ray Absorption Near-Edge, and Micro-Fourier Transform Infrared Spectroscopies for revealing an alternative degradation pathway of the pigment cadmium yellow in a painting by Van Gogh. *Anal. Chem.* **2012**, *84*, 10221-10228.
- [16] E. Fiorin, P.A. Vigato. Teodelinda's tales at Monza Cathedral: A physico-chemical diagnosis of the pictorial cycle. *J. Cult. Herit.* **2007**, *8*, 13-25.
- [17] J. van der Weerd, H. Brammer, J.J. Boon, R.M.A. Heeren. Fourier Transform Infrared Microscopic Imaging of an embedded paint cross-section. *Appl. Spectrosc.* **2002**, *56*, 275-283.
- [18] J.W. Salisbury, A. Wald. The role of volume scattering in reducing spectral contrast of reststrahlen bands in spectra of powdered minerals. *Icarus* **1992**, *96*, 121-128.
- [19] M. Fabbri, M. Picollo, S. Porcinai, M. Bacci. Mid-Infrared Fiber-Optics Reflectance Spectroscopy: A noninvasive technique for remote analysis of painted layers. Part I: Technical setup. *Appl. Spectrosc.* **2001**, *55*, 420-427.
- [20] H.B. Abrahamson, H.C. Lukaski. Synthesis and characterization of iron stearate compounds. *J. Inorg. Biochem.* **1994**, *54*, 115-130.
- [21] T.A. Egerton, N.J. Everall, I.R. Tooley. Characterization of TiO<sub>2</sub> nanoparticles surface modified with aluminum stearate. *Langmuir* **2005**, *21*, 3172-3178.
- [22] K.P. Rao, G. Chawla, A.M. Kaushal, A.K. Bansal. Impact of solid-state properties on lubrication efficacy of magnesium stearate. *Pharm. Dev. Technol.* **2005**, *10*, 423-437.
- [23] Y. Lu, J.D. Miller. Carbonyl stretching vibrations of spontaneously adsorbed and LB-transferred calcium carboxylates as determined by FTIR Internal Reflection Spectroscopy. *J. Colloid Interf. Sci.* **2002**, *256*, 41-52.
- [24] H.A. Capelle, L.G. Britcher, G.E. Morris. Sodium stearate adsorption onto titania pigment. *J. Colloid Interf. Sci.* **2003**, *268*, 293-300.
- [25] T.A. Ibidapo. Polymeric structure in some molten groups IIA and IIB metal dicarboxylates. *Macromolecules* **1989**, *22*, 1480-1484.
- [26] M. Gasgnier. IR spectra of some potassium carboxylates. *J. Mater. Sci. Lett.* **2001**, *20*, 1259-1262.

- [27] C.G. Juliá, C.P. Bonafé. The use of natural earths in picture: study and differentiation by thermal analysis. *Thermochim. Acta* **2004**, *413*, 185-192.
- [28] C.T. Johnston, S.F. Agnew, D.L. Bish. Polarized single-crystal Fourier-Transform Infrared Microscopy of Ouray dickite and Keokuk kaolinite. *Clay. Clay Miner.* **1990**, *38*, 573-583.

## APPENDIX B. THERMAL ANALYSIS OF METAL SOAPS

### B.1. Synthesis of Metal Soaps

Different synthetic procedures were used to produce different metal soaps, as discussed in the main text. These procedures are explained further in this section, and DSC traces are included to bring transparency to the decision-making process behind the choice of method.

In the first method (ambient temperature, no intermediate), two solutions were prepared, one containing a metal salt and the other, a fatty acid, and the two solutions were mixed. In this process, a metal soap may form by a substitution reaction such as



where  $n=3$  for Fe(III) and  $n=2$  for Pb(II), Zn(II), and Cu(II), although for copper, the reaction would be slightly different with respect to the  $\text{SO}_4^{2-}$  anion. Under the mild synthetic conditions used, the reaction was unlikely to proceed to completion, so the product was expected to contain a mixture of mono-, di-, and in the case of iron, tri-substituted metals, with the bulk of the product being monosubstituted. Or, the reaction may not have occurred to any appreciable extent at all. To determine whether or not it did, the DSC trace of the product was compared to the trace of the starting acid, and if the traces were sufficiently similar, an alternate synthesis was performed.

In the second method (ambient temperature), the reaction was carried out via a sodium soap intermediate because sodium was known to be more reactive with fatty acids than the metals of interest. To prepare the sodium soap, a slurry of the fatty acid was titrated with NaOH to an approximately neutral endpoint as follows:



Only azelate soaps were able to form in this manner. Palmitate and stearate slurries did not react with NaOH, even when the slurries were prepared with the aid of sonication. This is unsurprising given the difference in chain lengths between azelaic ( $\text{C}_9$ ) and palmitic/stearic acids ( $\text{C}_{16}$  and  $\text{C}_{18}$ , respectively).

Azelate soaps of the metals of interest were prepared by mixing the sodium soap solution with a solution of the metal salt, as before, in a substitution reaction:



Since azelaic acid is a diacid, one mole of R-COOH in an equation such as B.2 corresponds to 1/2 mole of the acid. DSC of the product was used to confirm that the sodium soap had been consumed.

Since palmitic and stearic acids were not reactive with sodium in the solid state, a third method was used to prepare palmitate and stearate soaps, wherein the acid was melted and the reaction with sodium was conducted at 70-80°C:



As detailed further in the main text, this was followed by adding a solution of the desired metal salt in accord with equation B.3. DSC was used analogously to method 2.

An additional check for metal impurities was performed by comparing thermograms of metal soaps to those of the starting metal salts (Figure B.1). Basic copper carbonate exhibited a distinct peak at 243°C. This peak appears to correspond to the DSC peak reported in the literature as occurring between 280-285°C when scanning at a rate of 5°C/min [1]. That peak was hypothesized to correspond to either dehydration or decarboxylation. Thermograms of the other starting salts were featureless, so they could not have been used to similarly check for the presence of metal impurities.

Azelate soaps were all able to be synthesized at ambient conditions (Figure B.2). Only lead azelate was successfully synthesized using the one-step method. When attempting the one-step method in the syntheses of zinc and iron azelates, no precipitates could be obtained. In the case of copper, a precipitate was collected using the one-step method, but DSC suggested that it was only a mixture of azelaic acid and basic copper carbonate (and TGA confirmed), so the two-step method was used instead. Although the two-step method failed similarly when using copper carbonate, a convincing precipitate was obtained when copper sulfate was used as a starting reagent. DSC of the resulting copper azelate has a peak at 80°C which indicates that it still has an impurity of azelaic acid, but it also has distinct new

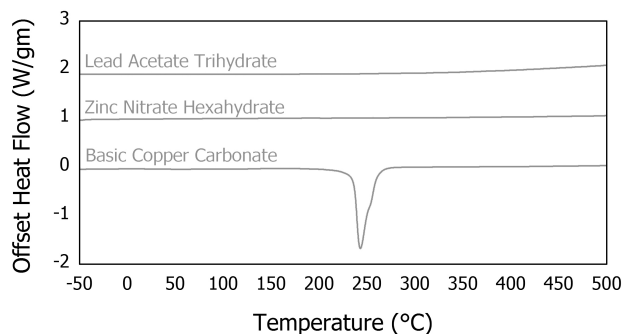


**Figure B.1.** DSC thermograms of metal salts that were used as precursors in the synthesis of metal soaps.

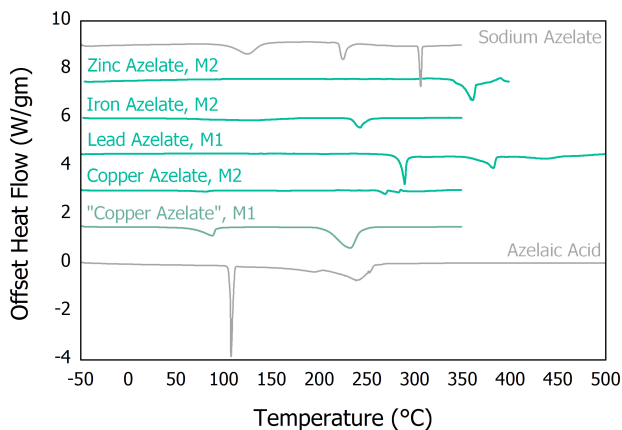


**Figure B.2.** DSC thermograms of azelate soaps and their precursors. Method of synthesis is indicated as "M1" or "M2". Unsuccessful syntheses were identified using traces shown in grey-teal.

features, indicating that a reaction had taken place. In this and other cases when impurities did not interfere with analyses, an alternate synthetic method was not sought.

Lead and zinc palmitates were able to be synthesized using the one-step process (Figure B.3). However, in the cases of copper and iron, the precipitates obtained using the one-step process were in large part the originating acid. Syntheses of copper and iron palmitates using method 3 (high temperature, sodium soap intermediate) yielded acceptable results. In the case of stearate soaps, only

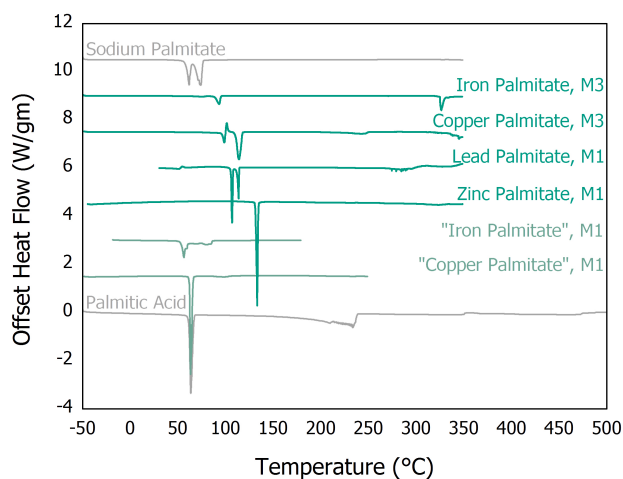


**Figure B.3.** DSC thermograms of palmitate soaps and their precursors.

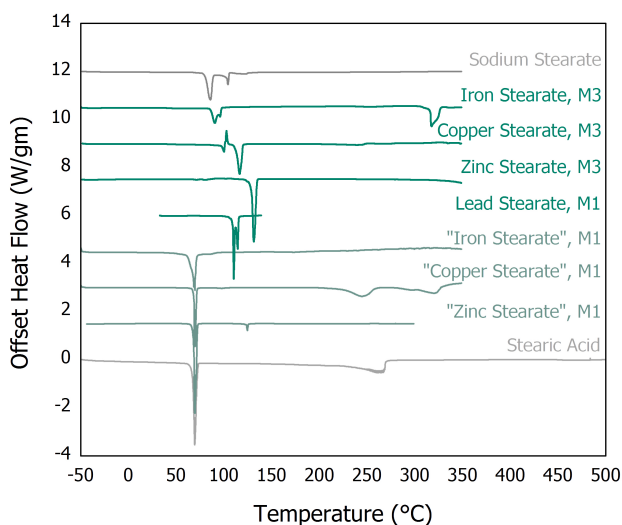


**Figure B.4.** DSC thermograms of stearate soaps and their precursors.

lead stearate was able to be synthesized using the one-step process, so method 3 was used in the remainder of the syntheses (Figure B.4).

## B.2. Identification of Degradation Temperatures

DSC thermograms identify thermodynamic processes, summarized in Table B. 1, which may arise from various physical or chemical changes within a material. Some of these, such as melting, support the notion of thermotropic liquid crystals and are relevant to the present investigation. Others, such as sample decomposition, complicate DSC results without furthering an understanding. Therefore, to deconvolute degradation events from other processes that may manifest on DSC thermograms, thermogravimetric analysis was performed to identify temperatures of decomposition steps (Figure B.5).

For each metal, monovalent palmitate and stearate soaps decomposed similarly to one another and differently from the corresponding divalent azelate soap. Comparison of derivative plots shows that stearate soaps decomposed in sharper steps than the respective palmitates. For some metals, e.g. lead, this was likely the cause for the discrepancy between its palmitate and stearate derivative (DTG) traces, wherein the stearate soap to had one apparent DTG peak while the palmitate had two, or wherein the the stearate peaks were much less resolved. Had decomposition behavior been the primary interest of this investigation, this ambiguity would likely be cleared by utilizing a slower heating rate during testing. However, given the limited purpose of this characterization, such a change was not deemed necessary.

TGA plots for three of the twelve soaps are available in the literature – copper palmitate [2], zinc stearate [3], and iron stearate [4]. All are consistent with the present results. Degradation events are summarized in Table B.2. In addition, sodium azelate was analyzed by TGA because an impurity of

**Table B.1.** Temperatures (°C) at which metal soaps and starting acids exhibit endotherms or exotherms in their DSC thermograms. *Italics* denote peaks whose irregular shape suggests sample degradation. ~~Strikethrough~~ indicates peaks that are due to impurities of the starting reagents.

	Azelate	Palmitate	Stearate
Acid	107, 197, 239	64, 233	69, 264
Pb soap	289, 382, 467	107, 113, 274-289	110, 114
Zn soap	360	133	131
Cu soap	<del>80</del> , 269, 283, 302	99, 101, 114	100, 103, 116
Fe soap	243	93, 326	90, 96, 317

**Table B.2.** Temperatures (°C) at which metal soaps exhibit peaks in their DTG plots. *Italics* denote peaks that are especially weak. The symbol ~ indicates weight loss events that are too ambiguous for meaningful identification from the present data.

	Azelate	Palmitate	Stearate
Pb	286, 322, 391, 467	333, 361	366
Zn	332, 387, 472	~, 318, 421	~, 349, 444
Cu	166, 245, 278, 301, 335	265, 307	270, 315
Fe	251, ~, 370, 382, 450	73, 269, 315, 442	277, 326, 340

sodium azelate was suspected in iron azelate based on DSC data. However, the DTG plot of sodium azelate had a sharp peak at 131°C (due to a weight loss of 6.5%), a major decomposition event above 450°C, and minor weight loss at 329°C (data not shown), which eliminated that possibility.

For copper azelate, the small degradation peak at 245°C is due to degradation of basic copper carbonate (Figure B.1). Although an analysis of decomposition products was not performed, the complexity of degradation seen in iron soaps may be caused by the loss of tightly-bound waters of hydration, which could occur far above the usual 100°C.

The assembly of Table B. 2 now allows to identify degradation processes that are observable by DSC in order to disregard them from further consideration as potential liquid crystalline phase transitions. Table B.3 is thus prepared by comparing Table B.1 against Table B.2 and against TGA plots of azelaic, palmitic, and stearic acids that have been reported in literature [5]. TGA confirms degradation as responsible for all peaks that were suspected as such based on their shape, and it also identifies additional degradation events that would otherwise have been considered potential phase changes.

**Table B.3.** Temperatures (°C) at which metal soaps and starting acids exhibit endotherms or exotherms in their DSC thermograms. Numbers in *italics* indicate peaks whose shape suggests decomposition. Numbers in (parentheses) indicate peaks that correspond to decompositions identified by TGA. ~~Strikethrough~~ denotes peaks that are due to impurities of the starting reagents.

	Azelate	Palmitate	Stearate
Acid	107, 197, (239)	64, (233)	69, (264)
Pb soap	(289), (382), (467)	107, 113, (274-289)	110, 114
Zn soap	360	133	131
Cu soap	80, (269), (283), (302)	99, 101, 114	100, 103, 116
Fe soap	(243)	93, (326)	90, 96, (317)



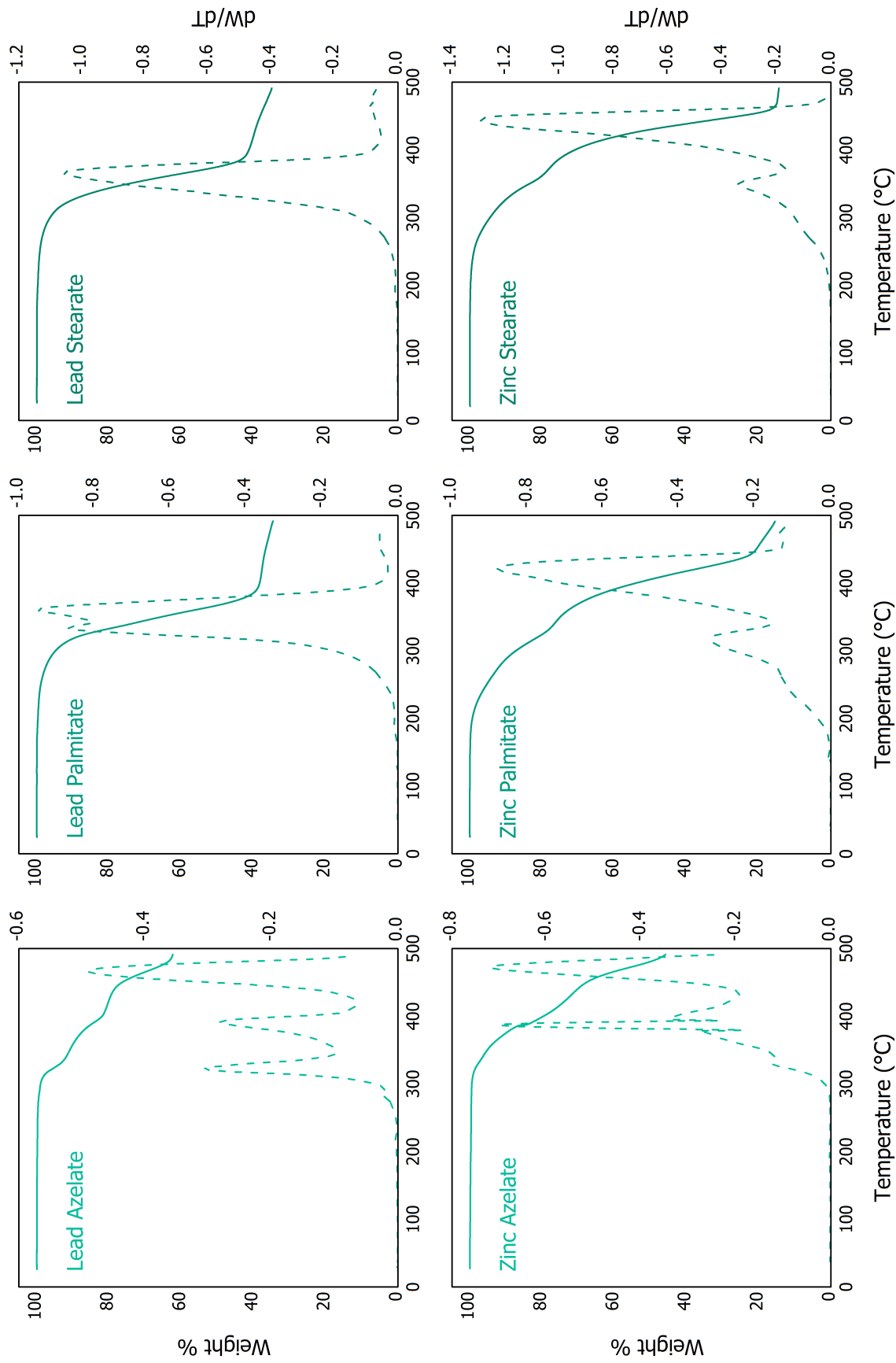


**Figure B.5.** TG plots of synthesized metal soaps. Dashed lines denote derivative (DTG) plots.

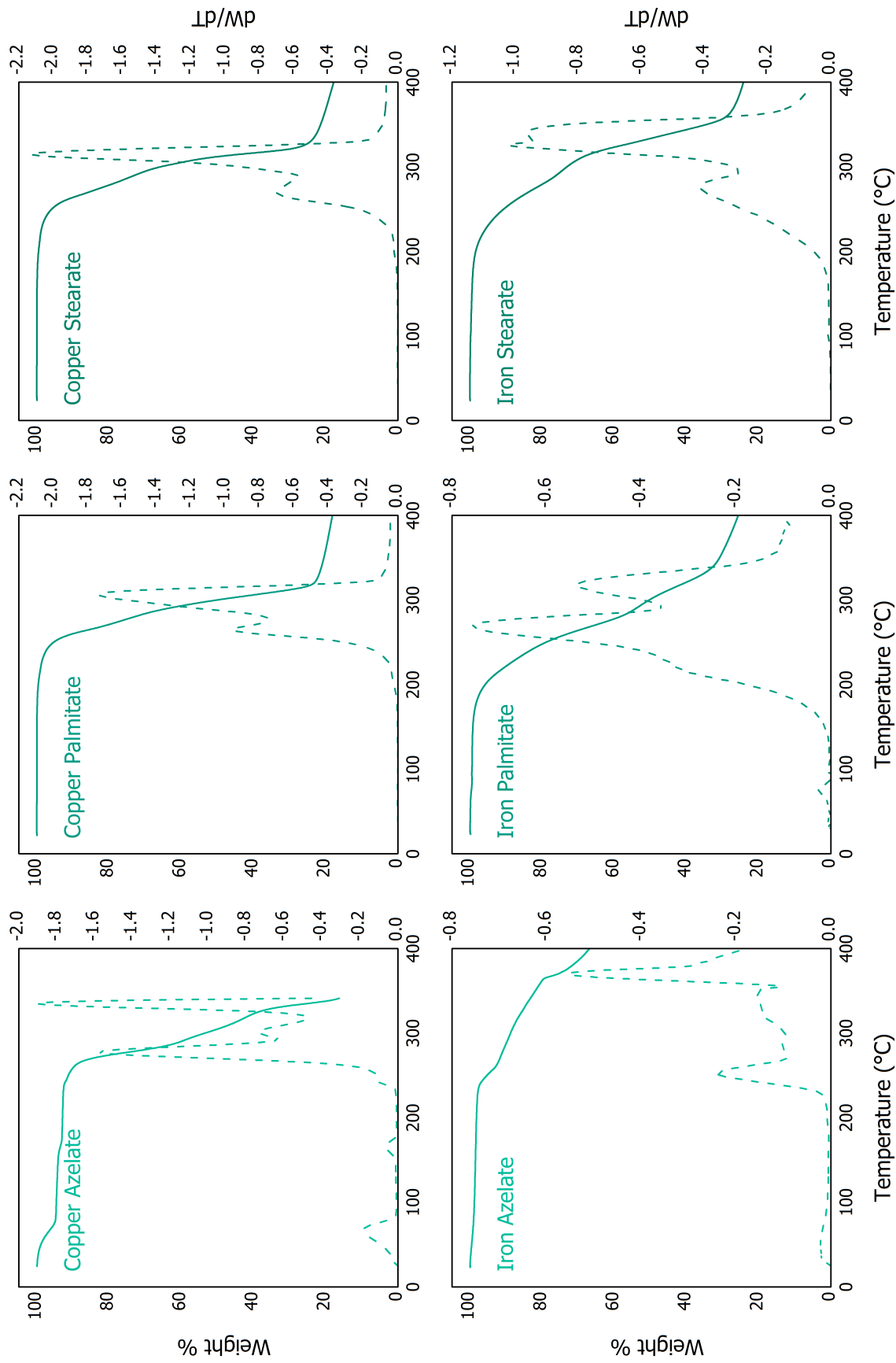


**Figure B.5.** TG plots of synthesized metal soaps (continued from previous page).

All the palmitate and stearate soaps studied undergo thermodynamic processes other than simple degradation. However, the conclusion that these DSC peaks reflect phase transitions is, so far, only tentative. For conclusive determination of the type of process responsible for the peaks, methods other than DSC must be used. Unfortunately, azelate soaps exhibit few DSC features that cannot be explained as degradation and that might be similarly due to thermotropic phase transitions.

### B.3. Identification of Phase Transitions

#### B.3.1. Lead Soaps

Lead palmitate and stearate exhibit sharp pairs of DSC peaks at 101/114°C and 103/116°C (Figure B.6). These values are nearly identical to 100/111°C for lead palmitate and 108/114°C for lead stearate reported in one study [6], and are consistent with 108/114°C and 109/115°C reported in a later study [7]. On the basis of polarizing microscopy and X-ray diffraction, these transitions had been assigned to crystal polymorphism at the lower temperature, and melting to an isotropic liquid at the upper temperature. The intermediate crystal structure was assumed to be similar to a smectic phase that develops in lead soaps of short-chain monovalent fatty acids.

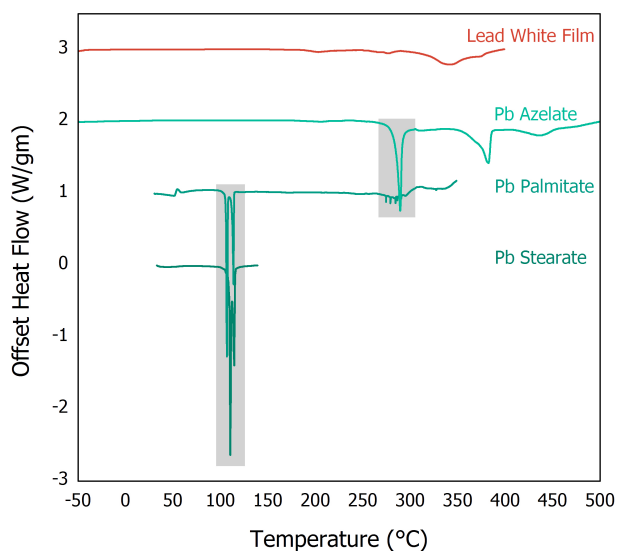


**Figure B.6.** DSC thermograms of lead soaps and the corresponding oil paint film. Grey boxes highlight soap peaks that are assigned to phase transitions.

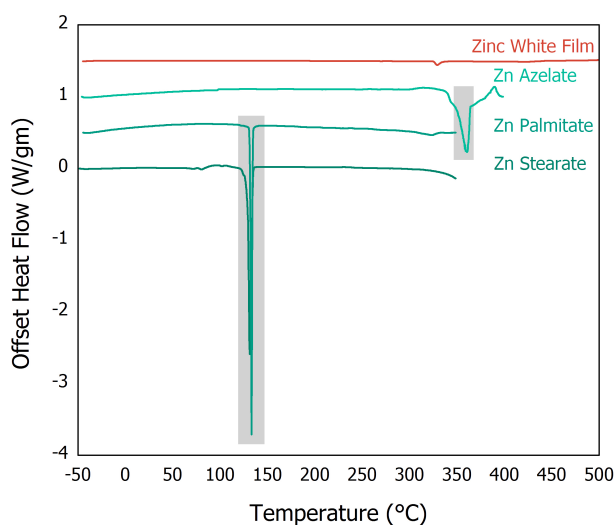


**Figure B.7.** DSC thermograms of zinc soaps and the corresponding oil paint film.

Peaks exhibited by lead azelate all correspond to sample decompositions. However, the TGA weight loss corresponding to the first peak is negligible at 0.65 wt%. Since the peak's asymmetrical shape suggests melting, and since lead azelate is known to form crystals at ambient conditions [8], this peak is tentatively assigned to melting.

### **B.3.2. Zinc Soaps**

DSC analyses of zinc palmitate and stearate are available in the literature [9]. The reported peaks, seen presently at 133°C for palmitate and 131°C for stearate (Figure B.7), are nearly identical to the literature report of 134°C and 130°C, respectively. The same study used polarizing microscopy to assign the transition to simple melting, reporting that no mesophases were observed. A consistent result for zinc stearate was reported in a later study [3], wherein the DSC endotherm was located at 125°C and the optical transition was observed at 120°C. The small discrepancy in results is consistent with impurity in the synthesized soap.

No literature studies of zinc azelate's thermal behavior have been located so the transition at 360°C cannot be conclusively assigned. However, it appears to be composed of two overlapping peaks, one of which is sharp and consistent with melting, while the other is broad and may be due to a slower process such as decomposition. Indeed, decomposition was observed at 387°C on DTG plots corresponding to a weight loss of ~20%.

### **B.3.3. Copper Soaps**

Liquid crystalline behavior of copper palmitate and stearate had been studied by other investigators [10]. The unusual sets of DSC peaks between 90-120°C (Figure B.8) were also observed. The first endotherm and the consequent exotherm were found by that study to be dependent on the thermal history of the sample and were not investigated in detail. The second endotherm was reported at 116°C for both palmitate and stearate, consistent with the present values of 114°C and 116°C, respectively. It was identified as a transformation from a crystalline phase to a columnar mesophase on the basis of polarizing microscopy, and this assignment was confirmed by X-ray diffraction.

The transition from the columnar mesophase to an isotropic liquid has been reported in copper palmitate and stearate as occurring above 200°C [10]. However, the exact melting point has been

difficult to identify due to sample decomposition. For example, one early study assigned the melting point to 225-230°C [11], while another reported it at 250-252°C [12]. Therefore, melting may be the source of the DSC peaks occurring at 243°C and 241°C in copper palmitate and stearate, respectively, with the breadth of the peaks and the subsequent calorimetric features being caused by sample decomposition. Alternately, these peaks may be due simply to decomposition of the pigment.

No literature studies of copper azelate have been located. However, copper azelate does not seem to experience phase transitions other than decomposition within the current temperature range. Given the weakness of DSC features exhibited by copper azelate, any copper azelate present in the paint films is not likely to be detectable by DSC.

### B.3.4. Iron Soaps

DSC thermograms of iron stearates have been recently reported in the literature [4]. Only a single peak was reported, instead of the double peak obtained in the present study (Figure B.9). The reported endotherms were considerably weaker and broader than the current results, owing at least in part to the faster scan rate used in the literature study. Therefore, the literature is consistent with the present data. However, no phase assignment was made.

A much earlier study examined iron(III) palmitate and stearate by DSC and X-ray diffraction [13, 14]. X-ray data suggested that the soaps occurred in a liquid crystalline state at ambient conditions, although no conclusive determination was made. DSC endotherms were reported at 101°C in both iron

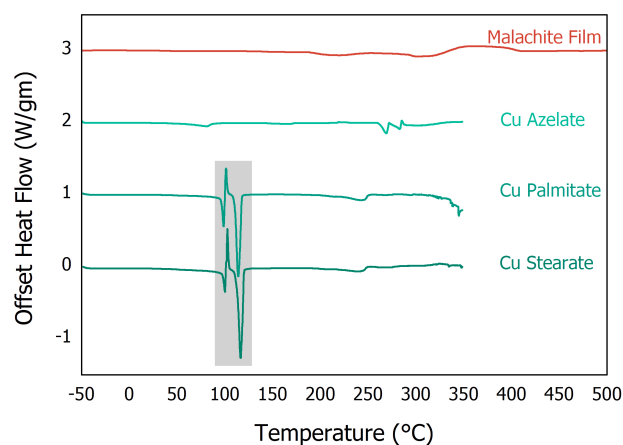


**Figure B.8.** DSC thermograms of lead soaps and the corresponding oil paint film.

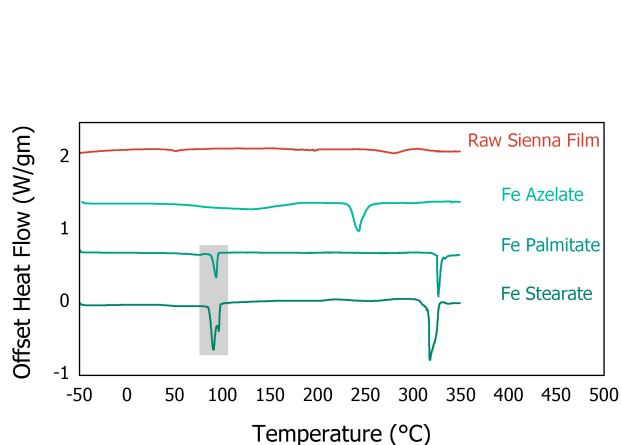


**Figure B.9.** DSC thermograms of iron soaps and one of the corresponding oil paint film.

palmitate and stearate. This is higher than the present endotherms at 93° and 90/96°C, and the difference is too high to be attributed to a slower scan rate, 1.5°C/min vs. 3°C/min used here. Therefore, it is possible that a slightly different soap or mixture of soaps was synthesized in the present study than in the literature, e.g. with two fatty acid moieties per iron atom rather than the idealized three.

No literature studies of iron azelate have been located. The only distinct peak on iron azelate's thermogram is due to sample decomposition – most likely, loss of hydrates. The broad weak endotherm between 60-180°C may be caused by water loss as well, since a small weight loss is observed below 100°C on DTG. This suggests that a presence of iron azelates in oil paint films may not be observable by DSC, since soaps found in the films are less likely to be hydrated than the synthesized soaps.

### **B.3.5. Summary**

All the palmitate and stearate soaps in this study exhibit DSC features that cannot be explained as simple degradations. Literature was located to assign phase transitions to most of these features. Zinc palmitate and stearate melt from a crystal to an isotropic liquid. Lead palmitate and stearate undergo two transitions in the studied range, from a crystal to a different crystal to an isotropic liquid. Copper palmitate and stearate transition from a crystal to a columnar mesophase to an isotropic liquid. The transitions in iron palmitate and stearate have been previously observed but were not assigned. It was assumed that they exist in a liquid crystalline phase at ambient conditions and that the DSC endotherm is a transition to an isotropic liquid.

DSC traces of azelate soaps are less characteristic than the palmitates and the stearates. For copper and iron azelates, all features are assignable as sample degradations. However, zinc and lead azelates exhibited endotherms which are consistent with melting points, although no literature was located to conclusively assign these transitions.

### **B.4. Correspondence Between Metal Soaps and Paint Films**

None of the films studied show evidence of palmitate or stearate soaps on their DSC thermograms. However, films pigmented with Zinc or Lead White have DSC features that are comparable to features of the corresponding azelates (Figures B.6 and B.7). In both cases, the corresponding

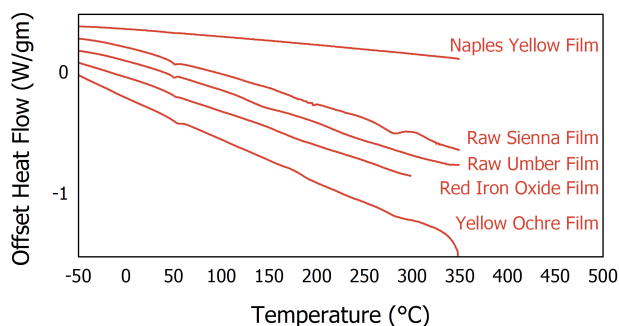


**Figure B.10.** DSC thermograms of soft oil paint films. No baseline correction was performed so as not to create procedural artifacts in the weak features.

endotherm appears at a lower temperature in the film than in the azelate soap. This is consistent with expectations, as impurities in metal soaps increase the liquid-like character of the resulting soap [15], and the soaps that might form within the oil paint films would be far from pure.

Films pigmented with Malachite or Raw Sienna have weak DSC features, but they do not appear to correspond to features of the respective azelate soaps (Figures B.8 and B.9). The only endotherm in the Malachite paint (220°C) that occurs earlier than the set of copper azelate peaks (269-300°C) is more likely due to the decomposition of the basic copper carbonate pigment. Further, when a heat/cool/heat routine was used with the Malachite film (not shown), the cooling stage was featureless, and no features remained on the second heat. Therefore, it is not surprising that none of the soap standards match the features of the Malachite film.

With exception of Raw Sienna, films pigmented with iron have no strong DSC features (Figure B.10). However, thermograms of all four films have a weak endotherm at 50-52°C. This feature is considerably weaker in the thermogram of the film pigmented with Naples Yellow,  $Pb_3(SbO_4)_2$ , which suggests that it might be due to the presence of  $Fe_2O_3$  in the films. None of the synthesized metal soaps have features in that region. However, palmitic and stearic acids have a sharp peak that is only slightly higher, at 64°C for palmitic acid and 69°C for stearic acid. Therefore, while a conclusive assignment cannot be made, this peak suggests the presence of free fatty acids in the oil.

## B.5. References

- [1] S.A.A. Mansour. Thermoanalytical investigations of decomposition course of copper oxysalts. I. Basic copper carbonate. *J. Therm. Anal.* **1994**, *42*, 1251-1263.

- [2] I. Bonaduce, L. Carlyle, M.P. Colombini, C. Duce, C. Ferrari, E. Ribechini, P. Selleri, M.R. Tiné. New insights into the ageing of linseed oil paint binder: a qualitative and quantitative analytical study. *PLoS One* **2012**, *7*, e49333.
- [3] M. Gönen, D. Balköse, F. İnal, S. Ülkü. Zinc stearate production by precipitation and fusion processes. *Ind. Eng. Chem. Res.* **2005**, *44*, 1627-1633.
- [4] P.K. Roy, P. Surekha, R. Raman, C. Rajagopal. Investigating the role of metal oxidation state on the degradation behaviour of LDPE. *Polym. Degrad. Stabil.* **2009**, *94*, 1033-1039.
- [5] M.R. Schilling, D.M. Carson, H.P. Khanjian. Gas chromatographic determination of the fatty acid and glycerol content of lipids. IV. Evaporation of fatty acids and the formation of ghost images by framed oil paintings. In J. Brigland, J. Brown (eds.), *ICOM Committee for Conservation, Preprints of the 12<sup>th</sup> Triennial Meeting*, Lyon, 29 August-3 September 1999. James & James: London, 1999, 1:242-247.
- [6] S.O. Adeosun, S.J. Sime. Properties of molten carboxylates part 4: A quantitative differential thermal analysis study of melting and mesophase formation in some lead(II) carboxylates. *Thermochim. Acta* **1976**, *17*, 351-359.
- [7] H.A. Ellis. Thermotropic phase transitions in some lead(II) carboxylates. *Mol. Cryst. Liq. Cryst.* **1986**, *139*, 281-290.
- [8] M.J. Plater, B. De Silva, T. Gelbrich, M.B. Hursthouse, C.L. Higgitt, D.R. Saunders. The characterization of lead fatty acid soaps in 'protrusions' in aged traditional paint. *Polyhedron* **2003**, *23*, 3171-3179.
- [9] I. Konkoly-Thege, I. Ruff, S.O. Adeosun, S.J. Sime. Properties of molten carboxylates part 6. A quantitative differential thermal analysis study of phase transitions in some zinc and cadmium carboxylates. *Thermochim. Acta* **1978**, *24*, 89-96.
- [10] H. Abied, D. Guillon, A. Skoulios, P. Weber, A.M. Giroud-godquin, J.C. Marchon. Investigation of the structures of the crystalline and columnar phases of linear chain copper(II) alkanoates. *Liq. Cryst.* **1987**, *2*, 296-279.
- [11] M. Takekoshi, N. Watanabe, B. Tamamushi. Copper stearate as a thermotropic liquid crystal. *Colloid Polym. Sci.* **1978**, *256*, 588-590.
- [12] R.F. Grant. Proton magnetic resonance absorption in copper(II) stearate. *Can. J. Chem.* **1964**, *42*, 951-953.
- [13] R.D. Vold, G.S. Hattiangdi. Characterization of heavy metal soaps by X-ray diffraction. *Ind. Eng. Chem.* **1949**, *41*, 2311-2320.
- [14] G.S. Hattiangdi, M.J. Vold, R.D. Vold. Differential thermal analysis of metal soaps. *Ind. Eng. Chem.* **1949**, *41*, 2320-2324.
- [15] T.J.R. Cyr, W.R. Janzen, B.A. Dunell. Effect of thermal history and impurities on phase transitions in long-chain fatty acid systems. In R.S. Porter, J.S. Johnson (eds.), *Ordered Fluids and Liquid Crystals*. American Chemical Society: Washington, D.C., 1967, 13-25.



## APPENDIX C. THERMAL ANALYSIS OF PAINT FILMS

### C.1. Introduction

This appendix contains DMA and DSC data that are omitted from the main text for clarity.

### C.2. Differential Scanning Calorimetry

DSC thermograms are shown in Figure C.1. The y-axes are greatly magnified. Although many details appear, none of them resemble a step change which could indicate a  $T_g$ . Note that the films shown on the right in Figure C.1 were heated starting at  $-50^{\circ}\text{C}$  while those on the left were heated from  $-100^{\circ}\text{C}$ . This is the reason a low-temperature artifact appears on the thermograms that are on the right in Figure C.1.

### C.3. Dynamic Mechanical Thermal Analysis

DMA data are shown in Figures C.2-C.4. DMA data were collected for each of the intact films on two occasions. The two sets of tests were performed approximately a year apart, so separate datasets are identified in Figures C.2-C.4 by the age of the film during testing. The first time, a scan was

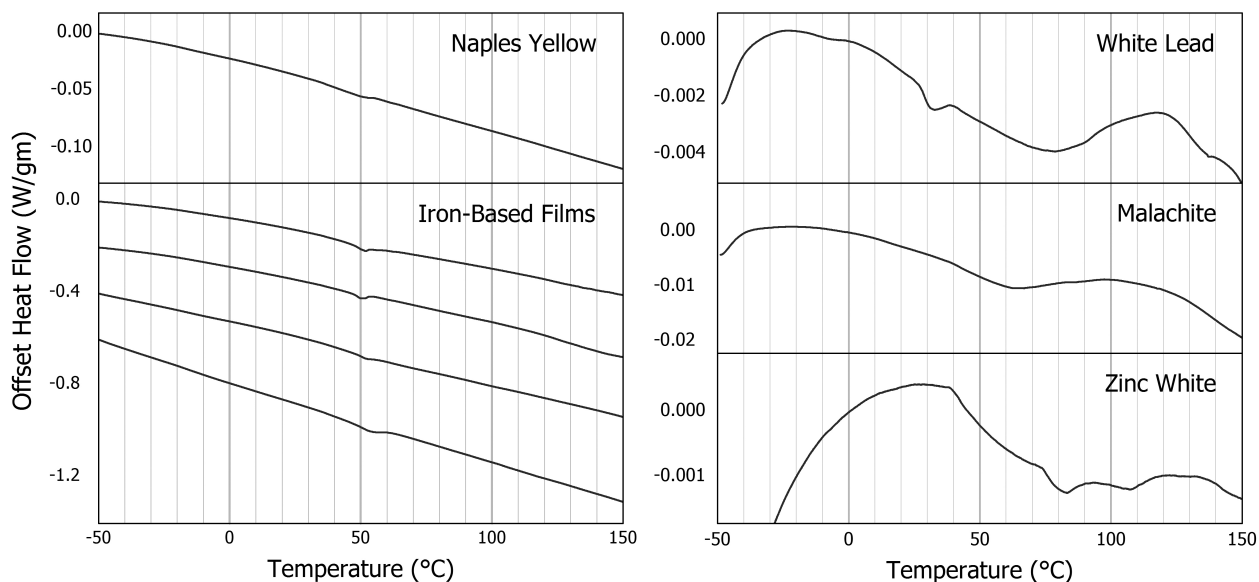


**Figure C.1.** Detail of DSC thermograms of aged oil paint films. Iron-based pigments are as follows, top to bottom: Raw Sienna, Raw Umber, Iron Oxide, Yellow Ochre. Films pigmented with White Lead and Zinc White are the younger pair from the set.

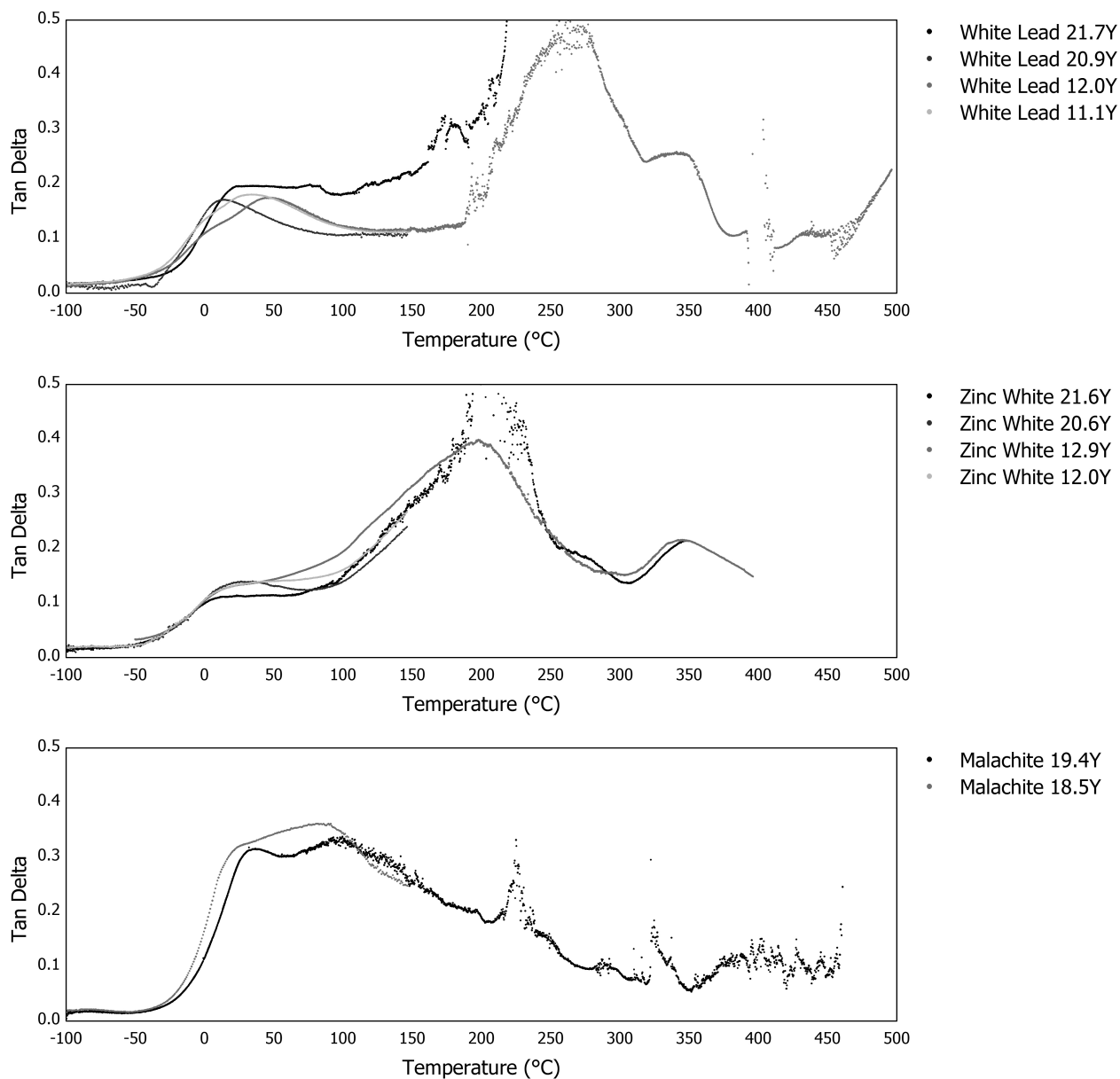


**Figure C.2.** Tan  $\delta$  plots of aged oil paint films pigmented with White Lead, Zinc White, and Malachite.

performed from -100°C to 150°C. The second time, the upper temperature limit was raised to 500°C. Most of the films had ruptured before reaching this upper limit. In addition, during the second set of tests, the older film pigmented with Zinc White fractured twice while equilibrating to -100°C, so to avoid another fracture, the lower temperature limit for that film was set to -50°C.

Since the library of paint films contained two films pigmented with White Lead and two films of Zinc White, each prepared at a different time, this resulted in four traces for each White Lead and Zinc

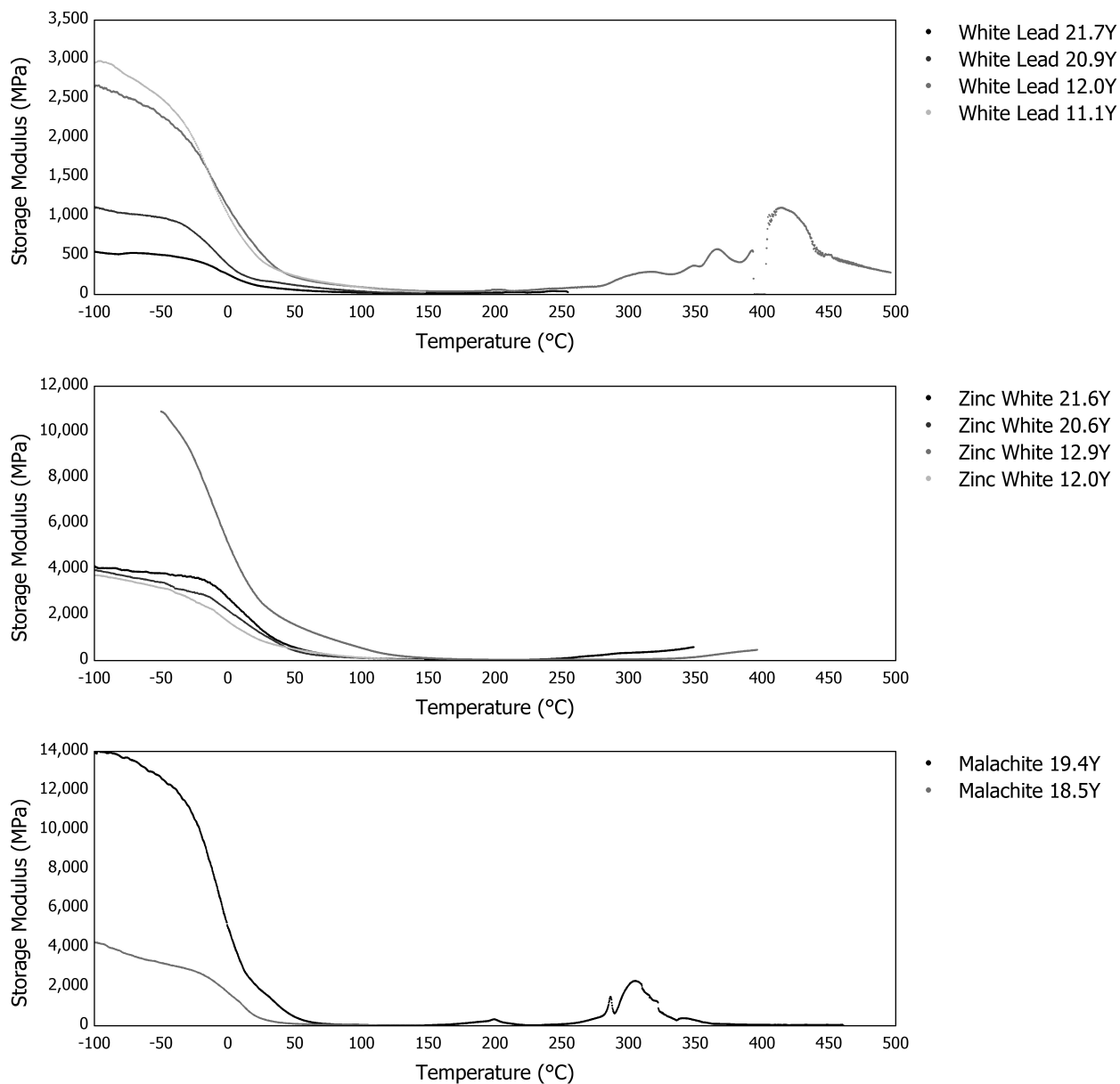


**Figure C.3.** Storage modulus plots of aged oil paint films pigmented with White Lead, Zinc White, and Malachite.

White, and two traces for the one film pigmented with Malachite. Although replicates for any given pigment are similar qualitatively, they are very different quantitatively. This is especially true for values of the storage modulus at low temperatures. However, there was insufficient sample for additional testing that could have gauged the extent of this variation and excluded outliers which may have been caused by sample damage during loading, especially for the Zinc White films which were extremely brittle.

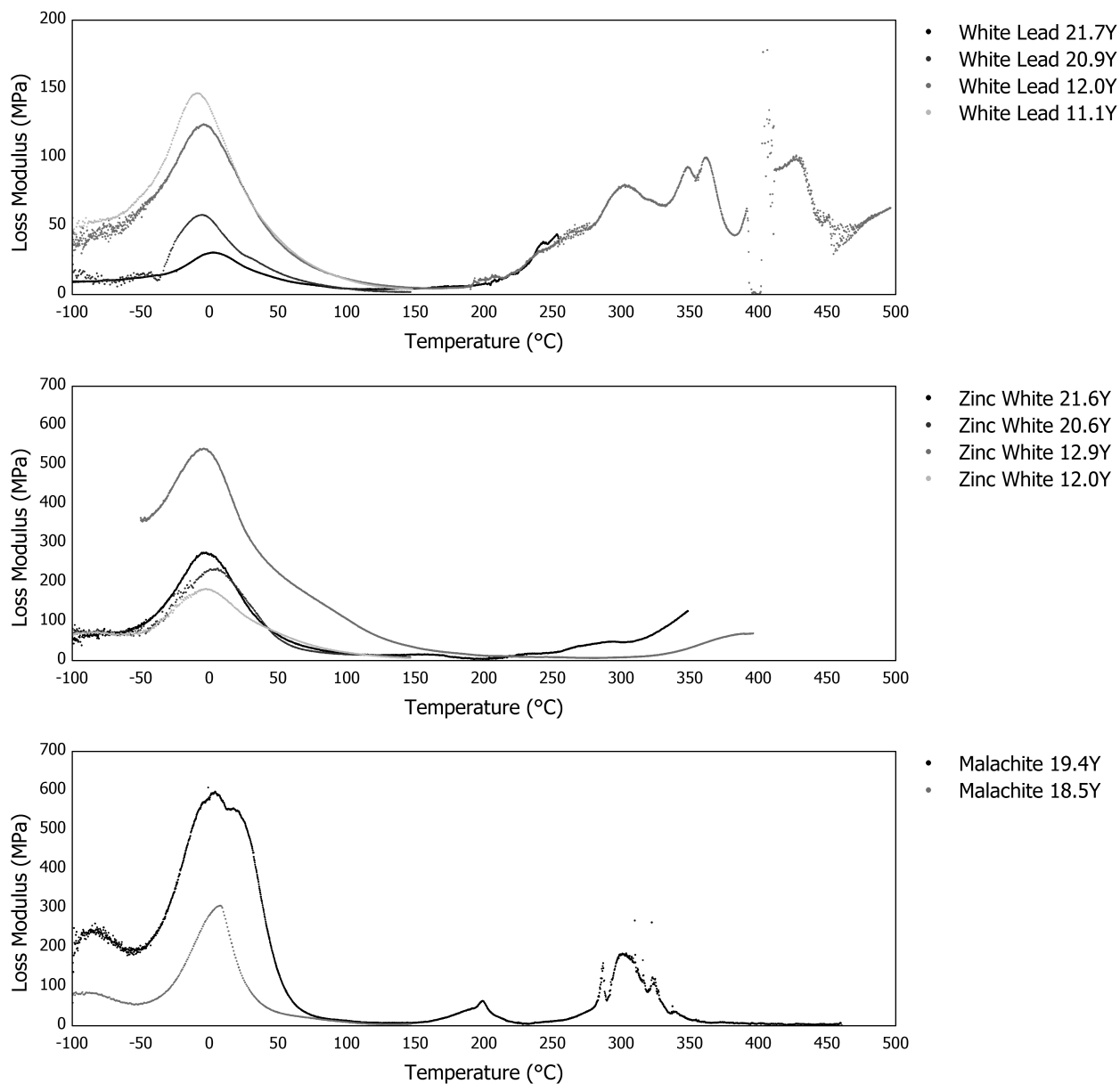


**Figure C.4.** Loss modulus plots of aged oil paint films pigmented with White Lead, Zinc White, and Malachite.

Crosslink densities were estimated using the storage modulus,  $E'$ , in what appears to be the rubbery plateau region of the storage modulus plots. Since this is the first such study, the applicability of the rubber elasticity theory to the present set of films is not known – and since this calculation of crosslink density was not this study’s primary goal, the validity of this calculation was not explored. Further, as discussed above, storage modulus values that are used in this calculation can be only

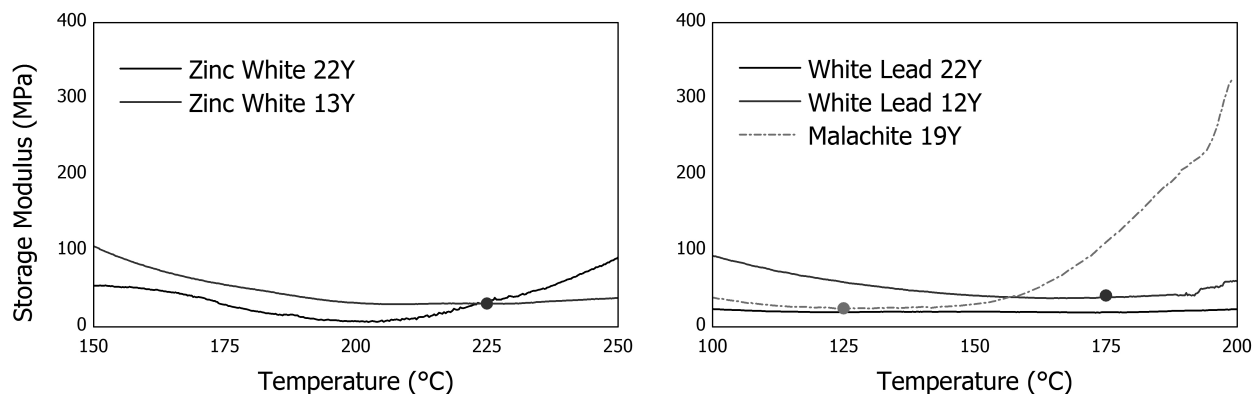


**Figure C.5.** Detail of the storage modulus plots of aged oil paint films pigmented with White Lead, Zinc White, and Malachite, that shows the data points that were used to estimate the crosslink densities of the films.

**Table C.1.** Results of the calculation used to estimate crosslink densities of the films.

Pigment	$T$ (°C)	$E'$ (MPa)	$10^3 \times \nu_e$ (mol/cm <sup>3</sup> )
Malachite	125	24.2	2.4
White Lead	175	41.1	3.7
Zinc White	225	30.5	2.5

considered as approximate due to the poor repeatability. Instead, this calculation was performed as a first approximation of a crosslink density, using the following equation:

$$\nu_e = E'/3RT$$

where  $\nu_e$  is the crosslink density,  $R$  is the gas constant, and  $T$  is the temperature in K [1]. The points that were chosen for this calculation are shown in Figure C.5. (For the films pigmented with Zinc White and White Lead, only one estimate per pigment was made since any differences would not have been statistically significant.) The results of this calculation are shown in Table C.1. Overall, the resulting crosslink densities are on the same order but slightly higher than those typical of highly crosslinked films [1].

#### C.4. References

- [1] L.W. Hill. Calculation of crosslink density in short chain networks. *Prog. Org. Coat.* **1997**, *31*, 235-243.

## APPENDIX D. MASS SPECTRA OF LEAD OIL PAINT FILMS

### D.1. Background

Three of the oil paint films considered here were analyzed using Time-of-Flight Secondary Ion Mass Spectrometry (ToF-SIMS) by a group at the University of Delaware [1]. For convenience, this appendix contains spectra that were collected as part of that study that are also relevant to the work in this dissertation. The external study should be consulted for experimental details and for peak assignments.

### D.2. Results and Discussion

As explained more thoroughly in the main text, linseed oil is composed primarily of various fatty acids, the vast majority of which is bound via glycerol molecules into triglycerides. When the oil is exposed to oxygen, unsaturated fatty acids become joined together, predominantly at sites that are stabilized by their proximity to double bonds. As time and oxidation progress, the film suffers hydrolysis. Saturated fatty acids (which in linseed oil are primarily palmitic,  $C_{16}$ , and stearic,  $C_{18}$ ) do not have double bonds, so they may simply cleave from the glycerol moieties during degradation. Unsaturated fatty acids cleave not only from the glycerol moieties but also from the crosslink sites. This gives rise to shorter diacids, including subaric ( $C_8$ ), azelaic ( $C_9$ ), and sebacic ( $C_{10}$ ), because most original fatty acids are  $C_{18}$  and have double bonds located approximately in the middle of the moiety.

Mass spectra of selected free (unbound) fatty acids in aged lead-containing films are shown in Figure D.1. Monoacids palmitic and stearic were more prevalent than the diacids, and the difference in abundances appeared more pronounced for the films pigmented with White Lead,  $2(PbCO_3) \cdot Pb(OH)_2$ , than the film pigmented with Naples Yellow,  $Pb_3(SbO_4)_2$ . Each of the free fatty acids was much more prevalent in the case of Naples Yellow than in White Lead. Interestingly, for the White Lead films, the age of the film (13 or 23 years) had only a slight bearing on the prevalence of monoacids, and was negligible for diacids. For the White Lead films, azelaic was the most common free diacid, followed by subaric acid, and then by sebacic.

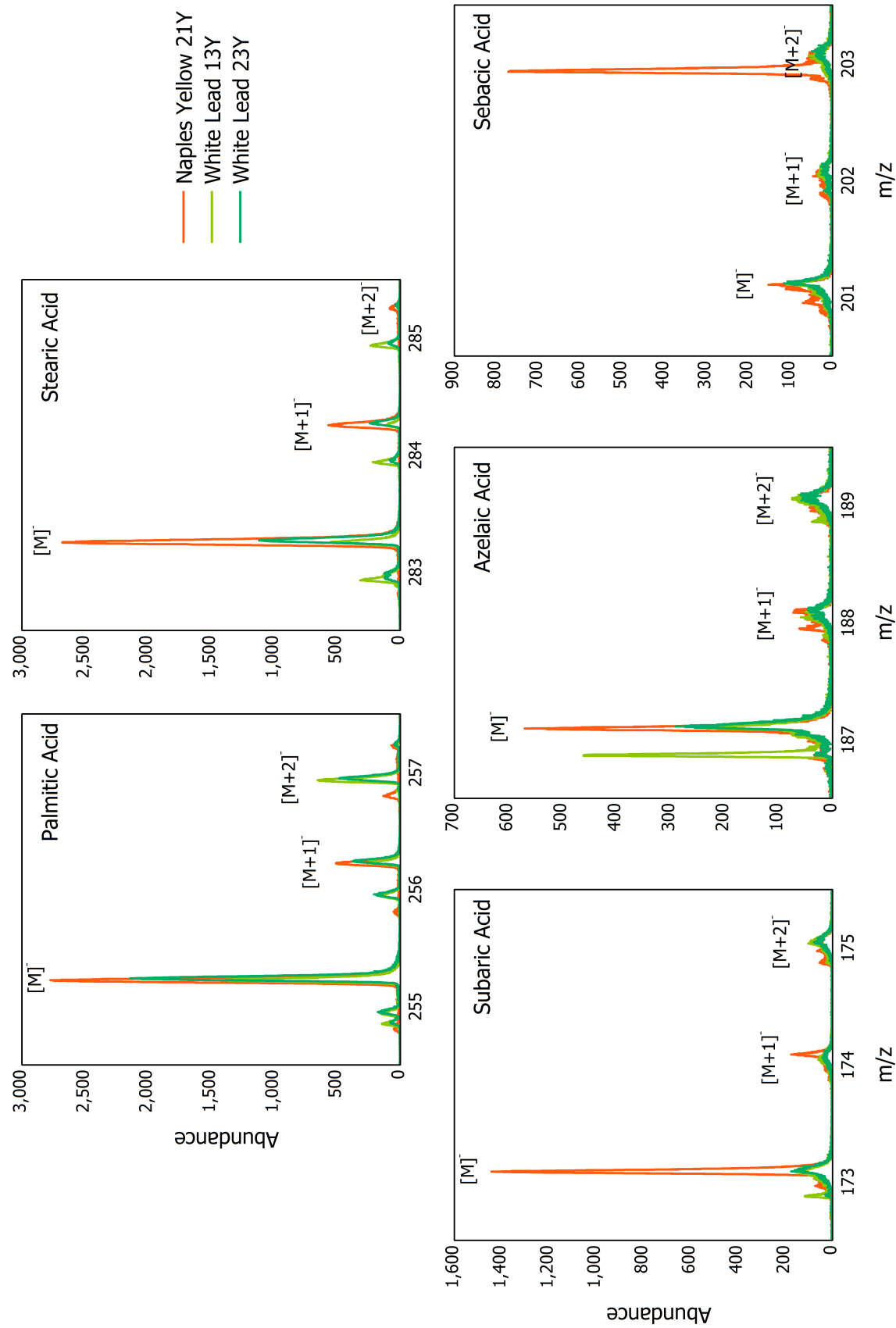


**Figure D.1.** Mass spectra of selected oil paint films showing  $m/z$  ranges that contain peaks assigned to free fatty acids. Adapted from [1].

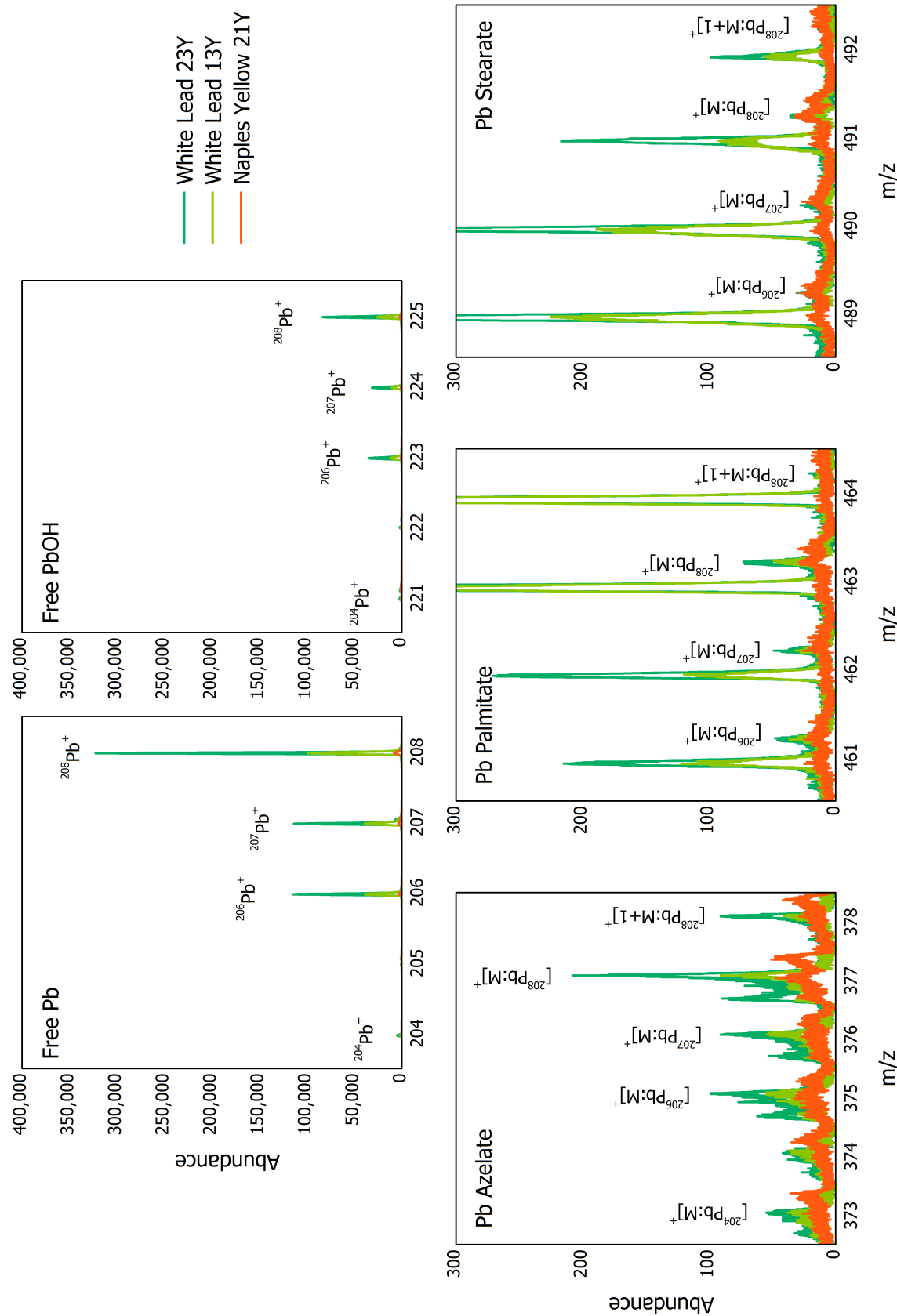


**Figure D.2.** Mass spectra of selected oil paint films showing  $m/z$  ranges that contain peaks assigned to free lead (top row) and lead-bound soaps (bottom row). Adapted from [1].



Mass spectra of free lead ions are shown in Figure D.2. For the White Lead paint, the abundance of free lead increased with age due to the diffusion of lead out of the pigment particles. The abundances of the free lead ions exceeded the abundances of free fatty acids by 1-2 orders of magnitude. In contrast, for Naples Yellow, the abundance of free lead ions was on the same order as for free fatty acids (Figure D.3). This was likely the reason that the occurrence of lead soaps was very low in the Naples Yellow film (Figure D.2), despite the high prevalence of the corresponding free fatty acids. The near-absence of soaps helps to explain the higher content of free fatty acids present in the Naples Yellow film, but only to a small extent. The balance may be due to a greater extent of hydrolysis in the Naples Yellow film as compared to White Lead.

For the White Lead films, the prevalence of soaps increased with age. Lead azelates were by far the most common of the three soaps considered, followed by lead palmitates and then, by lead stearates. (The content of lead stearates was nearly negligible. The assignment of peaks for lead soaps of subaric and sebacic acids was indeterminate and is not included here.) The greater abundance of lead palmitates versus stearates was consistent with the greater abundance of free palmitic acid versus stearic. However, the far greater abundance of lead azelates could not be similarly explained, since the content of free azelaic acid was far lower than the content of free monoacids. Further, it could not be explained by diffusion, since the content of free lead ions was orders of magnitude higher than the content of fatty acids, so the diffusion rate of metal would have been the controlling step in the soap formation reaction.

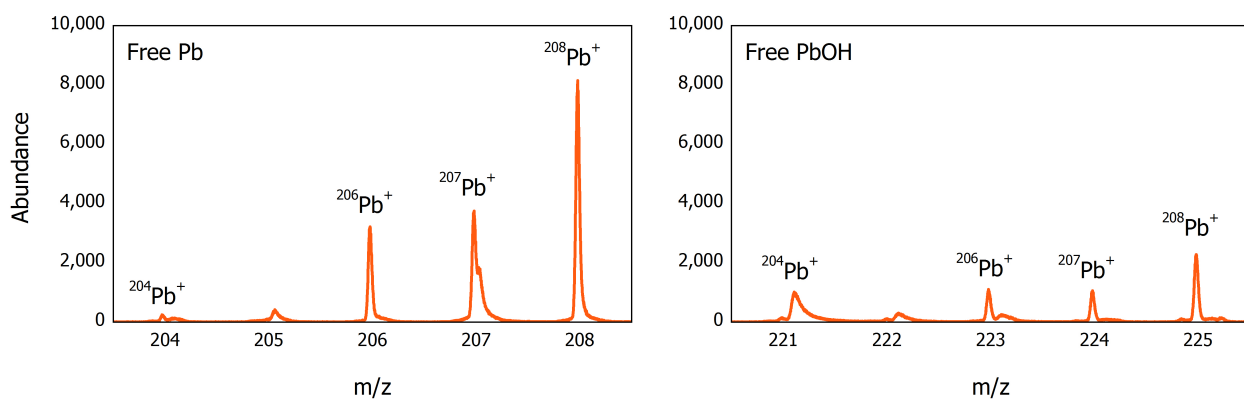


**Figure D.3.** Mass spectra of a 21-year-old oil paint pigmented with Naples Yellow, showing  $m/z$  ranges that contain peaks assigned to free lead. Adapted from [1]. This data is shown compared to White Lead in Figure D.2.

The most likely remaining reason is that azelaic acid is more reactive with lead ions than are the monoacids.

### **D.3. Conclusion**

ToF-SIMS was used to characterize the abundances of free fatty acids, free lead, and lead-bound fatty acids within lead-pigmented oil paint films. The abundances of free fatty acids showed that hydrolysis had occurred in films pigmented with both Naples Yellow and White Lead, and suggested that hydrolysis was more extensive in the Naples Yellow film. Lead soaps were clearly distinguishable in films pigmented with White Lead but were nearly absent for Naples Yellow, consistent with the greater stability of the Naples Yellow pigment against the diffusion of lead ions. The abundance of soaps in White Lead films increased with age. Lead azelates appeared to be the most common, followed by lead palmitates and then, lead stearates.

### **D.4. References**

[1] Z. Voras, K. deGhetaldi, B. Baade, J. Mass, T.P. Beebe, Jr. A closer look at historic paint materials using Time-of-Flight Secondary Ion Mass Spectrometry. Unpublished work, **2013**.

## APPENDIX E. INTRODUCTION TO MOLECULAR DYNAMICS

### E.1. Introduction

Chapter 2 has explained to a general audience those MD concepts that are necessary to understand the present work. This appendix extends that introduction to two topics referenced in Chapter 2 but not explained there in detail – the progress of a simulation through time, and the control of temperature and pressure. Important topics omitted from this introduction for narrative purposes are neighbor lists and parallel processing, which are computational techniques used to speed up the simulations. Readers interested in a more thorough introduction are referred to the literature [1-4].

### E.2. Time Evolution

In molecular dynamics, an initial configuration of particles proceeds through time in small increments termed time steps. During each time step, the classical ordinary differential equations of motion are solved and the atom coordinates are adjusted. *Time integration* is the numerical method that is used to accomplish this task: given the positions, velocities, and other properties at the current time  $t$ , the time integrator solves the equations of motion to obtain these properties at a later time  $t + \Delta t$ , where  $\Delta t$  is the size of the time step. This section describes the sequence of key events in LAMMPS [5, 6] when the velocity Verlet time integration algorithm is used [7]. This algorithm uses the *explicit central difference method* from the field of numerical analysis, such that the velocity at the midpoint of the time step (i.e., at time  $t + \frac{1}{2}\Delta t$ ) is used in the calculation of new coordinates.

At the start of the simulation, prior to the first time step, each particle is assigned an initial velocity. In the present simulations, initial velocities were always assigned at random (such that re-running a simulation would produce slightly different results), meaning that velocity vectors were assigned to random numbers from a uniform distribution. Although sampling from other distributions is also possible, this does not have a practical impact on results, since the Boltzmann distribution is established within only  $\sim 100$  time steps [1]. Once the random numbers were generated, their magnitudes were scaled to conform to the required temperature, and their directions were corrected such

that there would be no overall linear momentum. In the velocity Verlet algorithm, forces at time  $t$  are calculated prior to the first time step from the potential functions (e.g.,  $U_{ij}$  and  $U_{FENE}$ ), and accelerations  $a(t)$  are calculated from the forces.

At the start of the time step, thermostat and barostat functions described in the next section are called, which perform the first half of the velocity Verlet time integration algorithm. At this point, velocities  $v(t)$  are updated by a half-step, and positions  $x(t)$  are updated by a full step, as follows:

$$v(t + \frac{1}{2}\Delta t) = v(t) + \frac{1}{2}a(t)\Delta t \quad (\text{E.1})$$

$$x(t + \Delta t) = x(t) + v(t + \frac{1}{2}\Delta t)\Delta t \quad (\text{E.2})$$

Next, periodic boundary conditions are applied, such that particles whose new positions are outside of the simulation box are remapped back into the box. In addition, box boundaries may be adjusted, neighbor lists and bins may be rebuilt, and particles may be migrated between processors. However, the details of those operations are beyond the scope of this introduction.

When all particle positions are fully updated, interactions between the particles are computed using the new coordinates as input to the potential functions. This portion of the time step consumes the majority of the computational time. Afterward, the net force on each particle is known, and new accelerations  $a(t + \Delta t)$  are determined. Then, the second half of the velocity Verlet algorithm is performed:

$$v(t + \Delta t) = v(t + \frac{1}{2}\Delta t) + \frac{1}{2}a(t + \Delta t)\Delta t \quad (\text{E.3})$$

At this point, any requested properties are computed, and any specified output is written. In a typical run, thousands and sometimes millions of time steps must be performed because the size of the time step  $\Delta t$  must be very small. As the time step becomes larger, particle trajectories obtained by the simulation diverge faster and faster from their exact solution, which has the consequence of energy not being conserved. Therefore, shorter time steps must be used for fast-moving particles, such as at high temperatures or for rapidly-varying potentials. For this reason, a much shorter time step was used during the push-off run at the start of the present simulations, whose function was to remove overlaps between particles in the starting configurations.

## E.3. Control of Temperature and Pressure

### E.3.1. Introduction

#### E.3.1.1. Statistical Ensembles

Thermodynamics is a phenomenological theory that describes the behavior of macroscopic matter without reference to its microscopic constituents. The foundation for thermodynamics is provided by the field of statistical mechanics, which explains thermodynamic concepts in terms of the microscopic laws of motion. Statistical mechanics is founded on the idea that macroscopic observables such as temperature and pressure do not require knowledge of the system's microscopic configuration, which is termed its *microstate*. Instead, these properties may be computed by performing averages over an *ensemble*, which is a collection of all microstates that have an identical thermodynamic state.

An ensemble is described by enumerating those of its thermodynamic variables which are constant, which are termed *constraint variables*. The simplest ensemble is the microcanonical ensemble which is specified by a fixed number of particles  $N$ , a fixed volume  $V$ , and a fixed energy  $E$ . Since this ensemble cannot exchange energy or matter with its environment, it describes an isolated system. When a molecular dynamics simulation is performed using only the per-particle interactions (e.g.,  $U_{ij}$  and  $U_{FENE}$ ) to compute the net force on each atom, that simulation is performed in the microcanonical ensemble.

#### E.3.1.2. Temperature

The temperature of a given microstate is determined by the average kinetic energy of all microstates that constitute the respective ensemble. Therefore, when the net energy (kinetic + potential) of the ensemble is fixed, its temperature may change throughout the course of the simulation – so that temperature cannot be controlled for simulations conducted in a microcanonical ensemble. In order to effect isothermal conditions, one of the ensembles must be chosen for which  $T$  is a control variable rather than  $E$  – either canonical (NVT), isobaric-isothermal (NPT), or the grand canonical ensemble ( $\mu$ VT). The canonical ensemble is the simplest one of the set.

An instantaneous temperature may be calculated by

$$3k_B T = \frac{1}{N} \sum_{i=1}^N m_i v_i^2 \quad (\text{E.4})$$

where  $m_i$  is the mass of the  $i$ th particle,  $N$  is the number of degrees of freedom, and  $k_B$  is the Boltzmann constant.

The simplest method of controlling temperature is through velocity (re)scaling. In this method, at each timestep (or at a specified interval), the the velocities of all particles in the system are multiplied by the factor  $\lambda$ . If the initial temperature is  $T_0$ , the associated temperature change is as follows:

$$\begin{aligned} \Delta T &= \frac{1}{3k_B N} \sum_{i=1}^N m_i (\lambda v_i)^2 - \frac{1}{3k_B N} \sum_{i=1}^N m_i v_i^2 \\ &= (\lambda^2 - 1) \cdot T_0 \end{aligned} \quad (\text{E.5})$$

By choosing

$$\lambda = \sqrt{T_{sp}/T_0} \quad (\text{E.6})$$

where  $T_{sp}$  is the setpoint temperature, every time velocities are rescaled, the temperature of the system is compelled to match the setpoint.

However, the method of velocity scaling does not produce systems that are in any known ensemble, so that the dynamics of the system simulated with this approach do not resemble the dynamics of systems in the real world. That is because instantaneous properties such as temperature fluctuate with time (e.g., for ergodic systems, time average is equal to its ensemble average), whereas velocity rescaling suppresses any fluctuations. For this reason, velocity scaling is used only during the early stages of equilibration.

### **E.3.2. Canonical Ensemble (NVT)**

The canonical ensemble is specified by a fixed number of particles  $N$ , a fixed volume  $V$ , and a fixed temperature  $T$ . It describes a system that is in thermal contact with a heat bath, which is so large in proportion to the system of interest that any temperature changes in the heat bath may be neglected. Numerically, this is accomplished by introducing a *thermostat* into the system, which is any method that

adds or removes energy from the system in such a manner that the average system temperature matches the setpoint.

In the present simulations, the Langevin thermostat was used, in which the equations of motion due to particle interactions are coupled to Langevin's equations of motion for Brownian dynamics [8]. In this model, simulated particles are treated as though they are in contact with an *implicit background solvent* which maintains the temperature of the system. Such a solvent is represented not as particles, but as the effect that it would exert on those particles that are present in the system. The net force on each particle in such an implicit solvent becomes

$$F = F_c + F_f + F_r \quad (\text{E.4})$$

where  $F_c$  is the conservative force due to particle interactions (e.g., LJ and FENE),  $F_f$  is a frictional force, and  $F_r$  is a random force.

The frictional force represents a drag force that is proportional to the particle's mass and velocity,

$$F_f = -\Gamma m v \quad (\text{E.5})$$

where  $\Gamma$  is a damping constant which, as will be shown in the next equation, determines how quickly the temperature is relaxed. It may be conceptualized as proportional to the viscosity of the implicit solvent.

The random force represents implicit solvent that is bumping into the particle at a temperature  $T$ ,

$$F_r \propto \sqrt{\frac{k_B T \cdot m}{\Delta t \cdot \Gamma}} \quad (\text{E.6})$$

where  $k_B$  is the Boltzmann constant. The random aspect is implemented through the use of random numbers which randomize the magnitude and the direction of this force.

Overall, the Langevin thermostat controls temperature by agitating particles through the random force and by slowing them down through the friction force. The damping term stabilizes the dynamics which allows to use a time step that is large relative to the fastest mode of particle motion. This renders the Langevin thermostat well-suited for effecting large temperature changes. For this reason, the present set of simulations used the Langevin thermostat to model the first stage of the cooling procedure (Section 2.2.3.1).

### E.3.3. Isobaric-Isothermal Ensemble (NPT)

#### E.3.3.1. Pressure

In molecular dynamics, pressure is calculated using the virial equation,

$$PV = N \cdot k_B T + \frac{1}{3} \sum_i^N x_i \cdot F_i \quad (\text{E.7})$$

where  $F_i$  is the net force acting on the atom  $i$  and  $x_i$  is its position. This equation would reduce to the ideal gas law if the second term were zero, which would occur if the particles were non-interacting.

Pressure can be accurately described as a scalar per equation E.7 only for those systems that are isotropic. In all other cases, pressure is a tensor:

$$P = \begin{bmatrix} P_{xx} & P_{xy} & P_{xz} \\ P_{yx} & P_{yy} & P_{yz} \\ P_{zx} & P_{zy} & P_{zz} \end{bmatrix} \quad (\text{E.8})$$

Using this notation, each element  $P_{ij}$  is the pressure in the  $j$  direction which is acting on a hypothetical surface plane with a unit area that is oriented such that its normal points in the  $i$  direction. The pressure tensor is calculated in a manner similar to the pressure scalar:

$$P_{ij}V = \sum_k^N m_k v_{k_i} v_{k_j} + \sum_k^N x_{k_i} \cdot F_{k_j} \quad (\text{E.9})$$

Just as temperature is controlled by effecting changes in the particle velocities, pressure is controlled by effecting changes in the system volume. Among the three ensembles that are widely used in molecular dynamics, NVE, NVT, and NPT, the NPT ensemble is the most difficult one to generate because both the kinetic energy and the volume must be controlled. The two tasks are usually executed using different modules, a barostat for pressure and a thermostat for temperature. Since the same thermostats are used in NVT and in NPT simulations, an NPT simulation may be alternately viewed as running an NVT simulation while coupled to a barostat.

#### E.3.3.2. Andersen Barostat

The most commonly used barostats are based on the *extended system* approach in which the simulated system is coupled to its volume  $V$  as an additional degree of freedom. This coupling mimics the



action of a piston, and this coupled (extended) system of the simulation box and the piston together form the microcanonical ensemble – i.e., a system isolated from any other influences.

The simplest extended-system barostat, the Andersen barostat, is designed for systems that are isotropic (cubic) [9], so that while the volume of the system is adjusted to match the setpoint pressure, the shape of the simulation box remains unchanged. The equations of motion for the system are constructed from expressions for the potential and the kinetic energies of the piston and of the particles. The piston's potential energy is

$$E_{p,p} = P_{sp}V \quad (\text{E.10})$$

where  $P_{sp}$  is the setpoint external pressure and  $V$  is still the volume of the box. The piston's kinetic energy is

$$E_{p,k} = \frac{1}{2}M \left( \frac{dV}{dt} \right)^2 \quad (\text{E.11})$$

where  $M$  is a piston property which determines the time scale of the motion in a manner analogous to mass. The potential and kinetic energies of the particles in the simulation box are computed through the usual expressions for kinetic and potential energies, but using coordinates and velocities that are scaled in a manner that reduces the simulation box to a unit volume:

$$x_i' = \frac{x_i}{\sqrt[3]{V}} \quad (\text{E.12})$$

$$v_i' = \frac{v_i}{\sqrt[3]{V}} \quad (\text{E.13})$$

The expressions for the potential and the kinetic energies of the piston and of the particles are combined and used to derive the equations of motion of the scaled system. Then, the change of variables in equations E.12-E.13 is applied in the reverse direction, such that the equations of motion are transformed to the original set of variables. The final equations of motion are first-order ordinary differential equations which may be solved numerically using standard predictor-corrector algorithms.

The Andersen barostat described above has been generalized to anisotropic systems such that each dimension of the simulation box fluctuates independently of the others [10]. The method used in the present simulations [11, 12] is based on that approach.

### E.3.3.3. Nosé-Hoover Thermostat

When a barostat is used without coupling it to a thermostat, the ensemble that is generated is not isobaric-isothermal (NPT) but, rather, something else. The ensemble that is generated by the Andersen barostat is isobaric-isoenthalpic (NPH), which is rarely used in simulations. Most commonly, extended-system barostats are used together with extended-system thermostats such as the Nosé-Hoover thermostat [13-15] in order to generate an isobaric-isothermal ensemble. In this approach, the heat bath is modeled in a manner similar to the piston in the Anderson barostat. The heat bath is represented by a mass-like parameter  $Q$ , which is comparable to the mass-like parameter  $M$  for the piston, and a change of variables is performed in a manner analogous to equations E.12-E.13 in the derivation of the final equations of motion.

When the Nosé-Hoover thermostat is used alone, without a barostat, it generates a canonical ensemble (NVT). In the present simulations in which the system was equilibrated to a lower temperature at a constant volume, a Langevin thermostat was used rather than a Nosé-Hoover thermostat because when a step change is applied to the setpoint variable (e.g. temperature), extended-system methods produce large oscillations during equilibration. In contrast, the Langevin thermostat approaches the setpoint smoothly, without large fluctuations, such that much less time is needed for the system to reach equilibrium.

## E.4. Conclusion

This appendix has introduced two molecular dynamics topics in order to aid the reader in understanding the simulation procedure that is outlined in Chapter 2. First, the sequence of events during a time step has been illustrated in terms of the velocity Verlet algorithm which was used during the NVT components of the simulations. Second, the concept of statistical ensembles was introduced, followed by a description of the functions that are performed by the thermostating and barostatting modules. The functions were illustrated by describing the Langevin thermostat and the Andersen barostat. In addition, the Nosé-Hoover thermostat was summarized briefly. In these explanations, many specifics were omitted in order to limit the length of this introduction. Readers interested in further details are referred to *Computer Simulation of Liquids* for a general treatment of concepts and to *Understanding Molecular*

*Simulation: From Algorithms to Applications* as well as *Statistical Mechanics: Theory and Molecular Simulation* for a mathematical description of the molecular dynamics algorithms [1, 2].

## E.5. References

- [1] M.P. Allen, D.J. Tildesley. *Computer Simulation of Liquids*. Clarendon Press: Oxford, 1987.
- [2] D. Frenkel, B. Smit. *Understanding Molecular Simulation: From Algorithms to Applications*, 2<sup>nd</sup> Ed. Academic Press: New York, 2002.
- [3] M.E. Tuckerman. *Statistical Mechanics: Theory and Molecular Simulation*. Oxford University Press: New York, 2010.
- [4] C.R. Sweet. Chapters 1-2 in *Hamiltonian Thermostatting Techniques for Molecular Dynamics Simulation*, Ph.D. Thesis, University of Leicester, Leicester, 2004.
- [5] S.J. Plimpton. Fast parallel algorithms for short-range molecular dynamics. *J. Comp. Phys.* **1995**, *117*, 1-19.
- [6] *LAMMPS Developer Guide*. Sandia National Laboratories: 2011. <http://lammps.sandia.gov/doc/Developer.pdf>
- [7] W.C. Swope, H.C. Andersen, P.H. Berens, K.R. Wilson. A computer simulation method for the calculation of equilibrium constants for the formation of physical clusters of molecules: Application to small water clusters. *J. Chem. Phys.* **1982**, *76*, 637-649.
- [8] T. Schneider, E. Stoll. Molecular-dynamics study of a three-dimensional one-computer model for distortive phase transitions. *Phys. Rev. B* **1978**, *17*, 1302-1322.
- [9] H.C. Andersen. Molecular dynamics simulations at constant pressure and/or temperature. *J. Chem. Phys.* **1980**, *72*, 2384-2393.
- [10] M. Parrinello, A. Rahman. Polymorphic transitions in single crystals: A new molecular dynamics method. *J. Appl. Phys.* **1981**, *52*, 7182-7190.
- [11] W. Shinoda, M. Shiga, M. Mikami. Rapid estimation of elastic constants by molecular dynamics simulation under constant stress. *Phys. Rev. B* **2004**, *69*, 134103.
- [12] M.E. Tuckerman, J. Alejandre, R. López-Rendón, A.L. Jochim, G.J. Martyna. A Liouville-operator derived measure-preserving integrator for molecular dynamics simulations in the isothermal-isobaric ensemble. *J. Phys. A: Math. Gen.* **2006**, *39*, 5629-5651.
- [13] S. Nosé. A molecular dynamics method for simulations in the canonical ensemble. *Mol. Phys.* **1984**, *52*, 255-268.
- [14] S. Nosé. A unified formulation of the constant temperature molecular dynamics methods. *J. Chem. Phys.* **1984**, *81*, 511-519.
- [15] W.G. Hoover. Canonical dynamics: Equilibrium phase-space distributions. *Phys. Rev. A* **1985**, *31*, 1695-1697.

## APPENDIX F. MAPPING OF PHYSICAL UNITS TO COARSE-GRAINED UNITS

### F.1. Introduction

The work in Chapter 2 has explored some structural and thermo-mechanical properties of a series of simulated thermoset networks. These polymers were created by crosslinking coarse-grained monomers that were fictional, i.e., not linked to specific real-life systems. Nonetheless, these thermosets may be *mapped* to real-life systems in order to estimate the physical significance of the Lennard-Jones units that were used throughout the simulations. Mapping is very different from linking hierarchies (atomistic and coarse-grained) which is done in multiscale modeling because when hierarchies are linked, the link is established by adjusting parameters of the various interaction potentials, - whereas mapping is a simple calculation that is largely independent of simulation details. Since a single coarse-grained system may be mapped to many different real-life systems, the results of mapping have high uncertainties, and may be regarded as order-of-magnitude approximations. However, even order-of-magnitude approximations may provide useful checks. Such approximations are performed in this appendix.

### F.2. Mapping Calculations

The Lennard-Jones system uses the following fundamental units:  $\sigma$  for length,  $\varepsilon$  for energy, and  $m$  for mass. The unit of time is derived from the fundamental units as  $\tau = \sqrt{m\sigma^2/\varepsilon}$ . In order to map a Lennard-Jones system to a physical system, three parameters are necessary. Two of these, mass and length, are easily obtained from the molecular structure. The third parameter may be taken as the glass transition temperature  $T_g$ , as the elastic modulus  $E$  at a particular temperature, and from many other properties. Since mapping is a very inexact procedure, different mappings are likely to result from choosing to map using, for instance,  $T_g$ , as opposed to  $E$  or any other property. No meaningful gains are obtained by choosing one property over another, so the present mapping is performed by using  $T_g$  due to the wide availability of experimental values in the literature.

To perform the mapping, model 4-3 is conceptualized as an  $n=0$  diglycidyl ether bisphenol A (DGEBA) epoxy that is crosslinked with a ring-based diamine (Figure F.1). This set of physical systems is chosen based on the functionalities and the relative sizes of the simulated crosslinker and chain extender monomers. Continuing along this path, if the crosslinker in model 4-3 is a ring-based diamine, then the crosslinker in model 6-3 would be a ring-based triamine. Such a monomer is trivial to imagine, but none are used commercially because they would be too hindered sterically for all 6 amine hydrogens to be capable of reaction – unlike the diamines, all 4 of whose amine hydrogens are effective in forming crosslinks. Model 6-3, then, represents a limiting case, in which crosslinking is higher than is physically possible for a thermoset. This is consistent with its properties ( $T_g$ ,  $E$ ) being significantly higher than those of the other models.

The molecular weight of an  $n=0$  DGEBA epoxy (hereinafter referred to as simply “epoxy” throughout this appendix) is 340 gm/mol. Since each bead in the simulation has the mass of  $1m$ , if an epoxy is mapped to a two-bead chain extender molecule, this translates to

$$m = \frac{340 \text{ u}}{2} \times \frac{1.660538921 \times 10^{-27} \text{ kg}}{1 \text{ u}} = 2.822916166 \times 10^{-25} \text{ kg} \quad (\text{F.1})$$

$$\cong 3 \times 10^{-25} \text{ kg}$$

The length of an epoxy is approximately 16 Å. This number was obtained by drawing the structure of an epoxy, optimizing the geometry using the OPLS 2005 force field (Figure F.1), and then measuring the distance between the two farthest carbon atoms (which are located on the two oxirane

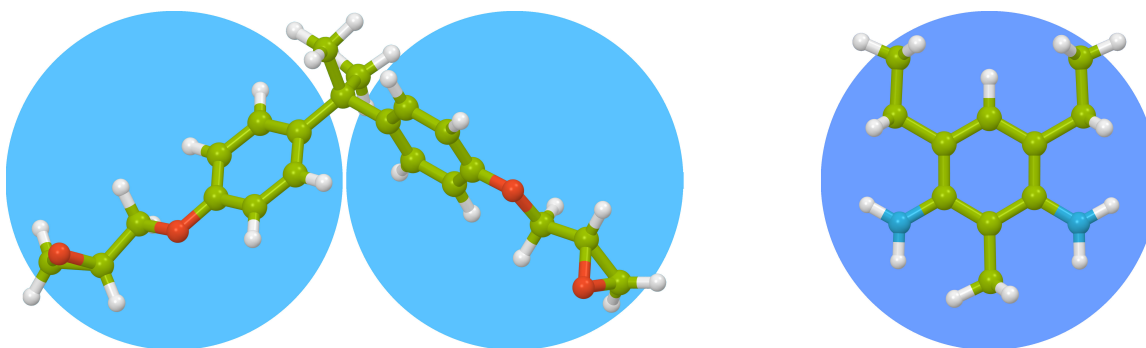


**Figure F.1.** A schematic that shows coarse-grained model 4-3 mapped to a  $n=0$  DGEBA chain extender and a DETDA crosslinker.

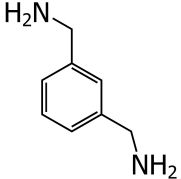
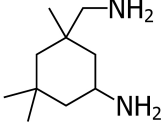
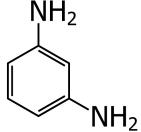
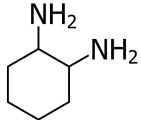
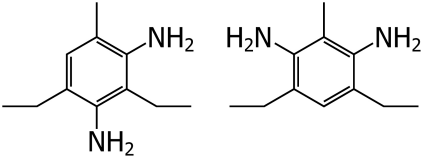
rings). The distance across two bonded coarse-grained beads is the sum of the optimum bond length,  $0.961 \sigma$ , and the optimum distance between the centers of the non-bonded beads,  $1 \sigma$ . This maps to slightly less than 1 nm:

$$\sigma = \frac{16 \times 10^{-10} \text{ m}}{1.961} = 8.159102498 \times 10^{-10} \text{ m} \quad (\text{F.2})$$

$$\cong 8 \text{ \AA}$$

For the unit of energy,  $T_g$  of model 4-3 was found to be  $0.465 \varepsilon/k_B$  (Section 2.3.1). Glass transition temperatures of several epoxy-diamine systems that have been reported in the literature are summarized in Table F.1. Since most studies do not consider whether complete conversion has been

**Table F.1.** Glass transition temperatures of some common thermosets, each prepared from a stoichiometric mixture of a DGEBA epoxy and the diamine listed. The epoxy used to prepare the DETDA-containing thermoset had  $n \approx 0.14$ . The epoxy used in all other systems listed was D.E.R. 332 which has  $n \approx 0.03$ . Glass transition temperatures were determined by DSC in all cases, except for the DETDA-containing thermoset, whose  $T_g$  was determined from the location of the DMA  $\tan \delta$  peak.

Diamine Structure	Name, Abbreviation, MW	Cure Schedule	$T_g$ (°C)	Ref
	<i>m</i> -xylenediamine mXDA 136 gm/mol	60°C/1 hr + 150°C/1 hr	127	[1]
	isophorone diamine IPDA 170 gm/mol	60°C/1 hr + 190°C/1 hr	171	[1]
	<i>m</i> -phenylenediamine mPDA 108 gm/mol	80°C/2 hr + 150°C/2 hr + 200°C/5 hr	179	[2]
	1,2-diamine cyclohexane 1,2-DCH 114 gm/mol	23°C/7.5 hr + 70°C/24 hr	199	[3]
	diethyltoluenediamine DETDA 178 gm/mol	100°C/2 hr + 120°C/2 hr + 175°C/4 hr + 200°C/2 hr	203	[4]

achieved, only reports of the highest obtained  $T_g$ s are cited. The values cover a broad range, 127-203°C, so the question arises which  $T_g$  value should be used for mapping. The value of 127°C is a poor representative of the series and may be excluded using the Q-test with 95% confidence. Then, the range of  $T_g$ s becomes much narrower, 171-203°C, and the mean value is used for mapping:

$$\frac{0.465\varepsilon}{k_B} = (188 + 273.15) \text{ K} = 461.15 \text{ K} \quad (\text{F.3})$$

$$\begin{aligned} \varepsilon &= \frac{461.15 \text{ K} \times k_B}{0.465} \times \frac{1.3806488 \times 10^{-23} \text{ J/K}}{k_B} = 1.369217622 \times 10^{-20} \text{ J} \\ &\cong 1 \times 10^{-20} \text{ J} \end{aligned} \quad (\text{F.4})$$

Finally, the unit of time is mapped to

$$\begin{aligned} \tau &= \sqrt{\frac{m\sigma^2}{\varepsilon}} = \sqrt{\frac{2.822916166 \times 10^{-25} \text{ kg} \times (8.159102498 \times 10^{-10} \text{ m})^2}{1.369217622 \times 10^{-20} \text{ J}}} \\ &= 3.704717863 \times 10^{-12} \sqrt{\frac{\text{kg} \cdot \text{m}^2}{\text{J}}} \\ &\cong 4 \text{ ps} \end{aligned} \quad (\text{F.5})$$

### F.3. Mapped Simulation Parameters

Simulations in Chapter 2 were performed at two temperatures,  $0.3 \varepsilon/k_B$  and  $1.0 \varepsilon/k_B$ . The lower temperature maps to 24°C (298 K) and thus represents room temperature. The upper temperature maps to 719°C (992 K). Such a temperature would be far too high for a real material, since real-world polymers decompose hundreds of degrees below this level. However, in simulated materials, bonded potentials may be used that do not allow bond-breaking, so that no decomposition takes place. Such was the choice used here. Then, raising the temperature has two consequences: faster dynamics which facilitate sample equilibration, and a lower sample density. The latter effect may be either desired (e.g. for modeling crosslinking of resin diluted in solvent) or undesired (e.g. for modeling reactions in bulk), depending on the goals of the experiment. For the reactions in Chapter 2, a lower sample density was desirable

because it would lead to more trapped free volume upon cooling which would produce more extreme visualizations of pore space.

The key time scales used in the simulations are summarized in Table F.2 together with the mapped real-world units. One reason coarse-grained simulations are sometimes chosen over atomistic simulations is that they are capable of reaching larger time scales when using the same computer resources, which is a consequence of having fewer degrees of freedom and the ability to use larger time steps. (Indeed, the mapped time step size of 18 fs is an order of magnitude larger than the time step size of 1 fs which is typical in atomistic simulations.) Therefore, it is useful to check how the present time scales compare to ones typical in the atomistic literature.

The duration of the crosslinking reaction is on the same order as in atomistic simulations and many orders of magnitude faster than real-world reactions which last hours or, sometimes, days. While a slower reaction could have been simulated, there was no reason to do that since the faster rate of reaction has not produced any known artifacts, either here or in the literature. Simulations that were used to determine  $T_g$  and  $\alpha_v$  were an order of magnitude slower than many atomistic simulations in recent literature and were on the same order as several others, although based on examination of the raw data, this slower rate likely had no effect on results. However, time scales used in tensile testing were 1.5 to 5 orders of magnitude slower than in atomistic simulations, and as detailed in Chapter 2, these large time scales had been motivated by necessity. Then, the use of coarse-graining was instrumental not only in producing generic architectures, but also for conducting simulations that would have been more computationally expensive for comparable all-atom models.

**Table F.2.** Simulation time scales mapped from Lennard-Jones units to real-world units.

LJ Units	Mapped Units	Description
0.005 $\tau$	18 fs	Time step used for all simulations after initial push-off
10 $\tau$	37 ps	Interval between successive attempts to create new bonds
10,000 $\tau$	37 ns	Crosslinking reaction for models 3-5 and 4-5
15,000 $\tau$	56 ns	Crosslinking reaction for models 4-3 and 6-3
2,000 $\tau$	7 ns	Equilibration stage in simulations used to characterize $T_g$ and $\alpha_v$
50,000 $\tau$	185 ns	Equilibration stage in simulations of tensile testing
1,002,000 $\tau$	3.7 $\mu$ s	Equilibration at NPT when cooling from $T=1.0 \epsilon/k_B$ to $T=0.3 \epsilon/k_B$



#### F.4. Mapped Simulation Results

Thermo-mechanical results obtained in Chapter 2 are mapped in Table F.3 to real-world units. Since mapping was performed using  $T_g$  as one of the coordinates,  $T_g$  results are with the range expected of thermoset polymers. Other properties, however, are somewhat at odds.

Real-world tensile moduli at room temperature vary widely by thermoset chemistry, spanning a range from  $\sim 800$  MPa for phenol-formaldehydes to  $\sim 9650$  MPa for melamine-formaldehydes [5]. The simulated materials are within this range, but on its far lower end. This is an expected consequence of disregarding bond angle, dihedral, and improper torsional interactions in the model. Then, the simulated materials were more flexible (less stiff) than most commercial thermosets, which have glassy moduli in the range of  $\sim 2$ -5 GPa, but not unreasonably so.

Real-world coefficients of volumetric thermal expansion range at room temperature from  $\sim 30 \cdot 10^{-6} \text{ K}^{-1}$  for polyimides to  $\sim 110 \cdot 10^{-6} \text{ K}^{-1}$  for unsaturated polyesters [5]. For this metric, the simulated materials are at the far upper end of the range, again as a consequence of being modeled as freely-jointed chains which have fewer barriers to expansion. In addition, the finite size effect facilitates thermal expansion, since expansion of a simulation cell involves cooperative motion over far smaller length scales than in real materials. Again, mapped values show that simulated materials are softer than most real materials, yet within a realistic range of properties.

However, when considering mapped bulk densities, simulated materials exhibit a striking discrepancy: they have densities of  $\sim 0.5 \text{ g/cm}^3$  whereas real thermosets have densities of  $1.0$ - $1.4 \text{ g/cm}^3$  [5]. This may be understood by revisiting the schematic diagram of the chain extender molecule in Figure F.1: the mapped segment of a DGEBA molecule has a larger aspect ratio than a coarse-grained bead. As

**Table F.3.** Characterization results mapped from Lennard-Jones units to real-world units.

Model	$T_g$ (°C)	Below $T_g$			Above $T_g$		
		$\rho$ (g/cm <sup>3</sup> )	$E$ (MPa)	$a_v$ (10 <sup>-6</sup> K <sup>-1</sup> )	$\rho$ (g/cm <sup>3</sup> )	$E$ (MPa)	$a_v$ (10 <sup>-6</sup> K <sup>-1</sup> )
3-5	171	0.553	776	114	0.470	4.4	289
4-5	175	0.555	857	112	0.476	7.9	275
4-3	188	0.560	916	106	0.483	12.7	261
6-3	225	0.560	888	99	0.493	25.8	233

a consequence, it would produce far denser packings than would be obtained if the coarse-grained model were replaced by an all-atom model as depicted in Figure F.1, since each such all-atom monomer would be surrounded by a thick sheath of free volume. Since the same is not true for the coarse-grained monomers – the beads are instead densely packed – little may be gained by considering the mapped material densities.

## F.5. References

- [1] M.J. Marks, R.V. Snelgrove. Effect of conversion on the structure-property relationships of amine-cured epoxy thermosets. *ACS Appl. Mater. Inter.* **2009**, *1*, 921-926.
- [2] M.-S. Lu, J.-L. Chen, Y.-S. Li, F.-C. Chang, M.-S. Li, C.-C.M. Ma. The kinetics, thermal and mechanical properties of epoxy-polycarbonate blends cured with aromatic amine. *J. Polym. Res.* **1998**, *5*, 115-124.
- [3] M. Villanueva, I. Fraga, J.A. Rodriguez-Añón, J. Proupín-Castiñeiras, J.L. Martín. Study of the influence of water absorption on different epoxy-diamine systems by DSC. *J. Therm. Anal. Calorim.* **2007**, *87*, 205-209.
- [4] W. Liu, R.J. Varley, G.P. Simon. Phosphorus-containing diamine for flame retardancy of high functionality epoxy resins. Part II. The thermal and mechanical properties of mixed amine systems. *Polymer* **2006**, *47*, 2091-2098.
- [5] G.T. Murray. Processing and properties of polymers. In *Introduction to Engineering Materials: Behavior, Properties, and Selection*. Marcel Dekker: New York, 1993, 371-424.

## APPENDIX G. NETWORK EVOLUTION DURING CROSSLINKING

### G.1. Introduction

A supplementary study was performed that extended the topological analysis described in Section 2.4 of the main text to the progress of network properties throughout the crosslinking reaction. One motivation was exploratory, to observe the course of the reaction and to compare it to the predictions of simple gel theories. The other goal was to determine whether bonding one chain extender molecule to each crosslinker molecule for models 4-3 and 6-3 prior to the start of the crosslinking reaction had an effect on the incidence of primary loops by the reaction's end.

### G.2. Simulation Procedure

For models with  $M_c=5$ , the same starting configurations were used as the ones in the main study in order to highlight differences in topologies that are due strictly to the stochastic factors. For models with  $M_c=3$ , new starting configurations were generated such that crosslinker molecules were not pre-bonded to the chain extender molecules. These modified models are identified as 4-3' and 6-3' throughout this appendix.

Simulations and analyses were conducted following the procedure described in the main text, but with two modifications. First, the duration of the simulations for models 4-3' and 6-3' was extended such that the final extent of reaction matched that for models 4-3 and 6-3 (Table G.1). Second, configurations were stored after every such timestep when the simulation had attempted to create new bonds (i.e., every  $10 \tau$ ), and the topology of each configuration was then analyzed to determine the prevalences of

**Table G.1.** Extents of the crosslinking reactions (%) described in the primary study in Chapter 2 compared to the extents of reactions (%) of the supplementary study which is the subject of this appendix.

Primary Study			Supplementary Study		
Model	Mean	SD	Model	Mean	SD
3-5	97.8	0.1	3-5	97.9	0.1
4-5	97.7	0.2	4-5	97.8	0.2
4-3	98.6	0.1	4-3'	98.6	0.1
6-3	97.9	0.1	6-3'	98.0	0.1

bonds, primary loops, and dangling chains at each such timestep. In the course of this procedure, the sizes of all fragments that comprised each configuration were determined, and the sizes of the largest and the second-largest fragment were further tracked for each sample. The extent of reaction was calculated for each configuration as the number of bonds made by the average crosslinker molecule to chain extender molecules, divided by the functionality of that crosslinker  $f$ . Model-wide properties were calculated as the average across its respective five samples.

### G.3. Results and Discussion

The progress of instantaneous properties throughout the course of the reactions is shown as a function of time in Figure G.1 and as a function of conversion in Figure G.2. Effective functionality increases only slowly for each model at first as new bonds result primarily in dangling chains. However, after ~50% of the bonds have been made, new bonds serve to connect these chains to the growing network, so the prevalence of dangling chains decreases. This halfway point occurs early in the reaction in terms of time.

As a shorthand, the largest fragment is referred to here as the *backbone*, even for times preceding gelation. The plots of backbone size vs. conversion have a qualitative shape that depends on the prevalence of looping, such that for models that are more prone to looping, the plots of backbone size vs. conversion are less steep than for those models that are not. This is because the fraction of new bonds that are intramolecular rather than intermolecular is far larger for models that are prone to looping (4-3' and 6-3') than those that are not.

The size of the second-largest fragment increases appreciably at first, but it drops to negligible when all large fragments become incorporated into the backbone, which occurs slightly prior to the inflection point in each model's plot of its backbone size. This suggests the approximate location of the gel points. The gel point is defined as the time when the crosslinked network percolates throughout the system, such that, in descriptions of macroscopic phenomena, its size is said to become infinite. However, such a process cannot be identified in a periodic system because it occurs over distances far larger than the size of the simulation box, so the size of the second-largest fragment must be relied upon

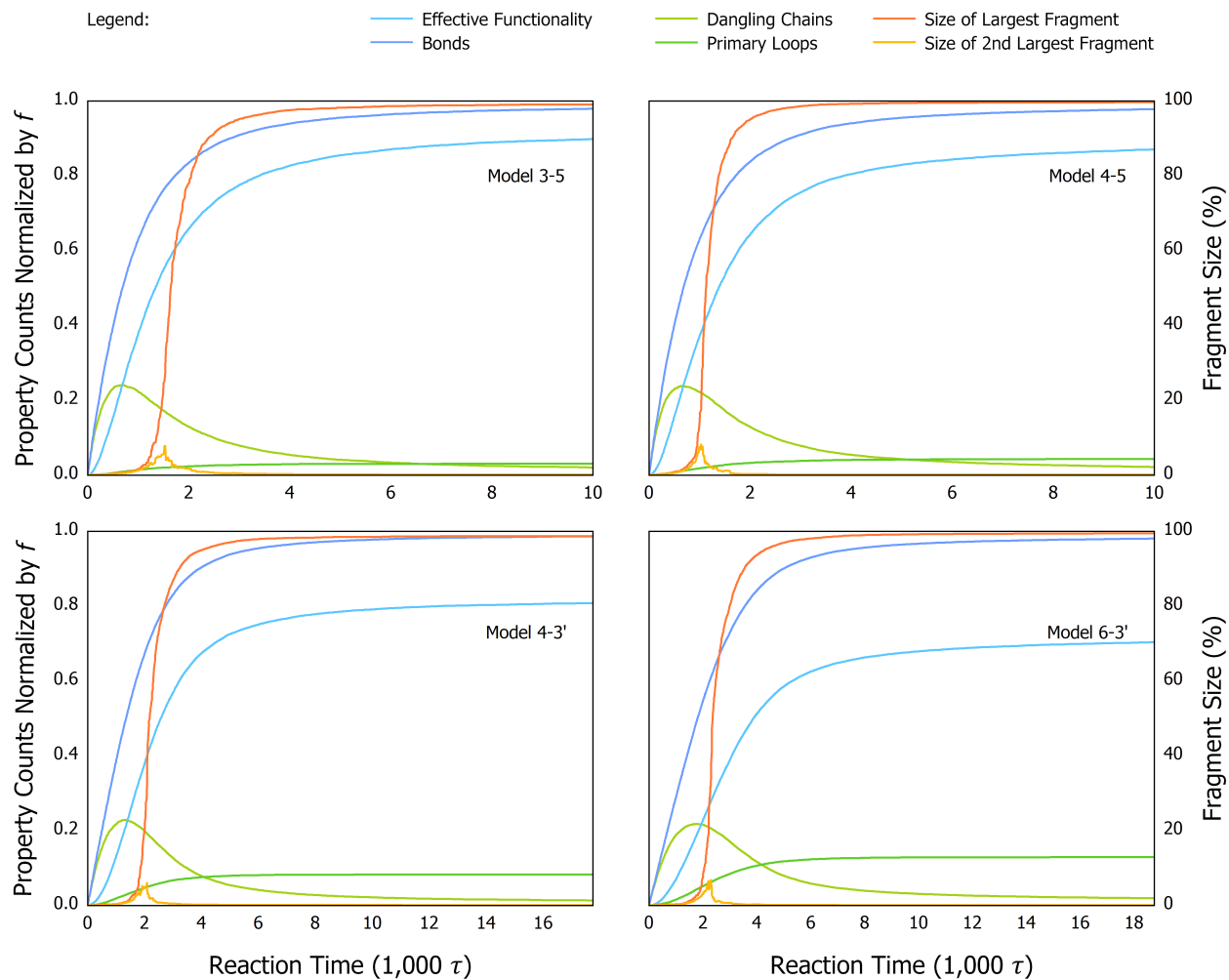


**Figure G.1.** Network properties for each model throughout the course of crosslinking reactions shown as a function of time. The left y-axis indicates the characteristics of the average network junction within each system: the numbers of bonds to chain extender molecules, the numbers of primary loops and dangling chains, and the resulting effective functionality of the average network junction, all normalized by the crosslinker functionality  $f$ . The right y-axis indicates the sizes of the largest and the second-largest fragment within each system, shown as a percentage of beads that comprise that system.

in its stead. Unfortunately, the shape of the peak in the size of the second-largest fragment broadens as a consequence of the finite size effect. Therefore, the location of the gel point may be only estimated, and the most reasonable estimate (using the discussed metrics) is the time point shortly after the maximum in the size of the second-largest fragment.

Several theories exist which predict the location of the gel point. Those that are most widely used are the oldest and the simplest ones: the Carothers theory and the Flory-Stockmayer theory. Both

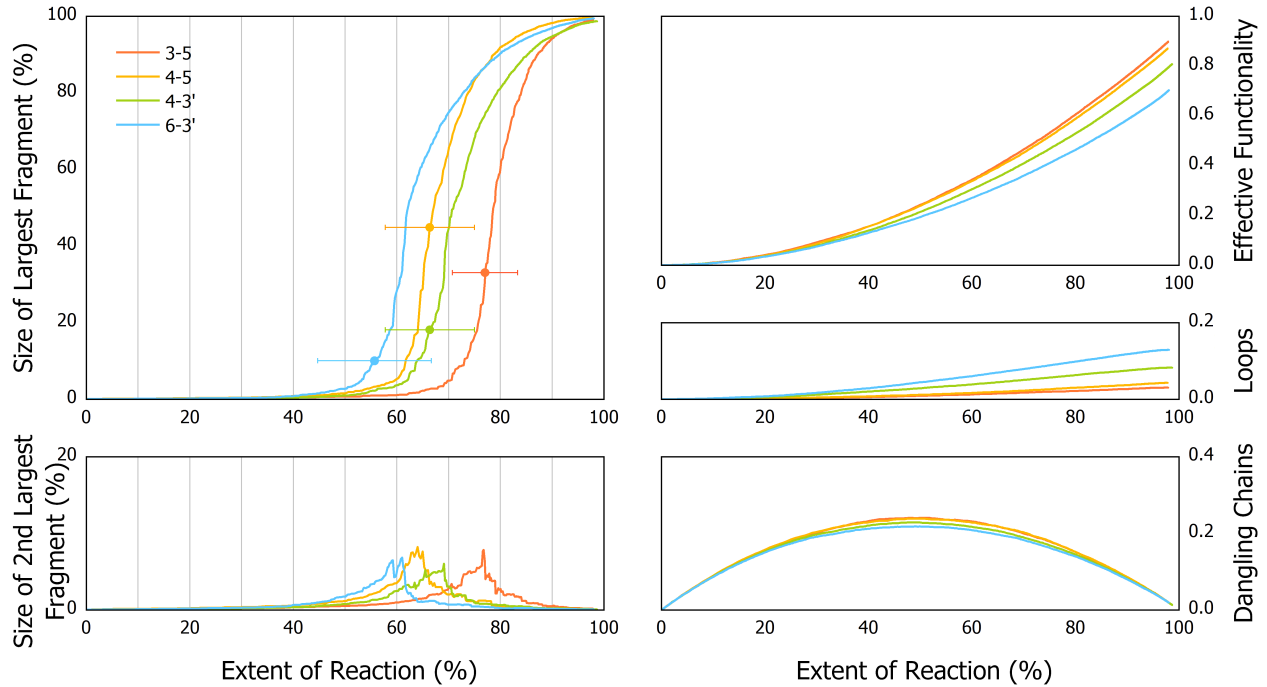


**Figure G.2.** Network properties for each model throughout the course of crosslinking reactions shown as a function of conversion. Markers in the subplot of the size of the largest fragment (i.e., the backbone size) indicate the extents of reaction at the gel point as follows: the minimum and the maximum error bars indicate forecasts of the Flory-Stockmayer and the Carothers theories, respectively, while the marker itself indicates the value obtained by averaging the two forecasts.

provide expressions for the extent of reaction at gelation,  $p_{gel}$ , using as inputs only the functionalities of the starting monomers and their stoichiometric ratios.

In the Carothers theory [1], the conversion at gel point is calculated simply as

$$p_{gel} = \frac{2}{f_{avg}} \quad (\text{G.1})$$

where  $f_{avg}$  is the average functionality of all the monomers in the system. In the Flory-Stockmayer theory [2-7], conversion at gel point is calculated using the branching coefficient

$$\alpha = \frac{1}{f - 1} \quad (\text{G.2})$$

where, in a two-component system such as ones used here,  $f$  is the functionality of the higher-functional monomer. For stoichiometric systems, conversion at gel point is calculated as follows:

$$p_{gel} = \sqrt{\alpha} \quad (\text{G.3})$$

**Table G.2.** Extents of reaction at gelation,  $p_{gel}$ , predicted for the present models using the Flory-Stockmayer theory and the Carothers theory, as well as the value obtained by averaging the two predictions.

Model	Flory-Stockmayer			Carothers		Average
	$f$	$a$	$p_{gel}$	$f_{avg}$	$p_{gel}$	$p_{gel}$
3-5	3	0.50	70.7%	2.40	83.3%	77.0%
4-5	4	0.33	57.7%	2.67	75.0%	66.4%
4-3	4	0.33	57.7%	2.67	75.0%	66.4%
6-3	6	0.20	44.7%	3.00	66.7%	55.7%

The predictions of the Flory-Stockmayer theory and the Carothers theory for the current models are listed in Table G.2. The values are identical for models 4-5 and 4-3 because these theories do not take into account the molecular weight between crosslinks  $M_c$ . In practice, the Flory-Stockmayer theory typically underestimates the conversion at the gel point while the Carothers theory typically overestimates it. (The underestimate from the Flory-Stockmayer treatment is due to its assumption that no cyclization reactions take place, such that the Flory-Stockmayer prediction is sometimes used against experimental results to approximate the extent of intramolecular reaction.) If an empirical assumption is made that the inaccuracies introduced by the two methods are equally significant, then a third prediction of  $p_{gel}$  may be obtained by averaging the predictions of the two theories. It has been shown that such an empirical approach provides values that are very close to experimental results [8]. Therefore, Table G.1 includes the average value of  $p_{gel}$  alongside the predictions of the Carothers and the Flory-Stockmayer theories.

The gel points predicted by the three methods are shown in Figure G.2 against the simulation data. The average method appeared to provide good predictions for models with  $M_c=5$ , such that the forecast nearly coincided with the peak in the size of the second-largest fragment. For models with  $M_c=3$ , the prediction of the average method slightly preceded the peak in the size of the second-largest fragment. This discrepancy may be due to the greater incidence of looping in the models with  $M_c=3$ , which would produce a larger error in the Flory-Stockmayer prediction of the gel point. However, whether or not this discrepancy is truly in error is indeterminate. The more interesting finding is that the simple gel theories are in qualitative agreement with the data.

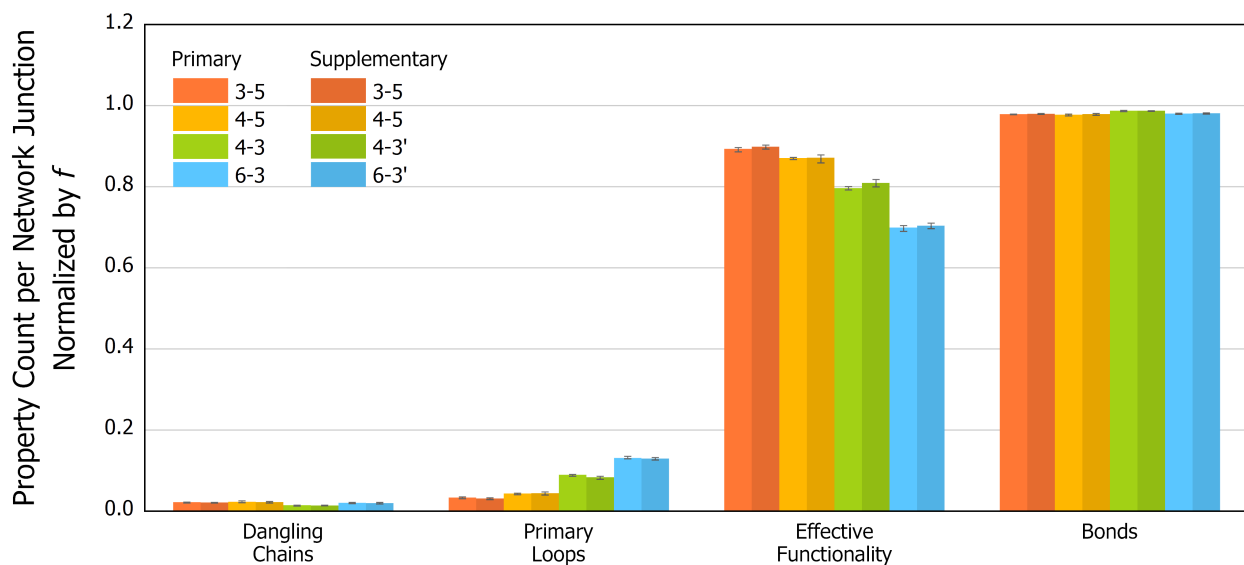


**Figure G.3.** Prevalence of network defects in the series of thermosets in the primary study in Chapter 2 compared to the same in the supplementary study which is the subject of this appendix. Error bars in each model-wide property show the smallest and the largest value of the respective sample property.

Finally, in Figure G.3, network properties at the end of this supplementary set of crosslinking reactions are compared to the ones obtained in the primary study. The two sets of simulation data are in agreement. This is important because one question for this supplementary study was whether pre-bonding the chain extender molecules in models 4-3 and 6-3 had contributed to loop formation. However, the differences between the properties of models 4-3/4-3' and 6-3/6-3' are not significant.

#### G.4. Conclusion

Simulations of crosslinking reactions were performed in which the progress of network properties was followed throughout the reactions. Properties tracked were the numbers of bonds between crosslinker and chain extender molecules, the numbers of primary loops and dangling chains, and the composite property of effective functionality which reflected the combined effect of the former three network parameters. In addition, the sizes of the largest and the second-largest fragment were followed. The approximate location of the gel point was estimated as the point where the ratio of the largest to the second-largest fragment sizes began to diverge.

The progress of properties was consistent with expectations based on what is commonly known about reaction kinetics. The approximate locations of gel points were in agreement with the prediction



produced by averaging the forecasts of the Flory-Stockmayer and the Carothers theories of gelation. However, this agreement could be only qualitative because the exact locations of the experimental gel points was indeterminate. Finally, network properties of models simulated in this supplementary study were compared to those of the models in Chapter 2. Differences in properties were only minor, so the effect of pre-bonding chain extenders to models 4-3 and 6-3 was not significant.

## G.5. References

- [1] W.H. Carothers. Polymers and polyfunctionality. *Trans. Faraday Soc.* **1936**, *32*, 39-49.
- [2] P.J. Flory. Molecular size distribution in three dimensional polymers. I. Gelation. *J. Am. Chem. Soc.* **1941**, *63*, 3083-3090.
- [3] P.J. Flory. Molecular size distribution in three dimensional polymers. II. Trifunctional branching units. *J. Am. Chem. Soc.* **1941**, *63*, 3091-3096.
- [4] P.J. Flory. Molecular size distribution in three dimensional polymers. III. Tetrafunctional branching units. *J. Am. Chem. Soc.* **1941**, *63*, 3096-3100.
- [5] W.H. Stockmayer. Theory of molecular size distribution and gel formation in branched-chain polymers. *J. Chem. Phys.* **1943**, *11*, 45-55.
- [6] W.H. Stockmayer, H. Jacobson. Gel formation in vinyl-divinyl copolymers. *J. Chem. Phys.* **1943**, *11*, 393.
- [7] W.H. Stockmayer. Theory of molecular size distribution and gel formation in branched polymers. II. General cross linking. *J. Chem. Phys.* **1944**, *12*, 125-131.
- [8] A. Pizzi. On the correlation of some theoretical and experimental parameters in polycondensation cross-linked networks. *J. Appl. Polym. Sci.* **1997**, *63*, 603-617.